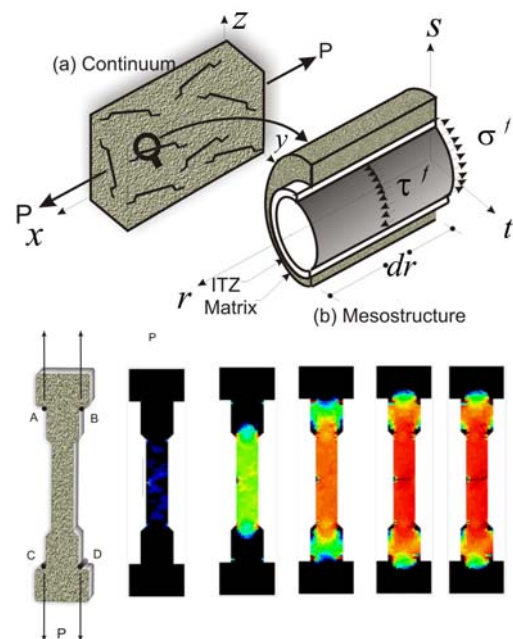# Multifield-Based Modeling of Material Failure in High Performance Reinforced Cementitious Composites

D. F. Mora
X. Oliver
A. E. Huespe

Multifield-Based Modeling of Material Failure in High Performance Reinforced Cementitious Composites

D. F. Mora
X. Oliver
A. E. Huespe

Abstract

Cementitious materials such as mortar or concrete are brittle and have an inherent weakness in resisting tensile stresses. The addition of discontinuous fibers to such matrices leads to a dramatic improvement in their toughness and remedies their deficiencies. It is generally agreed that the fibers contribute primarily to the post-cracking response of the composite by bridging the cracks and providing resistance to crack opening (Suwaka & Fukuyama 2006).

On the other hand, the multifield theory is a mathematical tool able to describe materials which contain a complex substructure (Mariano & Stazi 2005). This substructure is endowed with its own properties and it interacts with the macrostructure and influences drastically its behavior. Under this mathematical framework, materials such as cement composites can be seen as a continuum with a microstructure. Therefore, the whole continuum damage mechanics theory, incorporating a new microstructure, is still applicable.

A formulation, initially based on the theory of continua with microstructure Capriz (Capriz 1989), has been developed to model the mechanical behavior of the high performance fiber cement composites with arbitrarily oriented fibers. This formulation approaches a continuum with microstructure, in which the microstructure takes into account the fiber-matrix interface bond/slip processes, which have been recognized for several authors (Li 2003, Naaman 2007b) as the principal mechanism increasing the ductility of the quasi-brittle cement response. In fact, the interfaces between the fiber and the matrix become a limiting factor in improving mechanical properties such as the tensile strength. Particularly, in short fiber composites is desired to have a strong interface to transfer effectively load from the matrix to the fiber. However, a strong interface will make difficult to relieve fiber stress concentration in front of the approaching crack. According to Naaman (Naaman 2003), in order to develop a better mechanical bond between the fiber and the matrix, the fiber should be modified along its length by roughening its surface or by inducing mechanical deformations. Thus, the premise of the model is to take into account this process considering a micro

field that represents the slipping fiber-cement displacement. The conjugate generalized stress to the gradient of this micro-field verifies a balance equation and has a physical meaning.

This contribution includes the computational modeling aspects of the high fiber reinforced cement composites (HFRCC) model. To simulate the composite material, a finite element discretization is used to solve the set of equations given by the multifield approach for this particular case. A two field discretization: the standard macroscopic and the microscopic displacements, is proposed through a mixed finite element methodology. Furthermore, a splitting procedure for uncoupling both fields is proposed, which provides a more convenient numerical treatment of the discrete equation system.

The initiation of failure in HPFRCC at the constitutive level identified as the onset of strain localization depends on the mechanical properties of the all compounds and not only on the matrix ones. As localization criteria is considered the bifurcation analysis in combination with the localized strain injection technique presented by Oliver et al. (Oliver et al. 2010a). It consists of injecting a specific localization mode during the localization stage, via mixed finite element formulations, to the path of elements that are going to capture the cracks, and, in this way, the spurious mesh orientation dependence is removed.

Model validation was performed using a selected set of experiments that proves the viability of this approach. The numerical examples of the proposed formulation illustrated two relevant aspects, namely: 1) the role of the bonding mechanism in the strain hardening behavior after cracking in the HPFRCC and 2) the role that plays the finite element formulation in capturing the displacement localization in the localization stage.

Acknowledgments

Contents

List of figures

List of Boxes

Nomenclature

A_f	Cross area of the fiber;
$\mathbf{b}$	Body forces;
$\mathbf{B}^e$	Strain interpolation matrix;
$\mathfrak{B}_0$	Initial configuration of the body at $t = 0$;
$\mathfrak{B}$	Continuum body;
$\partial\mathfrak{B}$	Boundary surface of $\mathfrak{B}$;
$\mathbb{C}^{tg}$	Composite tangent operator;
$\mathbb{C}_m$	Matrix elastic constitutive tensor;
$\mathbb{C}_m^{tg}$	Constitutive tangent tensor for the matrix
$\mathbb{C}_f^{tg}$	Elasto-plastic tangent modulus
d_m	Damage variable associated with the matrix;
d_f	Diameter of the fiber;
$\mathbb{E}_f$	Fiber elasticity tensor;
E_m	Matrix Young's modulus;
E_f	Fiber Young's modulus;
g_f	Specific energy;
G_f	Fracture energy;
$\mathbb{G}_\Gamma$	Fiber matrix interface elasticity tensor;
$\mathbb{G}_\Gamma^{tg}$	Constitutive tangent tensor for the matrix fiber interface;
$\mathbf{F}$	Deformation gradient tensor;
f_m	Damage function;
f_f	Fiber yield surface;
f_Γ	Fiber matrix yield surface;
$\mathbf{F}^{ext}$	Global vector of external forces;
$\mathbf{F}^{int}$	Global vector of internal forces;
G_Γ	Elastic shear modulus;
$\mathcal{H}_f$	Heaviside's function;
H_f	Hardening/softening modulus associated with the fiber;
H_Γ	Hardening/softening modulus associated with the fiber matrix interface;
H_m	Softening modulus associated with the matrix;
$\bar{H}$	Discrete softening parameter;
$\mathbb{I}$	Four order Identity tensor
$\mathfrak{K}_{tg}$	Global tangent matrix;
k_m	Matrix volume fraction;
k_f	Fiber volume fraction;
k_c	Compound volume fraction;
l_a	Characteristic length;

$\mathbb{M}$	Fourth order tensor for the anisotropic damage model;
n_f	Number of fiber bundles;
$\mathbf{n}$	Unit vector orthogonal to the discontinuity surface;
$\mathbf{N}_j$	Displacement interpolation functions;
$[\mathbf{N}]^e$	Nodal shape function matrix;
$[\mathbf{N}]^e_v$	r derivatives of the shape functions matrix;
$[\mathbf{N}]^e_o$	s derivatives of the shape functions matrix;
$\mathbf{P}$	External force vector;
P^{int}	Total internal power;
P^{ext}	Total external power;
$\mathbf{p}^I_i$	Nodal slip displacements;
q_m	Matrix stress-like internal variable;
q_f	Fiber stress-like internal variable;
$\mathbf{q}_i$	Composite nodal displacements
$\mathbb{Q}_{loc}$	Localization tensor;
r_m	Matrix strain-like internal variable;
$\mathbf{r}^{ifib}$	Unit direction vector of the fiber bundle I ;
$\mathfrak{R}$	Global residual vector;
$\mathbf{S}$	Microstress tensor;
S	Discontinuity surface;
$\mathbf{T}$	Transformation matrix;
$\mathbf{t}^*$	Imposed surface traction vector;
t	Pseudo time;
t_B	Bifurcation time;
$\bar{\mathbf{u}}$	Matrix displacement field;
$\mathbf{u}$	Total displacement field;
V_c	Volume of a compound;
V	Total volume of the material;
W	Total energy dissipated;
$\mathbf{x}$	Spatial (or current) coordinates vector;
$\mathbf{X}$	Material (or referential) coordinates vector;
$\mathbf{z}$	Micromorphic force vector;
$\mathbf{1}$	Second order Identity tensor
$\boldsymbol{\alpha}_m$	Internal variables set associated with the matrix;
α_{m0}	Initial value of the strain like variable;
$\boldsymbol{\alpha}_f$	Internal variables set associated with the fiber;
$\boldsymbol{\alpha}_\Gamma$	Internal variables set associated with fiber matrix interface;
δ_Γ	Dirac delta function placed in Γ ;
$\delta\mathbf{u}$	Virtual variation of the $\mathbf{u}$ displacement field;
$\delta\beta^{(I)}$	Virtual variation of the $\beta^{(I)}$ displacement field;
β	Total relative fiber matrix displacement;
β^α	order parameters in the complex body;
β^p	Plastic component of the matrix fiber relative displacement;

β^e	Elastic component of the slip;
$\boldsymbol{\beta}$	Fiber-matrix relative displacement field;
$\boldsymbol{\zeta}$	Microforce vector;
$\boldsymbol{\varepsilon}_m$	Matrix strain tensor;
$\boldsymbol{\varepsilon}_f$	Fiber strain tensor;
ε_f^e,	Elastic strain component of the fiber strain;
ε_f^p	Plastic strain component of the fiber strain;
η_ε	Strain norm;
$\boldsymbol{\gamma}$	shear strain concentrated in the IZ surface;
Γ	Interfacial transition zone IZ surface;
ψ	Helmholtz free energy function;
ψ_m	Matrix free energy;
ψ_0	Matrix elastic free energy;
ψ_f	Fiber free energy;
ψ_f^h	Fiber free energy associated with the hardening/softening mechanism;
ψ_Γ	Fiber-matrix interface free energy;
Ψ	Perimeter of a fiber with any cross section shape;
L_e	Embedded length of the fiber;
$\boldsymbol{\sigma}$	Cauchy stress tensor;
$\boldsymbol{\sigma}_m$	Matrix stress tensor;
σ_m^{ut}	Ultimate tensile strength of the matrix;
σ_m^{uc}	Ultimate tensile strength of the matrix;
σ_f	Uniaxial component of the fiber stress tensor;
σ_f^y	Yield stress of the fiber
σ_{rr}	Component of the fiber stress tensor in the $r-$ direction;
σ_{rs}	Component of the fiber stress tensor in the $s-$ direction;
$\hat{\boldsymbol{\sigma}}$	Stress evaluated through the constitutive model for the composite;
$\bar{\boldsymbol{\sigma}}$	Effective stress tensor;
$\tilde{\sigma}_f^{(I)}$	Fiber axial stress evaluated through the fiber constitutive model;
λ_{n+1}	Prescribed load fractor;
λ_m	Damage consistency parameter;
λ_f	Fiber plastic multiplier;
λ_Γ	Plastic multiplier associated with the fiber matrix interface;
$\boldsymbol{\nu}$	Outward unit normal to the boundary;
τ_{rs}	Bond frictional stress in the fiber matrix interface zone;
τ_Γ^u	IZ ultimate bond strength;
$\tilde{\tau}_f^{(I)}$	Shear stress evaluated through the interface zone constitutive model (IZ);
$\bar{\lambda}$, $\bar{\mu}$	Lame's parameters
Π_f	Fiber perimeter;
Ω_{ini}	Injection domain;
$\Omega \backslash \Omega_{ini}$	Not injected domain;

Chapter 1
Introduction and state of the art

1.1.   High performance fiber reinforced cement composites

Cementitious materials such as mortar or concrete are brittle and have an inherent weakness in resisting tensile stresses. However, the addition of discontinuous fibers to such matrices leads to a dramatic improvement in their toughness and remedies their deficiencies. It is generally agreed that the fibers contribute primarily to the post-cracking response of the composite by bridging the cracks and providing resistance to crack opening (Suwaka & Fukuyama 2006).

In conventional fiber reinforced concrete (conventional FRC), the fiber content is usually low and the tensile response is characterized by the widening of a single crack, similar to an unreinforced concrete (Li & Li 2000), while high performance fiber reinforced cement composites (hereafter, HPFRC Composite) are highly ductile and characterized by pseudo strain hardening in tension. Consequently, strain hardening and multiple cracking constitute the main differences between FRC and HPFRC composite.

In order to make a proper description of the HPFRC composites, we first introduce a commonly used definition of a composite material, as follows: "A composite material is a combination of two or more materials having compositional variations and depicting properties distinctively different from those of the individual materials of the composite. The composite material is generally better than any of the individual components as regard their strength, heat resistance or stiffness" (Rajput 2008).

From the mathematical point of view, this imposes significant restrictions on defining adequate models and simulation tools making the analysis quite complicated. Therefore, since the difficulty of building a composite model is enormous, composite models are mostly patchwork and trial-and-error approaches. In fact, there are fundamental difficulties common

to all composite models, which still remain unresolved. This motivates us to study the internal mechanisms in HPFRC composites, with the view towards developing an appropriate model.

Our concern in this chapter is to introduce the description of the mechanisms involved in the HPFRC composites behavior and to present the current state of knowledge of simulation of this kind of composite. Pursuing these ideas, firstly, a brief overview of the principal elements of HPFRC composite mechanical behavior and an introduction to the key concepts are presented. Then, it is summarized a state-of-the art of current research on analytical and numerical methods in the context of both the composite analysis and the fracture problem and finally, it is outlined the general and specific objectives to be accomplished in this work.

1.1.1.   General classification of fiber reinforced concrete composites

Over the recent years, there have been significant advances in the design and use of short fiber reinforced cement and concrete composites as an industrial material, especially those combining several different types of fibers. These materials are particularly developed for specific applications, for which toughness, ductility and energy absorption are fundamental properties.
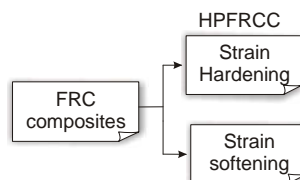
Figure 1.1 General classification of FRC composite. Adapted from (Naaman 2007a)

A general classification has been suggested.in (Naaman & Reinhardt 2006) and is based on whether the response of the composite is strain-hardening or strain-softening, as is illustrated schematically in Figure 1.1. Thus, high performance fiber reinforced cement composites (HPFRC Composite) are a class of composites characterized by a strain-hardening behavior in tension after first cracking, accompanied by multiple cracking up to relatively high strain levels.

However, the above presented classification is simple and does not reflect any peculiarities. According to (Naaman & Reinhardt 2006), a more specific classification is possible using the volume fraction of fibers, V_f, as the property characterizing strain-hardening and deflection-hardening response in fiber composites. Figure 1.2 contains the information on the critical volume fraction of fibers, $\left(V_f\right)_{cri}$, needed to achieve strain-hardening or deflection-hardening behavior. Thus, under tensile stress, the condition $V_f \geq \left(V_f\right)_{cri-tension}$ will produce strain-hardening and under bending load, the condition $\left(V_f\right)_{cri-bending} \leq V_f \leq \left(V_f\right)_{cri-tension}$ will cause deflection-hardening, otherwise the composite response will show strain-softening or deflection-softening, respectively.
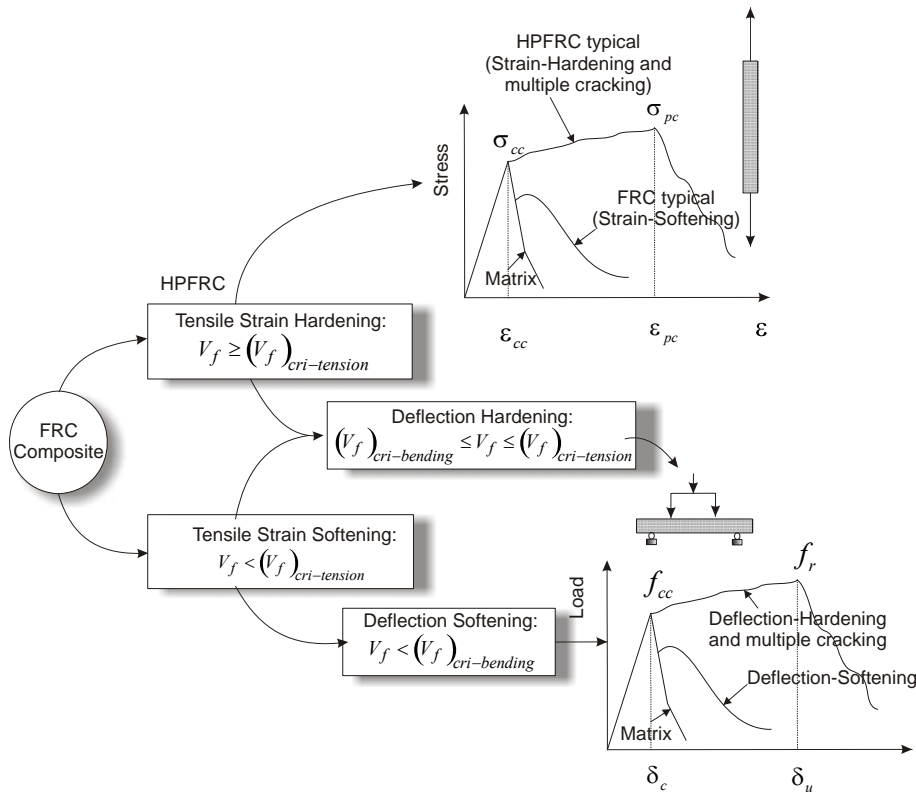
Figure 1.2. Classification of FRC composites based on tensile strain-stress response. Adapted from (Naaman & Reinhardt 2006)

1.1.2.   Typical stress-strain curves under tension. Conventional FRC vs. HPFRC composites

The stress-strain response characterizes the material behavior of plain concrete, conventional FRC and HPFRC composites. In brittle materials under tension (plain concrete or cement matrices), occurs little or no plastic deformation and the material fractures near the end of linear-elastic portion of the curve. Nevertheless, unlike the plain concrete, the characterization of the response of concrete-based composites not only involves the macroscale behavior but also the mesoscale one. Consequently, in conventional FRC and HPFRC composite, the presence of the fibers might contribute to promote inelastic deformation, improved ductility, and increased toughness. In this regard, it has been recognized as being the basic fracture mechanisms that influences the postcracking response, the following: (i) the debonding of the fibers, (ii) the pull-out of the fibers from the matrix, and (iii) the associated increase in crack opening.
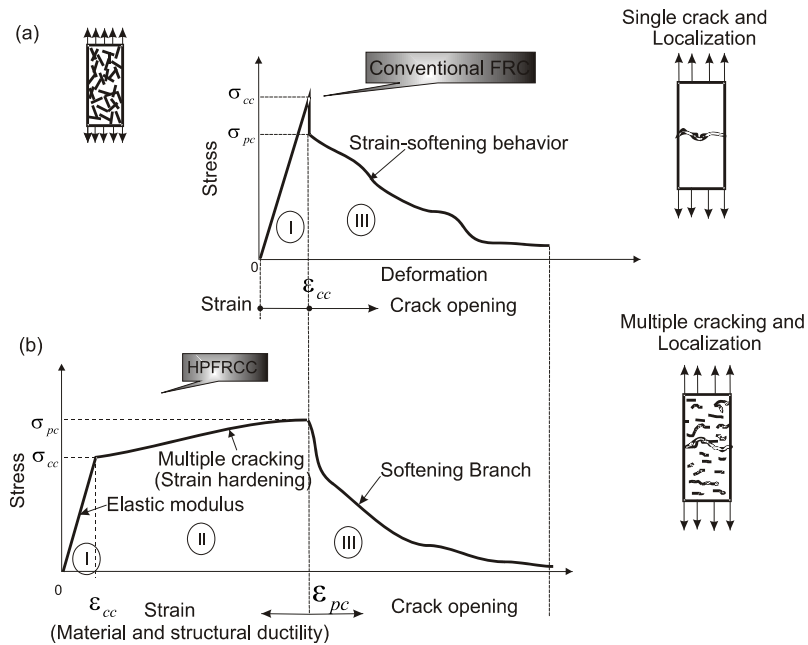
Figure 1.3 Typical stress-strain curve in tension until complete separation (a) Conventional strain-softening FRC composite (b) Strain-hardening composite. Adapted from (Naaman & Reinhardt 2006)

A brief discussion of the characteristics of the concrete-based composite response is introduced at this point, which gives some insights of the general behavior of these materials. Let us consider figure 1.3(a) that represents the typical response for conventional fiber reinforced concrete; the stress strain curve shows an ascending branch up to the peak stress, this point is characterized by its stress-strain coordinate $\left(\sigma_{cc}, \varepsilon_{cc}\right)$, which is followed almost immediately by the post-cracking behavior. After localization, the curve presents a descending branch, and therefore, no multiple cracking occurs.

In contrast, the stress-strain curve of an HPFRC composite, as in figure 1.3(b), starts with an initial ascending portion up to first structural crack $\left(\sigma_{cc}, \varepsilon_{cc}\right)$; at this point, the stress-strain curve deviates from the linear portion. This point is followed by a strain-hardening branch ending in the point $\left(\sigma_{pc}, \varepsilon_{pc}\right)$, which is denominated maximum post cracking stress-strain point. At the peak point, one crack becomes critical and starts the localization process, no other cracks can develop, and only this critical crack will open under deformation. Localization is characterized in the stress-strain curve by a descending branch and during this process fibers pull-out or fail (Li 2003). In summary, the general conclusion is that the introduction of short fibers in a cement-based matrix changes significantly the strain-stress curve, increasing the failure strain and the fracture toughness of the composite (Lin & Li 1997), (Li 2003).

According to (Suwannakarn 2009), it is possible to separate the curve in different stages and characterize each branch. Three stages can be considered in the HPFRC composite behavior, as follows (see Figure 1.3(b)),

- Elastic stage and first crack point before reaching the point: $\left(\sigma_{cc},\varepsilon_{cc}\right)$
- Multiple cracking stage from $\left(\sigma_{cc},\varepsilon_{cc}\right)$ till $\left(\sigma_{pc},\varepsilon_{pc}\right)$.
- Localization and softening stage.

In the first stage, the matrix remains intact and essentially elastic, so that the curve shows linear behavior up to σ_{cc}. When the first crack occurs, conventional FRC response softens, while HPFRC composite hardens (Stage II). This strain-hardening effect in the response of HPFRC composites is due, at least in part, to the ability of fibers to transfer the stresses during pull-out. As the load increases, new micro-cracks initiate, and possible coalescence between them might occur. The higher is the load, the longer are the cracks (Fantilli et al. 2007), (Fantilli et al. 2009). Consequently, the stiffness reduces, but its value remains positive, and therefore, the post cracking strength σ_{pc} is higher than σ_{cc} (Suwannakarn 2009). After saturation of matrix cracking, the stress applied on the composite is sustained only by unbroken fibers, and as far as this stress increases, the fraction of broken fiber could increase depending on the friction between the fibers and the matrix.

After reaching a maximum value in the post-cracking tensile strength point $\left(\sigma_{pc},\varepsilon_{pc}\right)$, the localization process starts (Stage III) and softening of the response is exhibited by the curve. Only one of the multiple cracks, previously developed in stage II, remains opening while the others cracks close (Naaman 2007b). The main underlying mechanism during this stage is the fiber pull out behavior of the composite (Suwannakarn 2009). It is evident that the behavior of the material into the last two stages depends on several parameters and phenomena including fracture toughness of the composite, fiber pull-out mechanism and fiber parameters, as well as bridging effect (Fischer 2006).

1.1.3.   Main fiber characteristics

The fibers used in cement composites are mainly organic, mineral or man-made and they can be classified, in general, into two categories: metallic and non-metallic. Today, for large scale civil and architectural structures, steel fibers are mainly used. Due to the increased interest in this field, many scientists devote much effort to study and develop new approaches for optimizing the fiber performance by changing its physical and mechanical features. A brief description of HPFRC composites with metallic and non metallic fibers is presented in (Colin 2000) and (Naaman A. E 1995). In the case of steel fibers, the geometry can play an important role; therefore, nowadays the industry has a wide variety of geometries available. Figure 1.4 is a sketch of possible geometries for short fibers. The benefits of fibers in cement based composite are evident, nevertheless, fiber inclusion to concrete reduces the workability during fabrication.

Steel fiber profile	Longitudinal Profile
Smooth surface (round flat or any shape)	
Crimped (round, flat or any section)	
Round with hooked ends	
Round with end buttons	
Indented, etched, roughened surface	
Poligonal Twisted	

Figure 1.4. Steel fiber profiles.

The major problem of short fiber composites is that the interfaces between the fiber and the matrix become a limiting factor in improving mechanical properties such as strength. Particularly, in short fiber composites, it is desired to have a strong interface to transfer effectively load from the matrix to the fiber. However, a strong interface will make difficult to relieve fiber stress concentration in front of the approaching crack. In this regard, currently, the research on steel short fiber composites concerns the optimal combination of geometric properties to obtain a superior performance. According to Naaman (Naaman 2003), to develop a better mechanical bond between the fiber and the matrix, the fiber can be modified along its length by roughening its surface or by inducing mechanical deformations. Namman (Naaman 2003) also discusses about the development and design of a new generation of steel fibers for use in cement, ceramic and polymeric matrices.

1.2. Some aspects about fiber reinforcement mechanics

As previously discussed, the evidence from both analytical and experimental studies strongly supports that the primary mechanisms of the HPFRC composites response involves mechanisms at mesoscopic or microscopic levels. Although, several models have been proposed to describe the behavior of the HPFRC composites in tension, an adequate model should capture naturally, at least partially, those features of the material response, which most critically influence the structural performance. In the remainder of this section, we will confine our attention on the principal aspects and issues associated with the fiber-matrix interface action and the manner in which it affects the cement based composites behavior.

1.2.1.   Fiber pullout and bond slip

The interaction forces between fiber and the matrix are transmitted by the interfacial bond, between the fiber and the surrounding matrix (Naaman & Najm 1991). Moreover, bond is considered a key phenomenon governing the mechanical properties of the composite (Guerrero & Naaman 2000). This mechanism is very complex in cement composites because of the presence of combined actions and the variability in the bond properties. Among these properties are: (1) physical and chemical adhesion between fiber and matrix, (2) geometrical characteristics of the mechanical adhesion surfaces, in the case of deformed, crimped, and hooked fiber, (3) fiber-to-fiber interlock and (4) friction by confinement (Naaman & Najm 1991). Additionally, another important component is the inclination of the fiber respect to the loading action ((Naaman A. E 1976) and (Laranjeira et al. 2010)).

Fiber pullout consists of pulling on one of both ends of a fiber embedded in a matrix. Fiber pull out tests are often conducted to understand the nature of the underlying mechanisms of the reinforcement processes and to assess bond-slip characteristics, where the fiber slip is monitored as a function of the applied load. From the experimental results, a typical bond shear stress-slip curve can be adequately adjusted by pullout testing to different situations. Nevertheless, it is emphasized that the bond characteristics depend on several factors involving the orientation of the applied load, the embedded length of the fiber, the shape of the fiber, and the strength of the matrix (Lee et al. 2010). Figure 1.5(a) illustrates the configuration of the fiber-matrix interface consisting of a quarter of fiber surrounding by the matrix material (bulk matrix). The Interfacial transition zone (ITZ) in concrete and cement composites is the region of the material surrounding the fibers (see Figure 1.5(a)). Figure 1.5(b) shows the general relationship between local bond shear stress and slip during the pullout process of a fiber into the composite, which is characterized by the shear modulus G_f and the maximum bond shear strength τ_{max}.
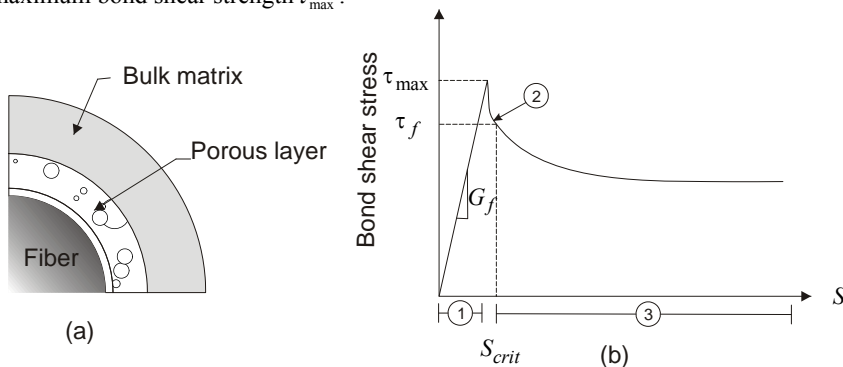
Figure 1.5 (a) Configuration of the fiber-matrix interface (b) General relationship between local bond shear stress and slip during the pullout process. Adapted from (Barros et al. 2005)

1.2.1.1. Matrix-fiber bound characteristics

The interfacial region between the bulk matrix and the fiber plays an important role to transfer the stresses from the matrix to the fiber. It is widely acknowledged that this zone has different morphology if compared with the remaining material. The properties of ITZ depend mainly on the nature of the binder, the presence of additives, and the water/cement ratio. During the loading process, three types of debonding mechanisms are involved, i.e. chemical, mechanical and frictional. In the pullout process of straight fiber, after the initial elastic region has been passed (1) (see Figure 1.5(b)), the chemical debonding mechanism is activated (region (2)). During this stage, there exists fully compatible fiber-matrix deformation. When chemical bonding is exhausted, frictional stresses are generated along the embedded length (portion of the fiber in the concrete matrix) due to the abrasion in the interfacial zone (region (3)), (Cunha et al. 2007).

The frictional bond can be improved by deformation processes in the steel fibers (Li & Stang 1997), which leads to better local interaction between the fiber and the matrix; in this case, the strain distribution in the compounds is smoother. This technique has proven to be the most effective one in improving the matrix-fiber interface (Banthia & Trottier 1994).

1.2.1.2. Aligned fibers

Three different phases can be distinguished in the pullout response of smooth steel fibers (Guerrero & Naaman 2000), namely, elastic stage, debonding and frictional pull out, as illustrated in Figure 1.6. The first phase is a linear ascending branch (OA), which is associated with elastic and/or adhesive bond. The pre-peak branch (AB) corresponds to the cracking of the interface transition zone, this crack growth causes the crack to be maximal at the critical debonding length until peak load, and the portion (BC) represents the propagation of the crack in the interfacial debonding zone until the end of the fiber length, namely, fully debonding. The point C indicates the initiation of the pull out under frictional slip. The load decreases since both the available frictional area and the roughness decrease (Cunha et al. 2007).

The pre-peak pullout response of hooked end fibers can be characterized by three different branches. In the (OA) and (AB') ascending branches, the adhesive bond and debonding up to full debonding appears which occurs at point B'. Path (B'C') is an additional increase of load due to the mechanical anchorage provided by the hooked end. The branches (C'D') and (D'E') correspond to the deformation of the hooked end. Finally, the load decreases in the branch (E'F'), following the same frictional mechanism as in the straight fibers. It can be concluded that *the fundamental mechanism that increases the pullout response in hooked end fibers is the plastic deformation that occurs in the hook portion* (Naaman & Najm 1991).
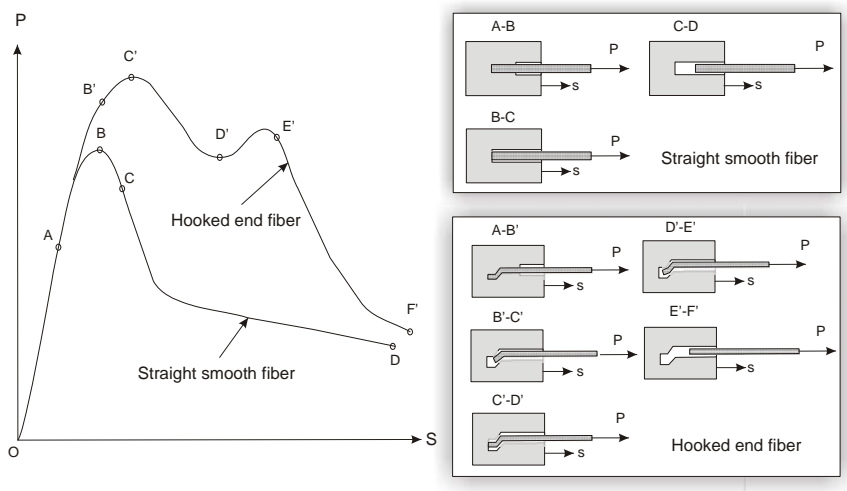
Figure 1.6 Pull out relationship between the load and the end-slip. Adapted from
(Cunha et al. 2007)

1.2.1.3. Inclined fibers

When the fibers are inclined with respect to the loading direction, a very complex stress field in the vicinity of the fiber can be induced (Banthia & Trottier 1994). A noticeable increasing is observed in both the pullout and the bond shear stress-slip relationship with respect to non-inclined fibers. Additionally, the pullout response of the inclined straight and deformed fibers display other effects, such as fiber bending, matrix spalling and local frictional effects (Laranjeira et al. 2010).

Crack opening will induce not only pullout, but bending on the fiber. For this reason, Leung and Geng (Leung & Geng 1998) proposed to decompose the bridging force P in two components: S represents the debonding/pull-out component due to interfacial stress along the fiber, and R, the bending component due to reactions from the matrix. The last component causes concentration of stress in the region between the fiber and the crack, resulting in concrete spalling (Cunha et al. 2007) and increase of the pullout load. Additionally, the pullout resistance of inclined fiber depends on both, bending and yielding, mechanisms, which are developed under small pullout loads, since the fiber will almost immediately be bent when the pullout starts to apply.

1.2.2.   Bridging effect

In order to understand the bridging effect, a fiber-reinforced specimen can be considered subjected to tensile loads, as it is shown in Figure 1.7. In absence of fibers, the cementitious material behaves as a quasi brittle material, but when the fibers are immersed into the matrix, the tensile stresses are transmitted from the matrix to the fibers (Nammur 1989). The applied

load will be shared by both components: the matrix and the fibers, and the participation of each compound is dictated by their relative stiffness and by the interfacial transition zone (ITZ) properties. As aforementioned, the tensile specimen will reach a stress stage at which the first micro-cracks develop. However, these are so small to be visible by the naked eye.

When a micro-crack is observed under close inspection at higher magnification (see for instance Figure 1.7), the fibers are seen passing through it and bridging the crack surfaces. The fibers transfer the forces across the crack and new micro-processes are activated (Kabele 2007a). These transfer processes are dominated by the bond strength in the interfacial zone. Experimental observations indicate that the properties of the fiber affect strongly the bridging effect; regarding this, the geometrical and mechanical properties can be modified in order to increase the bond strength and subsequently the bridging effectiveness (Naaman 2003).
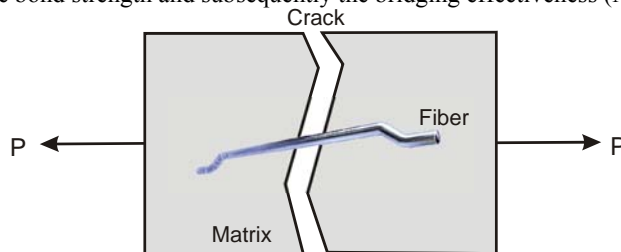
Figure 1.7 Pull out and bridging effect under tensile load.

1.3.   Material nonlinearities in reinforced cement composite

In HPFRC composites, various large-scale non-linearities associated with the matrix damage and fiber failure arise. This coexistence of degradation processes in the compounds, prior to composite failure, takes place during strain-hardening stage, in which the matrix failure is controlled by pre-existing flaws. Then, multiple cracks develop, until strain localization occurs at one of these cracks (Zhang et al. 2002). According to (Wu & Li 1994), the evolution of multiple cracking appears to be a stochastic process associated with distributed initial flaw sizes. The main sources of nonlinearities are, therefore, due to the nonlinear behavior of the compounds. The following sections provide basic information about the damage process in the matrix and the plasticity in the steel fiber.

1.3.1.   Matrix damage

Concrete is a quasi-brittle material, i.e., in controlled uniaxial tensile test, it is observed a softening branch after reaching a maximum load (Hariri 2001). Due to this characteristic, a damage model is usually employed to describe its mechanical behavior. The damage theory was presented by Kachanov in 1958 and further elaborated upon by Kachanov, Lemaître and Chaboche (1985). They described damage as a degradation in elasticity properties with con-

sequent decrease of the areas that transmit internal forces, through the appearance and subsequent growth of microcracks and microcavities (Maugin 1992). In the context of continuum mechanics, the growth of microcracks and microcavities is taken into account by introducing an internal variable that characterizes the degradation level of the material and transforms the real stress tensor into an effective stress tensor.

An additional process due to the brittle nature of cementitious matrices, is provoked when a fiber crosses a microcrack and the most superficial pieces of matrix wedges tend to spall off (Laranjeira et al. 2010). This is called *matrix spalling*. The larger is the crack opening displacement, the higher is the bending of the debonded segments of the fibers. The matrix spalling can influence the fiber behavior in the composite, since it deviates from the original direction the applied force at the fiber exit point.

Another failure mode exists in HPFRC composites and occurs when concrete strain reaches ultimate strain before rupture strain in the reinforcement under compression, this is referred as compressive crushing. This failure mode typically occurs if the element is over reinforced (Volume fraction of fibers higher than 4%), causing high compressions in bending test (Si-Larbi et al. 2006). Moreover, local crushing in the matrix may occur before the fiber can be drawn out (Li & Stang 1997), when debonding reaches the hooked end in deformed fibers.

1.3.2.   Plasticity in the fiber

Fibers in cement composite are either brittle (such as glass) or ductile with an initial elastic response (such as steel). For brittle fibers with linear elastic behavior, three parameters are needed to model their mechanical response: E_f, σ_{fu}, ε_{fu}; where E_f stands for the elastic constant (Young's modulus) of the material and the couple $\left(\sigma_{fu},\varepsilon_{fu}\right)$, characterizes the ultimate strength of the fiber under tensile load. In the case of ductile fibers, which are the most common used for structural purposes, a yielding process is well defined, and therefore, two additional parameters are needed: the yield stress σ_{fy} and the corresponding strain ε_{fy} (Naaman 2007a).
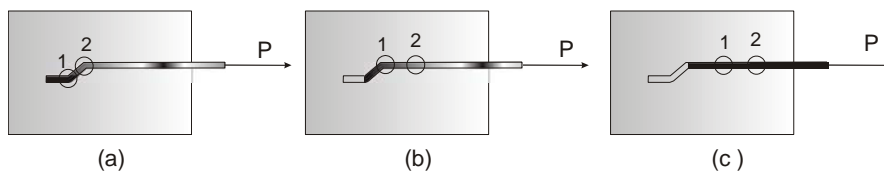
Figure 1.8 Locations of the plastic strain points during elastoplastic-straightening deformation in hooked end fibers. Adapted from (Xu et al. 2010)

Similar to straight steel fiber pullout test, the hooked-end steel fiber pullout process also includes debonding and frictional sliding. However, unlike the straight steel fiber, hooked-end fibers suffers also mechanical sliding that is greatly dominated by elastoplastic straightening deformation of the hooked end (Xu et al. 2010). During the mechanical pullout process, the hooked end steel fiber will be gradually elastoplastically deformed, without

significantly damaging in the surrounding matrix. The Figure 1.8 displays the locations of the points of the plastic strain that exhibit elastoplastic-straightening strain in the pullout process.

1.4.   Modeling approaches

Various models, both numerical and analytical, have been proposed for analyzing composites. The purpose of this section is to review some of these models. Emphasis is initially placed in the models generally used to assess the short fiber reinforced composites. Then, emphasis is given to multiscale approaches and continuum with microstructure, which are briefly explained. It is worth mentioning that, in spite of all the existing information and the actual knowledge about this material, its complex behavior (anisotropy, modes of failure, non-linearities, etc) requires a very deep analysis. Its total understanding still remains an open problem.

The history of modeling composite materials can be divided in two periods. The first one (before computers) is characterized by analytical procedures, particularly, studying the composite substructure, and searching parameters to solve the heterogeneous problem via a suitable homogeneous process. The second period, the advances in computer science originated a continuous development of new methodologies and modeling approaches, which using numerical methods allow simulating the complex behavior of the composite materials. Thus, new models based on computational mechanics, mathematics and engineering, emerge nowadays, in which the mesostructure, or even lower scales, can be considered in the analysis.

1.4.1.   Analytical methods for FRC

The addition of short steel fibers to concrete was reported in 1911 by Graham, but serious studies started in 1920 by Griffith (Rodriguez 1984). However, the interest in composites, for applications in advanced fields of technology, began in the early 1960s and, since then, engineers and scientists exploited seriously the potential of these materials (Herakovich 1998).

Composites can be roughly classified into continuous and discontinuous. It is generally accepted that the properties of short fiber composites (discontinuous composites) are controlled not only by the properties of the compounds and fiber-matrix interface but also by the fiber length, orientation, and fiber dispersion. As for the analysis of discontinuous composites, most models used to predict their mechanical response are derived from those proposed for continuous fiber composites. In the field of composite materials, different approaches may be performed to study the mechanical behavior of the composite material, two of them can be considered as classical : 1) nonlinear constitutive models that describe the composite response taking into account the anisotropy and, 2) Micromechanics models which are frequently used in combination with finite element calculations to provide reference properties of the composite material.

Micromechanics models for short fiber composites include the Eshelby's equivalent inclusion, the self-consistent model for finite length fiber, Mori-Tanaka type models, bounding models, the Halpin-Tsai equation, and shear lag model (Tucker Iii & Liang 1999). Briefly, some of them are described in the following. All these models use the following basic assumptions: 1.The fibers and the matrix are nearly elastic, the matrix is isotropic and the fibers are either isotropic or transversally isotropic. 2. The fibers are axisymmetric, and identical in shape and size. 3. The fibers and matrix are well bonded, and remain in that way during the deformation.

One of the first attempt to model FRC was the *shear lag theory* proposed by Cox (Cox 1952). This model assumes that the load is transferred from a broken fiber to adjacent fibers by the matrix shear forces, which are assumed, in turn, to be independent of the transversal displacements. Hence, the longitudinal and transversal equilibrium equations are uncoupled (Tripp 1989). This theory assumes, in essence that no slip occurs on the fiber-matrix interfaces, and that the presence of the fiber redistributes the stresses and strains within the composite material. The procedure uses two hypotheses: (1) a shear stress occurs at the fiber-matrix interface, and (2) the harder phase carries a comparatively greater part of the stress, while the soft phase tends to take the greater part of the strain (with reference to the volume fraction ratio) (Zhao & Ji 1997).

Hill (Hill 1964) has introduced into the literature the *Hill's concentration factor* approach, which considers the composites consisting of three elastic phases, namely, fiber, matrix and fiber-matrix interface. The average stresses, in every phase, are then expressed in terms of phase-average concentration factors, as developed by Hill. The stress concentration factor is defined as the ratio between the local stress in an intact fiber and the applied stress (Zhou & Wagner 1999). This method takes into account the fracture process of the fiber and the stress concentrations caused by the redistribution of stress from a failed fiber to the intact adjacent neighboring fibers.

Aveston and Kelly (Aveston & Kelly 1973) made meaningful contributions and postulated the *ACK theory* , in order to understand the strain-stress curve and the cracking pattern found in reinforced cement, plasters and other brittle materials. They developed an analytical model for multicracking in composites with continuous aligned fibers, and assumed that the fibers are held up by the matrix only through frictional stresses.

In 1973 *the Mori-Tanaka method* was published (Mori & Tanaka 1973) and it was restated in a more tractable form by Benveniste in 1987 (Eshelby-Mori-Tanaka scheme). Later, the modified scheme (Eshelby-Mori-Tanaka's scheme) was employed to provide accurate approximations of the properties of an aligned short fiber composite. Then, the properties of a misoriented short fiber composite was computed from those of the aligned one, averaging over all possible orientations (Nguyen & Khaleel 2004). All these works were basically conducted on linear behaviors.

The method of cells (MOC) (Aboudi 1989) and its extension, the generalized method of cells (GMC) (Paley & Aboudi 1992), are approximate analytical methods for predicting the elastic as well as inelastic response of fibrous composites. The analysis in this method is limited to a unit cell that includes one fiber and the surrounding matrix material. However, in spite of useful predictive capabilities proven by this method for the response of fibrous composites, it has still some limitations in non-unidirectional composites. Another advantage of

the generalized method is that is able to model specific fiber shape as well as different ar-rangements of fibers in the composite.

1.4.2.   Multiscale models and continuum with microstructure

1.4.2.1. Multiscale Modeling

Multiscale methods make possible to derive and compute phenomena and material parame-ters at macroscopic level from processes that take place one to several scales below. In the multiscale analysis, many scales can be considered, even though, in the study of heterogene-ous media normally is adopted a two scales scheme (Sanchez-Palencia 1987). In multiscale models, a central problem is the scale bridging (Wu 2011), which is a sequential, serial, information-passing or parameter-passing process from one scale to the other. This is often achieved via homogenization techniques. Nevertheless, the computational effort and memory required, has motivated an intensive search for new and improved methods.
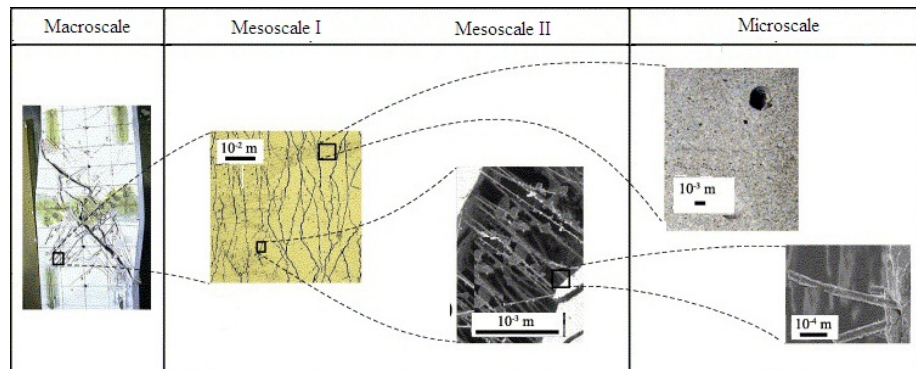
Figure 1.9 Approaches to modeling different scales in materials (Kabele 2007b).

Multi-scale models hinges on the concept of a representative volume element (RVE), which contains numerous substructures on the finer length scale and it is small enough to be viewed as a material point (figure 1.10). Additionally, the RVE is well defined in only two situations: (i) unit cell in a periodic microstructure, and (ii) statistically representative vo-lume containing a very large (mathematically infinite) set of microscale elements (e.g., grains) (Ostoja-Starzewski 2002). So that, it is acceptable, and computationally convenient, to model the material on the large length scale by a spatially uniform constitutive law, which is determined as the relationship between an overall stress and overall deformation of the RVE (Kabele 2007a). In fact, the macroscopic response of the heterogeneous material is obtained from homogenization of the response at smaller (meso, micro) length scales. In the field of structural analysis of composites, the objective of multiscale analysis consists of building an efficient, yet simple, "material" model for the scale chosen. Therefore, to take into account the information at various length scales is required a multiscale solid constitu-

tive model that provides more accurate description of the material, since the conventional phenomenological continuum constitutive models appear to be inappropriate.
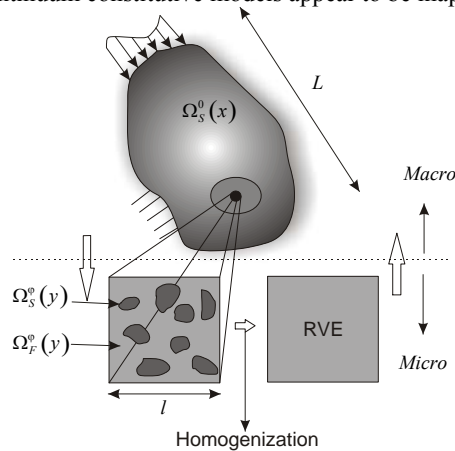
Figure 1.10. Problem to be solved in two scales. Adapted from (Sanz-Herrera et al. 2008)

1.4.2.2. Homogenization theory

In modeling heterogeneous media, it is tempting to adopt a macroscopic point of view, which considers the composite as a homogenized medium with anisotropic properties to be determined (Fish et al. 1997). Basically, the homogenization theory is based on the assumptions of spatial periodicity of the microscopic representative volume elements (RVE) and local uniformity of macroscopic fields within each RVE (Ghosh et al. 2001), as in Figure 1.10. In the mid 70s, methods based on multiple scale asymptotic expansions appeared by the name of mathematical homogenization (Benssousan et al. 1978).

Homogenization approaches are based on the spatial averaging theorem of the classical homogenization theory presented by Suquet in 1986. The main hypothesis in the homogenization procedures is that the heterogeneous media is somehow statistically homogeneous. Under this hypothesis is possible to determine an RVE in the media (Suquet 1987). Several formulations have been proposed in order to obtain the homogenized material properties. By far, the better known of these theories are the spatial averaging and the asymptotic expansion.

In the spatial averaging approach, the average macroscopic properties of the original heterogeneous material are calculated from the characteristic parameters of the microscopical response that, in turn, are obtained using a representative element domain. On the other hand, the asymptotic expansions approach proposed and developed by Sánchez-Palencia (Sanchez-Palencia 1987) and Bensoussan (Bensoussan et al. 1978), consists in a decomposition of the heterogeneous media through asymptotic expansions in scales with different orders of magnitude (Sánchez-Palencia 1986). A rigorous mathematical analysis is carried out to obtain in every scale the strain-stress constitutive equations.

On the other hand, motivated by the nature of the interaction between the compounds in composites, an specific homogenization case was developed by (Trusdell & Toupin 1960c). This is based on the hypothesis of homogeneous strain and is often referred to as the Taylor assumption, but it is also known as the so-called rule of mixtures theory. The two main hypotheses are: 1. all composite constituents are subjected to the same strain (iso-strain assumption) and 2. Each constituent contributes to the composite behavior according to its volumetric participation. The rule of mixtures theory is used to insert the basic constitutive expressions for each substance on the multiphase composite (Oller et al. 1996). However, the main drawback is the iso-strain condition, forcing the parallel distribution of the constituents. In order to outweigh this unfavorable condition, Rastellini (Rastellini et al. 2008) included the serial/parallel theory, eliminating the iso-strain condition.

The homogenization theory, for the analysis of linear elastic fiber reinforced composites, has been successfully applied in conjunction with computer simulations, by means of the finite element method. A vast amount of applications have been reported, for instance Toledano and Murakami (1987), Guedes and Kikuchi (1991) and Devries *et al.* (1989).

1.4.2.3. Continuum with microstructure

Due to the necessity of an enriched geometrical description of the body as the one provided by the usual continuum mechanics, the theory of continua with microstructure was postulated. The Cosserat brothers were the pioneers of this kind of theories. Their ideas were later developed by Ericsen et al. and then by Eringen.

In words of (Mariano 2000), the locution "continua with microstructure" refers to models of bodies where the material texture influence the gross mechanical behavior (macroscale) of the body. Classical examples of these materials are liquid crystals, dislocated continua, micro cracked continua, etc.

Unlike continuum mechanics, in continua with microstructure, mappings into the Euclidean space are still necessary for the description of the body, but other mappings are also expedient to represent into further details of the microstructure (Bongué Boma & Brocato 2010). In other words, the current state of the evolving microstructure is described by global fields of microscopic order parameters and their gradients, which, together with the macroscopic deformation, define the multifield character of the problem under consideration (Welschinger & Miehe 2008). From the theoretical point of view, this is the main difference with respect to multiscale models. Moreover, as it may be surmised, the materials described by means of this approach must satisfy the laws of thermodynamics.

1.4.3.   Fracture mechanics approaches

The main goal of models in fracture mechanics is to determine how a crack grows under certain conditions and whether it remains stable. Displacement discontinuities can either be described as discrete separate entities (discrete fracture mechanics approach), or embedded within the continuum format (continuum mechanics approach). Therefore, fracture mechanics can be divided into two categories, for application in concrete: Discrete and smeared crack models.

Numerical simulation was first applied to problems of concrete cracking by Ngo and Rashid in 1968 (Rashid 1968), who introduced discrete crack and smeared crack models, respectively. Subsequently, it was used extensively to predict the failure mechanisms. Since the beginning of the 1970s, several specific finite elements were developed to capture the discontinuities in the displacement and stress fields. The discrete model is aimed at simulating the initiation and propagation of dominant cracks. In contrast, the smeared crack model is based on the idea that in concrete, due to its heterogeneity and the presence of reinforcement, many cracks nucleate which only in a later stage if the loading process link up to form a more dominant crack. Since each individual crack is not numerically resolved, the smeared crack model captures the deterioration process through a constitutive relation (Borst et al. 2004).

1.4.3.1. Smeared crack model (continuum based models)

In smeared crack models, the crack process is smeared in a region. Rashid (1968) has considered an infinite number of microcracks into the domain of a finite element. Hence, the process can be conveniently modeled by reducing the stiffness in the normal direction of the cracks and being the limit stress given by the tensile strength of the material. Generally, when the combination of stresses satisfies a specific criterion, a crack is initiated.

Although the cohesive zone model is essentially a discrete concept it can be transformed into a continuum or smeared formulation by distributing the work of separation or the fracture energy over the width of an element (Pietruszczak & Mróz 1981). The cohesive crack model was initially proposed by Barenblatt and Dugdale (Dugdale's model). Subsequently, Dugdale's model was reconsidered by (Bilby et al. 1963), Willis (Willis 1967), who referred to it as the final stretch criterion rather than a model. In this model, it is introduced a softening stress-crack opening displacement constitutive law, and the area under the closing stress vs. crack opening displacement curve represents the fracture energy, GF, assumed as a material property. Based on this model, (Hillerborg et al. 1976) proposed the fictitious crack model in order to study crack propagation in concrete. The crack is assumed to propagate when the stress at the crack tip reaches the tensile strength. Additionally, it is considered that the crack can emerge somewhere without a preexistent crack.

In computational practice, the crack band models can be seen as numerical implementation of a cohesive crack model in which the crack opening is smeared over a finite element and the crack band is made of a row of finite elements (Planas et al. 2003). The crack band (Bažant & Oh 1983) uses a softening stress–strain relation, for the material included in a band around the crack (the bandwidth is an additional parameter to be determined) (Carpinteri et al. 2003). It is attractive because it involves only the modification of the classical constitutive relationship without requiring remeshing procedures. This model is based on the observation that microcracking, crack branching, and other toughening mechanism associated with the crack occurring within a fracture process zone, and the width of this zone is typically related to the maximum size of the heterogeneities (Bolander & Sukumar 2005).

The strong discontinuity concept emerged in the works of (Simo et al. 1993), (Armero & Garikipati 1996), and consists of the introduction of a strong discontinuity in the kinematics describing the continua. Although the jump introduced in the displacement field produces

unbounded values in any strain measure involved in the problem, the approach maintains the compatibility between the constitutive equations and the kinematics via the so-called strong discontinuity analysis.

1.4.3.2. Discrete crack model

The discrete crack approach to concrete fracture is intuitively appealing: a crack is introduced as a geometrical entity (Borst et al. 2004). Thus, discrete models describe fracture by means of discrete cracks, which are postulated to exist a priori. The models range from linear elastic fracture mechanics (LEFM) to cohesive crack models (Planas et al. 2003). The discrete crack approach has several disadvantages, being the main in its original version: cracks are forced to propagate along element boundaries, so that mesh bias is introduced. Furthermore, in the standard finite element method, discontinuity has to be placed along the finite element boundaries, and mesh adaptation is required to capture its geometry. Otherwise, displacement discontinuity can be described either at the element level, as in the assumed enhanced strain methods (AES) (Oliver et al. 2006b), or it can be explicitly introduced at the nodal level, as in the partition of unity finite element method (Möes et al. 1999), also known as the eXtended Finite Element Method (XFEM) (Benvenuti 2008).

1.4.4. Some recent approaches in HPFRC composites including cracking and postcracking behavior

High performance fiber reinforced cement composite behavior has been simulated by combining some of the approaches described above. In this section, the most recent contributions in this field are enumerated. They are presented in chronological order to illustrate the evolutionary development of these approaches.

Before 1998, the contributions in HPFRC composites aimed at the characterization of the material and, therefore, a vast amount of experimental results were reported. These studies were conducted to determine the mechanisms that control the mechanical response. Naaman, Li, Banthia and Bentur made remarkable contributions to understanding of short fiber reinforced concrete. Additionally, they made substantial progress in the analytical modeling of these composites based on their experimental results ((Naaman 2007a), (Banthia et al. 1998), (Li 1992)). However, the development of non linear numerical models, encompassing the involved mechanisms in an appropriate manner, does not appear until the late of 1990's.

In 1998, a constitutive model was proposed by (Boulfiza 1998), in which, it was assumed that the continuum damage mechanics (CDM) is able to predict the prepeak branch of the HPFRC composite response and the nonlinear fracture mechanics (NLFM) can predict the postcracking behavior. Then, in 2000, Ferrata Liberato (Ferrara Liberato 2000) presented a non-local damage model, together with a suitable constitutive model that was employed for steel fibers reinforced concrete. The main contribution was a mode I fracture model. A three point bending test on beams of different sizes and different fiber contents were simulated using this model. Another model based on the continuum damage mechanics was the one of

(Peng & Meyer 2000) to describe the inelastic behavior of HPFRC composites and the novelty of this approach is the inclusion of randomly distributed short fibers.

A nonlinear analytical model based on continuum damage mechanics was used by Li and Li (Li & Li 2001) to characterize the tensile stress-strain response, where the governing equation takes into account the damage evolution for both the matrix and the fiber. Furthermore, the damage evolution of the fiber considers the interface zone between the matrix and the fiber. Three years later, Zhang and Li (Zhang & Li 2004) published a model relying on the fracture mechanics approach. They used a superposition method to calculate the crack tip intensity factor. The fundamental parameters in this model were the fracture toughness of the hardened cement paste, the crack bridging law and the stress-crack opening width relationship of the material. In 2007 (Ferreira 2007), also employed a fracture mechanics model to study the fracture behavior of HPFRC composite by using R-curves.

A multiscale approach to model fracture in HPFRC composite appeared in 2007 (Kabele 2007a). He has described each scale and identified dominant substructures and physical mechanisms of deformation. In this analytical/numerical model, interconnections between the models were defined. At the same time, a simplified model to predict the constitutive response of cement composite was suggested in the work of (Naaman 2007a), taking into consideration the precracking state and the postcracking part based on a widely experimental study.

Bolander and coworkers have presented a discrete model with attention to the effects of non-uniform fiber distribution (Bolander et al. 2008). In the simulation, it was utilized a lattice model of the matrix phase of the composite, based on voronoi tessellation. They used a band crack approach and each fiber was explicitly modeled. Another model that considers the contribution of every fiber was the one developed by (Radtke et al. 2010), where fibers were not explicitly discretized, but they were modeled by applying discrete forces to a background mesh. The background mesh represented the matrix, while the discrete forces represented the interaction between fibers and matrix. These forces were assumed to be equal to fiber pull-out forces. More recently, a macroscale plasticity model was proposed by (Sirijaroonchai et al. 2010), which is a phenomenological model capable of representing hardening, softening, and the related cracking and crushing behavior. This model was based on experimental results obtained by the same author.

In the model presented in (Pros et al. 2011), the individual fibers immersed in the concrete bulk are accounted for in their actual location and orientation. The model is based on the immersed boundary (IB) methods, which initially were developed to account for 1D and 2D solids immersed in fluids. Furthermore, the concrete bulk is playing the role of the fluid and the cloud of fibers as the immerse boundary.

1.5.   Aims and scope of the research

The increasing use of short fiber reinforced cement composites in the concrete industry and the limited capacity of the existing models to simulate the response of these materials moti-

vate the formulation of new simulation approaches. Since micro-scale and multiscale models focus on the behavior of the components of HPFRC composites, they have high computational demands, which severely limit their use in applications. Constitutive macroscale models can capture only the overall behavior, but do not provide detailed enough information about the microstructural behavior. Continuum with microstructure, however, can provide details of the incorporated microstructure, and in fact, the balance equations associated with the microfield arise naturally from the theoretical framework. Computational efficiency associated with continuum with microstructure based models will, of course, depend on the numerical scheme adopted to solve the governing equations.

With the above motivation, the main objective of this research is to formulate, develop and implement a numerical model incorporating, what many authors recognize as the principal factor responsible of hardening properties in cement composites, i.e., the debonding process. The continuum with microstructure model formulated within this approach is expected to capture the main macro and microscopic features in the behavior of the material, while still maintaining its applicability even with the use of few model parameters, each identifiable from standard tests. In addition, as the nonlinearity in the material takes place in fiber, matrix and fiber-matrix interface, the continuum with microstructure model, through an adequate homogenization technique, can capture the nonlinear behavior of the overall material. In this regard, thermodynamics plays an important role and, therefore, to avoid unrealistic results, the first and the second laws of thermodynamics should be the basis for the constitutive modeling of the composite material.

The introduction of morphological descriptors to represent details of the microstructure of the body allows us to account directly for the interaction due to substructural effects that may change the stress distribution (Mariano & Stazi 2005). In this way, the continuum with microstructure is a *tool* to construct new models that contain any microstructure and, therefore, it is pursued in this study. The formulation and development of the new model for HPFRC composite using this framework follows procedures established in the multifield theory, which, in turn, satisfies the thermodynamic restrictions.

Also, this research focuses on aspects of the numerical implementation of the new model for HPFRC composite involving numerical issues for simulating fracture. Conclusions drawn from previous studies suggest that the problem remains unsolved and requires additional refinement of the approaching techniques. It is an important issue to propose an appropriate integration scheme for the constitutive model, as well as, a convenient numerical algorithm for the nonlinear finite element analysis. One of the aims of this research is then to propose adequate strategy to solve the set of governing equation of the HPFRC composite.

The introduction of softening in the constitutive model is motivated on theoretical and experimental grounds. However, from the mathematical point of view, softening leads to the loss of ellipticity of the governing partial differential equations in quasi-static analysis that results in ill-posed boundary value problems. Therefore, the solution of the boundary value problem using finite element schemes present several pathological features; the most critical is mesh dependent solutions. Therefore, special treatments such as regularization techniques are required in the resolution of the problem. One of these techniques is based on constitutive model regularization by means of the use of the fracture energy concept and the smeared

crack or crack band models, which can help to remove the mesh dependence. This approach is used in this study.

1.6.   Outline of the research

The chapter 2 of this monography addresses the high performance fiber reinforced concrete as a continuum with microstructure. It presents the continuum with microstructure framework and summarizes the basic concepts of the material multifield theory. The definition of a morphological descriptor associated to the pullout process and defined as the displacement jump introduced by the matrix-fiber slip. Afterwards, the fiber equation is rewritten as a mesoscopic momentum balance equation and the governing differential equations are established in strong and weak forms.

Chapter 2 is also concerned with constitutive models for the components and homogenization techniques employed to obtain the constitutive model of the composite material. The notion of the HPRFC composite as a continuum with microstructure is introduced while the constitutive model satisfies the laws of thermodynamics. Since the classical Taylor or homogenization miscroscopic strain model (also kwon as the rule of mixtures) for composite materials defines a linear relationship between the volumetric fraction of the components, it is necessary to define the individual constitutive material models for the fiber, the matrix and the fiber-matrix interface. In chapter 2, the models representing each compound are described and the homogenization technique is developed in order to obtain a homogenized material constitutive equation amenable to be handled by a finite element methodology.

In chapter 3, the finite element formulation for triangular and quadrilateral elements is developed. Once the governing equations of the continuum with microstructure based model for the HPFRC composite is postulated, a discretization is introduced by using a classical finite element technique. Two types of elements are chosen to discretize the domain, namely, the triangular and the quadrangular elements, both are provided with several degrees of freedom. The first two degrees of freedoms represent the classical displacement vector while the remaining ones represent the slip, in the debonding process, of the fibers in different directions. These aspects of the dicretization of the equations are described in this chapter among others important numerical implementation issues. Two schemes are proposed to integrate along the time the resulting system of equations, namely, a monolithic scheme and a partition scheme. In chapter 4, softening related problems and regularization techniques employed for the treatment of the mesh dependent pathologies are briefly reviewed. The strain injection procedure is introduced to alleviate these problems.

Chapter 5 concerns the numerical validation. A selected set of examples is presented in this chapter. The resultant formulation is verified by simulating the selected examples and by comparing directly the results with the experimental data. Although, the main goal of the current work is to present a new methodology to solve HPFRC composite problems by a novel strategy, the interest is also focused on simulating fracture process in the composite

material and the numerical problems involved. Therefore, it is included into the analysis recent contributions in this regard.

Chapter 2
HPFRC composites as a continua with microstructure

2.1. Introduction

In general, the direct application of macroscale phenomenological models is not able to describe the real phenomena in the HPFRC composite response, which by physical evidence is influenced by events occurring at lower length scales. Alternatively, multiscale modeling provides macroscopic responses at specific material points, by performing a detailed calculation of the RVE, e.g., (Ghosh et al. 1995), (Muliana 2008). This latter approach recognizes changes in the macrostructural geometries and interaction between components during deformation. However, the micro-macro formulations are, in general, computationally expensive, especially when material nonlinearity is also incorporated (Muliana & Haj-Ali 2008). Therefore, an alternative theory that represents this complexity is required, without giving up the advantages of the continuum modeling. One possible way, is to resort to the multifield theory. Thus, it is possible to study a body with some sort of substructure in the context of multifield theory by using a model of continuum with microstructure instead of the classical internal variable scheme. It preserves the well established advantages accruing from the classical scheme of the continuum, and, by introducing morphological descriptors, makes possible the description of the material with a micromorphic structure. The introduction of morphological descriptors, so as to characterize the observed microstructure, follows the general axioms and properties of the theory developed by Capriz (Capriz 1989).

The starting point of the material multifield theory is around 1909, when the brothers E. and F. Cosserat presented a theory of elasticity, in which each element was considered as a

small rigid body that was able to rotate freely with respect to the neighboring material. Later on, J.L. Ericksen and C.A. Truesdell extended Cosserat's ideas, in order to construct models in elastic structures (Ericksen 1974). In 1964, Mindlin (Mindlin 1964) introduced the idea that the material element deforms independently of other body parts. Thus, he developed a more relevant elastic theory in a linear setting. Materials described by both Cosserat and Mindlin' proposals required morphological descriptors, or order parameters, to include the "internal" substructure. Thus, many applications were presented in a variety of situations, such as ferroelectric materials, micromagnetic materials, etc, which used order parameters of different natures (i.e. tensors, vectors) to describe the microstructure.

In the 70's, the interest of researchers was directed toward unifying the existing multi-field models. This task was initiated by Capriz in the late of 1980's (Capriz 1989). His work deals with the construction of a general model-building framework, which is able to describe the influence of the substructural changes in the complex materials. Recently, new contributions deal with the application of the complex bodies' theory in computational mechanics for different materials, among others (Svendsen 2001), (Mariano & Stazi 2005), (Trovalusci & Masiani 2005), (Mariano 2008a), (Mariano 2008b), (Mariano 2007), (Mosconi 2005), etc.

Therefore, a formulation based on the continuum with microstructure is presented in this chapter, in order to provide the HPFRC composite with an "internal" morphology. The motivation of a formulation inspired in this theory is the fact that, in the micro level of these composites, takes place several micro processes. The most relevant one is the pullout of the fiber, which produces "*bridging effect*" in the presence of microcracks. The morphological descriptor equips the fiber-matrix interface with a slipping property that is defined as the ability to transfer the stresses through the fiber-matrix interfacial transition zone and to resist against slip between fiber and matrix. Thus, the model is thought to be able to transmit the micromechanical effects of the fiber into the general response of the composite.

The material model captures geometrical details and the distinct material behaviors, existing in the structural member. It should also be able to capture localized macrocracks, which occur in these composites after its hardening capacity is exhausted (Kabele 2007a).

2.2.   General elements of the multifield theory

A material with a micromorphic structure is such that its substructure, from nano to meso-level, influences dramatically its gross behavior and, in which, interactions due to substructural changes are prominent. Therefore, we expect that, in the model used for such material, the substructural interacting mechanisms modify the mechanical response of the body. The mechanics of micromorphic materials is a theoretical framework to construct material models with substructures (Mariano & Stazi 2005) and incorporate morphological descriptors into the continuum formulation. In consequence, we can use this framework to create a model that represents the HPFRC composite. It has to be understood as a continua with different material levels. In general, one or more microstructural levels are presented, which are cha-

racterized by the presence of additional descriptors. However, only one morphological descriptor will be included in our model, that accounts for the fiber-matrix sliding mechanism.

The only objective that we pursue in the following sections is to introduce the necessary ingredients providing the background for the posterior development of the HPFRC two-scale material model. Delicate additional details of this theory can be found in the mentioned papers of Mariano and Capriz.

2.2.1.   The concept of a body according with the continuum mechanics and with continua with microstructure

In (Holzapfel 2000), it is presented the classical definition of a body according to the continuum mechanics, as follows.

"A body is a collection of material elements whose morphology is identified just by their place in the space, such that a material element is represented as a material point".

In this way, the geometrical description of the body skips details about the minute substructure. Moreover, in most of the analysis in continuum mechanics, a further assumption about the nature of the material is made, namely, that it is homogeneous.

However, in a real body, a material element is not properly a simple point, rather a system of interacting substructures. Thus, according to the mechanics of continua with microstructure's definition, a material element is a continuum endowed with some sort of local microscopic order.

> Micromorphic solids are continuum mechanics models, which take into account, in some sense, the microstructure of the considered real material. The characteristic property of such continua is that the state functions depend, besides the classical deformation of the macroscopic material body, also upon the deformation of the microcontinuum modeling the microstructure, and its gradient with respect to the space occupied by the material body (Grammenoudis & Tsakmakis 2009).

Then, Capriz has noted that it is needed to associate, to each material element, a number of "order parameters" to describe the morphology of this microscopic system (Capriz & Mariano 2001). In the works of Mariano ((Mariano 2007), (Mariano & Stazi 2005)), these order parameters are presented as *morphological descriptors*. This enables the classical scheme of the continuum to include the effect of the microstructure.

Regarding the continuum theory, the fundamental assumption establishes that a body, denoted by $\mathfrak{B}$, may be viewed having a continuous distribution of matter, in space and time. The body is imagined as being a composition of a set of particles, X , as indicated in Figure 2.1. On the other hand, in order to characterize the observed microstructure in the multifield

model, each particle is associated to a certain number (i.e., m) of "order parameters" β^{α} $(\alpha = 1, 2, ..., m)$.

2.2.2.   Configuration space and motion

Let us consider a body $\mathfrak{B}$ with a reference placement $\mathfrak{B}_0$ in the three dimensional Euclidean space, as indicated in Figure 2.1, undergoing a quasi-static loading process given by a set of generalized external forces, which are going to be defined in the following. Parameter t represents a pseudo-time defining the sequence of increasing external loads.

In this theory, it is defined a right-handed reference frame, rectangular coordinate axes at fixed origin O with orthogonal basic vectors. In the classical approach,

$$\mathbf{x} = \tilde{\mathbf{x}}(\mathbf{X}, t), \; \forall \mathbf{X} \in \mathfrak{B}_0 \quad \forall t \in [0, t] \tag{2.1}$$
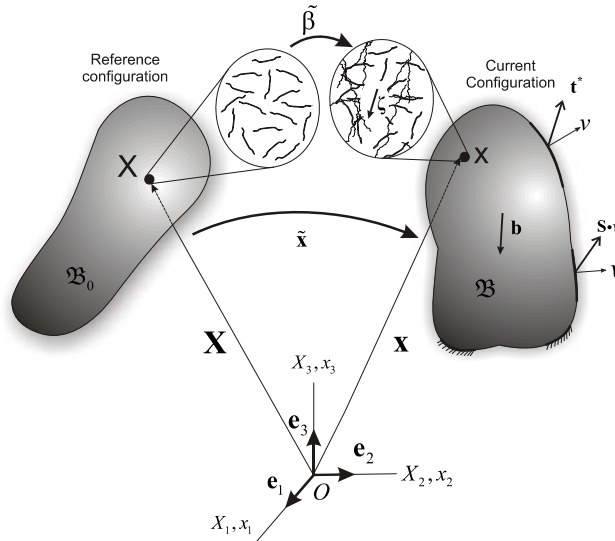
Figure 2.1. Configuration space during the body motion defined in the context of a multifield theory. Spatial placement is described by the map $\tilde{\mathbf{x}}$, while the micromorphic field $\boldsymbol{\beta}$ provides additional information about the material point mesostructural state.

The map $\tilde{\mathbf{x}}$, specifying the place $\mathbf{x}$, is called the *motion* of the body. Nevertheless, The key idea of a material multifield theory is to assign to each material point $\mathbf{X}$, of $\mathfrak{B}_0$, the pair $(\mathbf{x}, \boldsymbol{\beta})$ that completely defines the configuration space of the body. The first element of the pair, $\mathbf{x}$, specifies the placement in the Euclidean space of the material particle $\mathbf{X}$ for all t, and the second one, $\boldsymbol{\beta}$, is a morphological descriptor providing information about the microstructure configuration.

In the micromorphic materials' theory, the morphological descriptor β^α can be interpreted as coordinates (in a local chart of an atlas) of an element β in an appropriate manifold $\mathcal{M}$ of dimension m. Different physical circumstances may require different descriptors, of different mathematical natures. Moreover, for the same material substructure, different morphological descriptors can be chosen. Thus, often the chosen manifold $\mathcal{M}$ has a physical meaning, for instance, it could be a scalar field representing the void fraction in a continuum or a unit vector characterizing the orientation in liquid crystals (Mariano 2008b).

The pair $(\mathbf{x}, \boldsymbol{\beta})$ is sketched in Figure 2.1. For the micromorphic material theory, the representation of motion also includes the morphological description map: $\tilde{\boldsymbol{\beta}}$. Thus, in our picture, the *motion* is given by

$$\mathbf{x} = \tilde{\mathbf{x}}(\mathbf{X}, t) = \mathbf{X} + \mathbf{u}(\mathbf{X}, t), \forall \mathbf{X} \in \mathcal{B}_0 \quad \forall t \in [0, T]$$

$$\boldsymbol{\beta} = \tilde{\boldsymbol{\beta}}(\mathbf{X}, t), \forall \mathbf{X} \in \mathcal{B}_0 \quad \forall t \in [0, T]$$

(2.2)

where the vector field $\tilde{\boldsymbol{\beta}}$ specifies the values of the morphological descriptor at time t. $\mathbf{u}$ represents the displacement of the particle $\mathbf{X}$ and T the final pseudo-time where the analysis ends.

The micromorphic material theory also requires that the morphological descriptor $\boldsymbol{\beta}$ be an element of a differentiable manifold. During the motion, the velocity $\dot{\mathbf{x}}$ and the rate of change of the microstructure $\dot{\boldsymbol{\beta}}$ (also called, micro-velocity) are given by,

$$\dot{\mathbf{x}} = \frac{d\tilde{\mathbf{x}}}{dt}(\mathbf{X}, t)$$

(2.3)

$$\dot{\boldsymbol{\beta}} = \frac{d\tilde{\boldsymbol{\beta}}}{dt}(\mathbf{X}, t)$$

Hence, the spatial field of the morphological description is $\boldsymbol{\beta}_a = \tilde{\boldsymbol{\beta}} \circ \tilde{\mathbf{x}}^{-1}$, such that $\boldsymbol{\beta}_a = \tilde{\boldsymbol{\beta}}_a(\mathbf{x}, t)$. Besides, the spatial counterparts of the material rates $\dot{\mathbf{x}}$ and $\dot{\boldsymbol{\beta}}$, are $\mathbf{v} = \tilde{\mathbf{v}}(\mathbf{x}, t)$ and $\upsilon = \tilde{\upsilon}(\mathbf{x}, t)$, respectively.

In classical continuum mechanics, the material tangent vectors map into spatial tangent vectors via the deformation gradient $\mathbf{F}$. The microstructure requires also a gradient $Grad\,\boldsymbol{\beta}$, in order to map material tangent vectors at $\mathbf{X}$ into tangent vectors at $\boldsymbol{\beta}$ ($\boldsymbol{\beta} \in \mathcal{M}$). The spatial gradient is denoted $\nabla \boldsymbol{\beta}$ and by the chain rule, it is $\nabla \boldsymbol{\beta} = (Grad\,\boldsymbol{\beta})\mathbf{F}^{-1}$.

2.3.   Balances equations

An additional and relevant aspect of the theory is to consider the possible bulk and contact forces representing interactions of the morphological descriptor $\boldsymbol{\beta}$. These interactions produce an explicit power through the action of microforces $\boldsymbol{\zeta}$ acting on particles having the rate $\dot{\boldsymbol{\beta}}$, in a similar way as the conventional body forces $\mathbf{b}$ (per unit of volume) produce power through their action on particles with velocities $\dot{\mathbf{x}}$. Additionally to the power ex-

pended by the generalized forces $\mathbf{b}$ and ζ, it shall be considered those terms taking into account the power expended by the conventional surface tractions $\mathbf{t}^* = \boldsymbol{\sigma} \cdot \mathbf{v}$ acting on the boundary Γ_σ of $\mathfrak{B}$, and the power expended by microstructural surface tractions: $\mathbf{S} \cdot \mathfrak{V}$, due to microstresses $\mathbf{S}$, acting on the boundary Γ_S of $\mathfrak{B}$. In both cases, $\mathbf{v}$ is the outward normal vector to the body boundary. Thus, the general expression of the external power P^{ext}, according to the micromorphic material theory is,

$$P^{ext}\left(\dot{\mathbf{x}},\dot{\boldsymbol{\beta}}\right) = \int_{\mathfrak{B}} \left(\mathbf{b}\cdot\dot{\mathbf{x}} + \boldsymbol{\zeta}\cdot\dot{\boldsymbol{\beta}}\right) d\Omega + \int_{\Gamma_\sigma} \mathbf{t}^*\cdot\dot{\mathbf{x}} \; dA + \int_{\Gamma_S} \left(\mathbf{S}\cdot\mathbf{v}\right)\cdot\dot{\boldsymbol{\beta}} \; dA \tag{2.4}$$

The consequence of considering the interactions of the morphological descriptors in (2.4) through ζ and $\mathbf{S}$ is that additional, non-conventional, balance equations arise in the model. They are derived from the external power P^{ext} by considering the invariance of (2.4) under arbitrary observer changes. It is shown by Mariano (Mariano & Stazi 2005) that this equation has the following form,

$$\begin{aligned} \nabla\cdot\boldsymbol{\sigma} + \mathbf{b} &= \mathbf{0} \\ \nabla\cdot\mathbf{S} - \mathbf{z} + \boldsymbol{\zeta} &= \mathbf{0} \end{aligned} \qquad \forall\, \mathbf{X} \in \mathfrak{B}_0 \tag{2.5}$$

In equation (2.5)-a, $\boldsymbol{\sigma}$ is the conventional Cauchy stress tensor. Then, local balance equation (2.5)-a is the classical Cauchy equation, when inertial forces are neglected. Equation (2.5)-b is the local balance of the substructural actions, this equation is called *Capriz balance*.

A new object $\mathbf{z}$ arises in (2.5)-b, which can be interpreted as a continuously distributed micromorphic force. An additional balance equation, which can be seen as a generalized angular momentum balance, connecting the skew part of $\boldsymbol{\sigma}$ with $\mathbf{S}$ and $\mathbf{z}$ is derived in the theory. In Appendix I, we show that, after considering the HPFRC model that shall be presented in the following Section, this equation trivially prescribes the symmetry of the stress tensor $\boldsymbol{\sigma}$.

The use of the Green theorem and the balance equations (2.5) in P^{ext} establishes the following identity:

$$P^{ext} = \int_{\mathfrak{B}} \left(\boldsymbol{\sigma}:\nabla^s\dot{\overline{\mathbf{u}}} + \mathbf{z}\cdot\dot{\boldsymbol{\beta}} + \mathbf{S}:\nabla\dot{\boldsymbol{\beta}}\right) d\Omega = P^{\text{int}} \tag{2.6}$$

where the right part of (2.6) represents the total internal power: P^{int}. Note that $\mathbf{z}$ and $\mathbf{S}$ play the role of generalized forces conjugate to $\dot{\boldsymbol{\beta}}$ and $\nabla\dot{\boldsymbol{\beta}}$, respectively.

2.3.1.   Constitutive constraints

The materials described using this theory must satisfy the laws of thermodynamics, in particular the second one. Furthermore, we consider the material free energy density $\psi(\nabla^s\mathbf{u}, \boldsymbol{\beta}, \nabla\boldsymbol{\beta}, \boldsymbol{\alpha})$, where for simplicity, the analysis is restricted to isothermal case. The variable $\boldsymbol{\alpha}$ denotes the possible dependence of the constitutive response with a set of internal variables.

The isothermal version of the second law of thermodynamics prescribes, for any arbitrary deformation path, the verification of the following inequality:

$$\dot{\psi} - P^{\text{int}} = \dot{\psi} - \left(\boldsymbol{\sigma} : \nabla^s \dot{\bar{\mathbf{u}}} + \mathbf{z} \cdot \dot{\boldsymbol{\beta}} + \mathbf{S} : \nabla \dot{\boldsymbol{\beta}} \right) \leq 0 \, . \tag{2.7}$$

For admissible (arbitrary) choices of $\nabla^s \dot{\bar{\mathbf{u}}}$, $\dot{\boldsymbol{\beta}}$ and $\nabla \dot{\boldsymbol{\beta}}$. Equation (2.7) establishes the following identities for every one of the generalized forces:

$$\boldsymbol{\sigma} = \frac{\partial \psi}{\partial \nabla^s \mathbf{u}} \quad ; \qquad \mathbf{S} = \frac{\partial \psi}{\partial \nabla \boldsymbol{\beta}} \quad ; \qquad \mathbf{z} = \frac{\partial \psi}{\partial \boldsymbol{\beta}} \tag{2.8}$$

in fact, these identities are considered as constitutive constraints in the material model formulation.

2.3.2.   The morphological descriptor β as fiber-matrix slip during the debonding process

Let us take a closer look at the composite material and restrict our attention to the phenomenon sketched in Figure 2.2, that represents a block of HPFRC composite undergoing a loading process described by the force $\mathbf{P}$. One plausible description of the mesostructure considers a cell containing a fiber, the surrounding matrix material and the interfacial transition zone (ITZ) between the two compounds, as illustrated in the Figure 2.2-b. The ITZ is understood as a shell with zero thickness. The mechanical description, taking place in this simplified mesostructural cell, can be imagined as follows: the fiber is subjected to an axial stress σ^f, and a bond shear stress τ^f arises in the interfacial transition zone (ITZ). The last action has the effect of interconnecting the concrete-fiber mechanical response and it is not null only if a relative displacement, slip motion, between fiber and concrete happens. Therefore, the mesostructure is defined by the processes occurring in the fiber and the interfacial zone.

In order to take into consideration this mesoscopic phenomenon, we introduce a continuous microfield, $\boldsymbol{\beta}$, representing the relative displacement between fiber and matrix, i.e. the bond slip mechanism. In the context of a multifield theory, $\boldsymbol{\beta}$ represents a morphological descriptor and it is a new variable that must be determined.

2.3.3.   Hypothesis of the model

The heterogeneity of the HPFRC composite entails a large number of variables because of the random nature of the fiber distribution. In general, the fibers in HPFRC composites are randomly oriented in the bulk material. Nevertheless, it could be inappropriate to model each fiber separately. Some researchers have concluded, by experimental results, that both, pullout and bond-slip, relations are sensitive to the fiber orientation ((Laranjeira et al. 2010), (Leung & Geng 1998)). Additional investigations pointed out that the peak pullout load of an inclined fiber is almost as high as that of an aligned one. However, the work required to completely remove an inclined fiber is higher, if compared with the aligned one ((Naaman A. E 1976), (Cunha et al. 2007)).
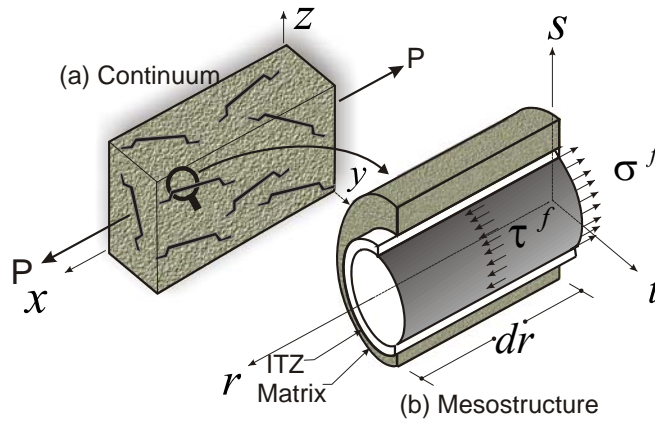
Figure 2.2. The HPFRC composite. (a) The HPFRCC and (b) the idealized mesostructure.

In addition, the number of fibers per unit volume of composite is a random parameter that affects the tensile strength behavior, and frequently is assumed as a probability distribution function to designate the number of fibers in an elemental point. Nevertheless, we assume that this component could be well represented by a discrete number of fiber bundles; each bundle being oriented in a specific direction and representing the set of fibers which are almost parallel to the fiber bundle. Then, the contribution of each bundle to the total response is given by their volumetric participation. The unit vectors $\mathbf{r}^{ifib}$ and $\mathbf{s}^{ifib}$ are associated to a given bundle orientation as is shown in Figure 2.3.

Figure 2.3. Kinematics at microstructural level.

In order to do the model feasible, we introduce some basic assumptions, as follows:

(i)   Even when the equations are written in a three-dimensional format, the numerical analysis is reduced to plane strain and stress cases. Small deformation theory and static loading process are assumed. Furthermore, the matrix, fibers, external forces and external displacements are contained in the plane $z = 0$. The real volume fraction of the fibers in the section of interest is obtained by affecting it with the orientation number, which is defined as the average length of the projection on the longitudinal axis of all fibers crossing a section, divided by the fiber length (Dupont & Vandewalle 2005).

(ii)   Any point of the HPFRC composite behaves as a micromorphic material. The continuum (HPFRC composite) at every point has an associated microstructure (fiber and the surrounding matrix), which is represented by the Capriz balance equation.

(iii)   The composite is defined as a homogeneous continuum in which each infinitesimal volume is occupied simultaneously by all the constituents, including fibers bundles in all direction exiting in the composite at the point, in a proportion given by the volume fraction of the component.

(iv)   Several families of short fibers, or fiber bundles, are considered in the formulation. Each family is oriented an angle θ respect to the global x-axis. We assume that the fiber random orientation is well represented by these fiber bundles, without underestimating or over sizing the problem. Each fiber does not interact with the neighboring fibers, nor, one bundle, in a given direction, interacts with another in a different direction.

(v)   after initiation of concrete cracking, the dowel effect induced by the fiber is neglected;

(vi)   The analysis of the continuum with microstructure is restricted to the isothermal case.

The first assumption ignores the spatial distribution of the composite material, which affects specially the fiber effectiveness in the case of short steel fibers composites. This assumption may be too coarse for adequately capture the mechanical behavior of the material. In fact, experimental research has shown that there is a high degree of proportionality between the toughness and the fibers crossing a section (Dupont & Vandewalle 2005). This drawback motives the use of an orientation factor, as defined in (Dupont & Vandewalle 2005). The orientation factor is the average length of the projection on the longitudinal axis of all fibers crossing a section. It is claimed in (Dupont & Vandewalle 2005) that the application of this simplification provides results which agrees well with the real cases.

2.3.4.   Configurational space and kinematical description of the composite

Let us consider a single fiber undergoing a tensile loading process, as depicted in Figure 2.4-(a). Also, let us consider a local cartesian system, $(\mathbf{r}, \mathbf{s}, \mathbf{t})$, with the r-axis being parallel to the fiber. The present model assumes one local cartesian system for every fiber bundle in the material.

Figure 2.4 (b-c) depicts the deformation mechanism of fiber and matrix, in a given Section A-A' parallel to the plane $(\mathbf{s}, \mathbf{t})$. During the initial loading stage, Figure 2.4-(b), it is supposed that both components, the matrix and the fiber, are perfectly joined, there is not slip between both components. Thus, the same displacement $\bar{\mathbf{u}}$ describes the kinematics of the composite. Specifically, the r-component of the displacement vector: $\bar{u}_r$, is identical for both

components. In this Figure, the dashed lines is used to indicate the initial (undeformed) position of the Section A-A', while the solid line shown the deformed position.

As the tensile stress increases, the bond shear strength is reached. Then, a second stage is observed, as shown in Figure 2.4-(c), in which the pull out mechanism activates the progressive failure in the ITZ, here the transition surface is denoted with Γ, inducing a relative motion (slip) between the two phases.
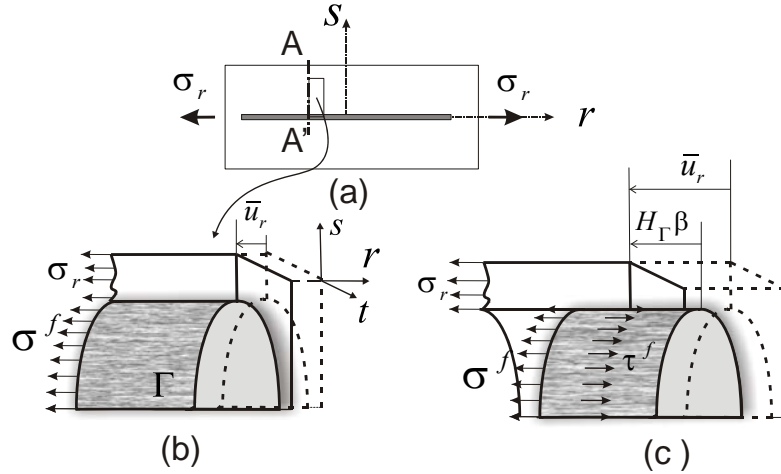
Figure 2.4. Kinematics at mesostructural level.

While the matrix undergoes a displacement $\overline{\mathbf{u}}$, relative to the original position, the fiber moves a distance $\overline{u}_r + \mathcal{H}_f \beta$ in the r-direction, where $\mathcal{H}_f$ is the Heaviside's function taking values 0 and 1 for the matrix and fiber domains, respectively. Then, the displacement field $\mathbf{u}(\mathbf{x})$ in the composite domain is defined as follows:

$$\mathbf{u} = \overline{\mathbf{u}} + \mathcal{H}_f \boldsymbol{\beta} \quad ; \qquad \mathcal{H}_f \begin{cases} =0 & \text{concrete} \\ =1 & \text{fiber} \end{cases} \tag{2.9}$$

The morphological descriptor in the coordinate system $(\mathbf{r}, \mathbf{s}, \mathbf{t})$ is characterized by the scalar β, which is the r-component of the vector $\boldsymbol{\beta}$, and with the remaining components equal to zero:

$$\boldsymbol{\beta} = \beta(r, s, t)\mathbf{r} \tag{2.10}$$

Without loss of generality, from now on we assume two dimensional problems with plane symmetry described in the plane $(\mathbf{r}, \mathbf{s})$; the assumed geometry of the reinforcement is such that preserves this symmetry. Then, $\nabla \boldsymbol{\beta}$ is given by:

$$\nabla \boldsymbol{\beta} = \beta_{,r}(\mathbf{r} \otimes \mathbf{r}) + \beta_{,s}(\mathbf{r} \otimes \mathbf{s}) \tag{2.11}$$

where we use the notation $(\bullet)_{,r} = d(\bullet)/dr$ and $(\bullet)_{,s} = d(\bullet)/ds$

The description of the deformation field is derived from equation (2.9). as follows:

$$\boldsymbol{\varepsilon} = \nabla^s \mathbf{u} = \nabla^s \overline{\mathbf{u}} + \delta_\Gamma (\boldsymbol{\beta} \otimes^s \mathbf{s}) + \mathcal{H}_f (\nabla^s \boldsymbol{\beta}) =$$
$$= \nabla^s \overline{\mathbf{u}} + \delta_\Gamma \beta (\mathbf{r} \otimes^s \mathbf{s}) + \mathcal{H}_f (\beta_{,r} (\mathbf{r} \otimes^s \mathbf{r}) + \beta_{,s} (\mathbf{r} \otimes^s \mathbf{s})) \tag{2.12}$$

where, the supra-index $(\bullet)^s$ refers to the symmetric part of the corresponding second order tensor. The second term in the right hand side is obtained after using the generalized gradient: $\nabla \mathcal{H}_f = \delta_\Gamma \mathbf{s}$, with δ_Γ being the Dirac delta function placed in Γ (the ITZ surface). Thus, the strain in the matrix (where $\mathcal{H}_f = 0$) is:

$$\boldsymbol{\varepsilon}_m = \nabla^s \overline{\mathbf{u}} ; \tag{2.13}$$

while the fiber strain results:

$$\boldsymbol{\varepsilon}_f = \mathcal{H}_f \left(\nabla^s \overline{\mathbf{u}} + \beta_{,r} (\mathbf{r} \otimes^s \mathbf{r}) + \beta_{,s} (\mathbf{r} \otimes^s \mathbf{s}) \right) \tag{2.14}$$

which depends on both the matrix displacement and the slip in the ITZ. Finally, the remaining term in equation (2.12) is:

$$\boldsymbol{\gamma} = \delta_\Gamma \beta (\mathbf{r} \otimes^s \mathbf{s}) \tag{2.15}$$

which can be interpreted as a singular shear strain concentrated in the ITZ surface.

2.4.   Integral expression of the microscopic momentum balance equation

From the above free energy expressions, and considering the strains (2.12)-(2.15) and the constitutive constraints (2.7); the generalized stresses are given by:

$$\boldsymbol{\sigma} = \frac{\partial \psi}{\partial \nabla^s \overline{\mathbf{u}}} = k_m \frac{\partial \psi_m}{\partial \nabla^s \overline{\mathbf{u}}} + k_f \frac{\partial \psi_f}{\partial \nabla^s \overline{\mathbf{u}}} = k_m \left(\frac{q_m}{r_m} \mathbb{C}_m \cdot \boldsymbol{\varepsilon}_m \right) + k_f \mathbb{E}_f \cdot \boldsymbol{\varepsilon}_f^e =$$
$$= k_m \underbrace{\left(\frac{q_m}{r_m} \mathbb{C}_m \cdot \boldsymbol{\varepsilon}_m \right)}_{\boldsymbol{\sigma}_m} + k_f \underbrace{E_f \left((\overline{u}_r)_{,r} + \beta_{,r} \right)^e (\mathbf{r} \otimes \mathbf{r})}_{\boldsymbol{\sigma}_f} = k_m \boldsymbol{\sigma}_m + k_f \boldsymbol{\sigma}_f \tag{2.16}$$

where we identify $\boldsymbol{\sigma}_m$ as the conventional concrete stress and $\boldsymbol{\sigma}_f$ as the (uniaxial) fiber stress. The microstress is given by:

$$\mathbf{S} = \frac{\partial \psi}{\partial \nabla \boldsymbol{\beta}} = k_f \frac{\partial \psi_f}{\partial \nabla \boldsymbol{\beta}} = \mathcal{H}_f \left(k_f \mathbb{E}_f \cdot \boldsymbol{\varepsilon}_f^e \right) = \mathcal{H}_f k_f E_f \left((\overline{u}_r)_{,r} + \beta_{,r} \right)^e (\mathbf{r} \otimes \mathbf{r}) = \mathcal{H}_f k_f \boldsymbol{\sigma}_f \tag{2.17}$$

where, from (2.17), we recognize that $\mathbf{S}$ coincides with the stress $\boldsymbol{\sigma}_f$ in the fiber domain while being zero in the remaining part of the volume. The micromorphic force results:

$$\mathbf{z} = \frac{\partial \psi}{\partial \boldsymbol{\beta}} = k_f \frac{\partial \psi_\Gamma}{\partial \boldsymbol{\beta}} = \delta_\Gamma \left(k_f \mathbb{G}_\Gamma \cdot \boldsymbol{\beta}^e \right) = \delta_\Gamma \left(k_f \underbrace{E_\Gamma \beta^e}_{\sigma_{rs}} \right) \mathbf{r} = \delta_\Gamma k_f \sigma_{rs} \mathbf{r} \tag{2.18}$$

where, due to the coefficient δ_Γ, this term can be identified with the shear stress acting in the ITZ.

Without loss of generality, we are assuming from now on that the external microforce $\zeta = \mathbf{0}$.

To understand more precisely the role played by the microstress balance law (2.5)-b, and considering that $\mathbf{S}$ and $\mathbf{z}$ are defined in the fiber and ITZ regions, respectively, it is more natural to define an integral expression of this balance equation. Let us integrate this expression in the body part $\mathscr{P}_B$ coinciding with the cylindrical slice of length dr enclosing a fiber and its associated ITZ surface, such as shown in the insert of Figure 2.5. The integral expression results:

$$\int_{\mathscr{P}_B} (\nabla \cdot \mathbf{S} - z)\, d\Omega = \begin{bmatrix} \int_{\Omega^f} \left((\sigma_{rr})_{,r} + (\sigma_{rs})_{,r} \right) d\Omega^f \\ 0 \end{bmatrix} - \begin{bmatrix} \int_\Gamma \sigma_{rs}\, d\Gamma \\ 0 \end{bmatrix} = \begin{bmatrix} 0 \\ 0 \end{bmatrix} \quad ; \qquad (2.19)$$

where the second identity is found by replacing equations (2.17) and (2.18) in the left side term. As can be seen, the second component of the vectorial equation is trivially equal to zero. Thus, the relevant balance equation comes from the first component of (2.19). Note that due to the presence of the Heavisde function coefficient in (2.17), the integration domain of the first term is restricted to the fiber volume here denoted: Ω^f; while the integration domain in the second term corresponds to the ITZ surface due to the Dirac function in (2.18).
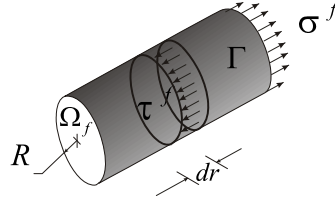
Figure 2.5. Fiber segment with the integration domains and the substructural actions.

Considering from the previous Section that $\sigma_{rs} = 0$ in the fiber, denoting σ^f the average value of σ_{rr} in a given section of the fiber and τ^f the average shear stress σ_{rs} in a circumferential section of Γ, expression (2.19) can be alternatively expressed as:

$$\Pi_f \tau_f - A_f (\sigma_f)_{,r} = 0 \qquad (2.20)$$

where, A_f and Π_f are the cross-section area and the perimeter of the fiber, respectively. A similar equation describing the relation between the axial stress and the shear stress distribution at the interface zone was presented by Naaman and coworkers (Naaman et al. 1991). As it was mentioned above, there exists one balance equation (2.20) for every fiber bundle which is characterized by the direction vector $\mathbf{r}^i$.

The equation (2.20) describes the stress distribution along the fiber in HPFRC composite, specifically, the axial stress and the interfacial shear stress distribution. In this regard, it can be distinguished two cases, namely, a debonding process with a no cracked matrix and a debonding process with a cracked matrix (Leung & Li 1990). The two cases are depicted in figure 2.6.

In the first process (Figure 2.6.a.), The failure is initiated by concentration of the shear stress in the interfacial zone, causing debonding first at the ends of the fiber and activating the slip process (stage 1). After enough slip, the shear bond stress exceeds the maximum shear capacity (stage 2). And finally, the ultimate bond strength is reached along the whole fiber (stage 3). In this stage, the fiber could either slide out or be removed completely, if frictional resistance remains in the ITZ, or any resistance is offered, respectively. In last case, the composite action is not achieved.
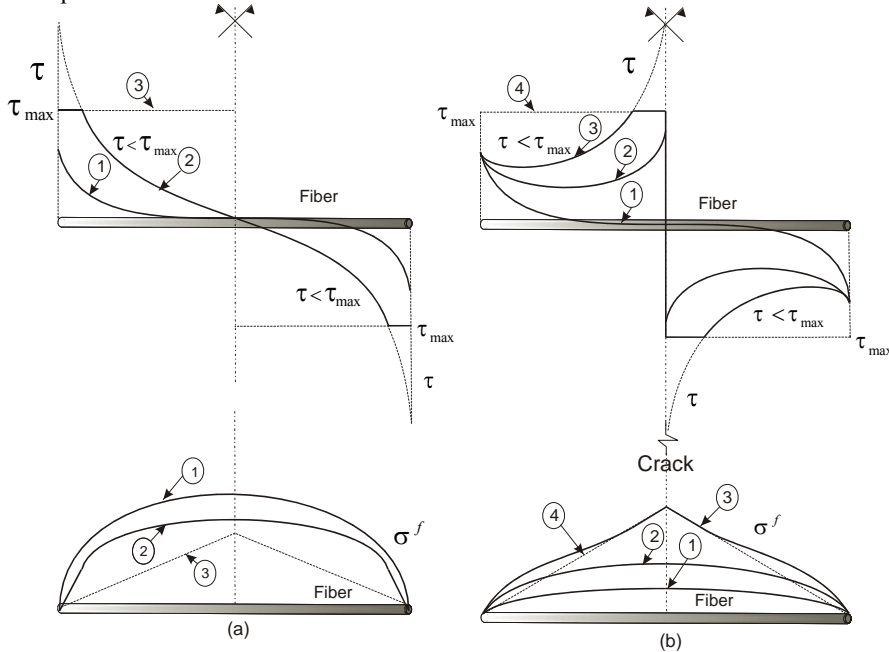
Figure 2.6. Typical bond shear stress distribution at fiber-matrix interface and axial stress distribution along the fiber before and after debonding: a) matrix without cracks; b) matrix with a crack.

The second case is depicted in figure 2.6.b. Before cracking (stage 1), the interfacial transition zone is intact and as a consequence, the maximum shear stress concentrates at the ends of the fiber while the axial stress at this point is zero and maximum in the middle length (Oller 2003). In the post-cracking stage (stage 2), the fibers transfer the stress through the interfacial zone and the shear bond stress reaches its maximum value at the crack surface. After that, the fiber is pulled out from the matrix, but the maximum shear-bond-stress capacity, along the ITZ, has not been reached. As soon as it is exceeded, two interfacial zones coexist, one that is bonded and other that is debonded (stage 3) (Naaman et al. 1991). In last stage (stage 4) the total fiber length is debonded and the shear bond stress reaches a constant value whether a perfect elastic-plastic relationship is assumed between the shear stress and the slip. In the same figure, axial stress distributions along the fiber length, in all stages, are

shown. In the present model, it is noted that the fiber end interfaces have not any mechanical effect.

2.5.   Constitutive models and homogenization of the equations by the rule of mixtures theory

A general constitutive equation can be obtained for the whole composite, disregarding the complexity that exists at lower scales. In several works, macroscale phenomenological models have been developed and used to describe the HPFRC composite behavior (see, for instance (Coto Roquet 2007), (Kulla 1998), (Wittel et al.) and (Sirijaroonchai 2009)). Nevertheless, they may produce an inadequate answer of the material behavior, if the microstructure has an important effect in the composite response.

In the HPFRC composites, the combined effects of the compounds control the mechanical response under an applied stress. From the mathematical point of view, this composite shows a very marked non-linear response being the main sources of nonlinearities fundamentally due to the material non-linear behavior of the compounds. Additionally, several parameters and mechanisms, including fracture toughness of the composite, fiber pull-out behavior, fiber parameters, and bridging effect, should be taken into account (Fischer 2006). Therefore, the constitutive equation that is required to describe the material response must depend on the properties of the matrix, the fiber and the interfacial transition zone.

The methodology adopted herein, for the constitutive analysis of the composite material, uses the hypothesis of homogeneous strain that is often referred to as the Taylor assumption, but it is also known as the so-called rule of mixtures theory (Trusdell and Toupin (1960)). Although the rule of mixtures theory does not take into account the microstructural interactions between the composite components, the use of the multifield theory allow us to include the microstructure of the fiber and the interfacial transition zone.

One of the purpose of th e following sections is to furnish the model of the HPFRC composite with an adequate constitute law; it may be able to approximate the physical behavior of the real material. Another aim of the chapter is to present the model of each component, as well as the computational issues involved.

Once the deformation tensor has been determined at each point of the composite, the next step, in the mathematical description of the composite as a micromorphic material, is to select an appropriate set of independent scalar and tensorial fields to determine uniquely the stress field. Following the thermodynamic analysis and according with the hypothesis of the Subsection 2.3.3, the composite free energy is derived from the mixture theory hypothesis. Instead of characterizing the whole composite performance, the mixture theory centers its efforts in modeling each compound and how the results obtained from the constituents can be used to predict the composite response. The classical mixture theory has been modified since its apparition in 1960 (Trusdell & Toupin 1960a), in order to include the constitutive non-linearities presented in the compounds ((Oller et al. 1996) and (Car et al. 2002)).

2.5.1.   Matrix constitutive model

In controlled uniaxial tests, the macroscopic mechanical behavior of quasi-brittle materials like concrete shows a softening branch after reaching a maximum load (Hariri 2001). Consequently, the constitutive model that conveniently describes its behavior is usually the continuum damage one, in which homogenized material parameters at the macroscale are used.

The damage theory was presented by Kachanov in 1958, and further elaborated upon Kachanov, Lemaître and Chaboche (1985). The key point in the isotropic model is to find the value of the damage scalar variable, d_m, at any time of the deformation process. In this theory, the damage was defined as the degradation of the elastic properties, caused by the area reduction that transfers the internal forces. This is produced by the appearance and subsequent growth of microcavities and coalescence of microcracks (Maugin 1992). In the context of continuum mechanics, these phenomena can be taken into account by introducing an internal variable; this characterizes the degradation level of the material and transforms the real stress tensor into an effective stress tensor (Simo & Ju 1987)

$$\bar{\boldsymbol{\sigma}} = \mathbb{M}^{-1} : \boldsymbol{\sigma} \text{,} \qquad (2.21)$$

where, $\mathbb{M}$ is the fourth order tensor for the anisotropic damage model. In the case of the isotropic damage model, the degradation process is assumed uniformly distributed in all directions. Therefore, the damage is represented by a scalar variable d , so that, the tensor $\mathbb{M}$ is substituted by $\mathbb{M} = (1 - d_m)\mathbb{I}$ and the stress tensor takes the following form,

$$\bar{\boldsymbol{\sigma}} = \frac{\boldsymbol{\sigma}}{(1 - d_m)} \qquad (2.22)$$

where $\boldsymbol{\sigma}$ is the Cauchy stress tensor and $\bar{\boldsymbol{\sigma}}$ is the effective stress tensor, measured in the non-damage space. The damage variable gives a quantitative measure of the stiffness loss and takes values in the scale of 0 to 1, indicating the limits, no degraded and completely degraded material, respectively. The effective stress was defined by Lemaître-Chaboche, in 1978 and it is referred to the surface that really transmits the internal forces (Maugin 1992), see Figure 2.7.
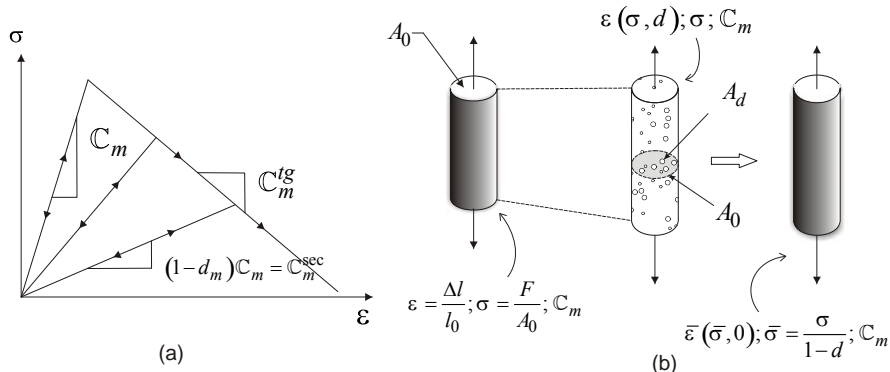
Figure 2.7 . Element under tension. Shape of the constitutive equation.

The matrix constitutive behavior is represented by means of a non-symmetric tensile/compressive strength isotropic damage model, which was originally developed by Simo and Ju (Simo & Ju 1987), and further elaborated by Oliver et al (Oliver et al. 1990).

2.5.2.   Tensile/compressive damage model

Once a free energy function was specified (Helmholtz energy, see equation (2.23)), Simo and Ju (Simo & Ju 1987) had obtained the basic ingredients of the model. Then, the constitutive equation for the stress tensor was derived along with the evolution laws, damage criterion and loading/unloading conditions. The density of Heltmholz's free energy of the matrix ψ_m is given by,

$$\psi_m\left(\boldsymbol{\varepsilon}_m,\alpha_m\right)=\left(1-d_m\left(\alpha_m\right)\right)\psi_0\left(\boldsymbol{\varepsilon}_m\right)$$

$$with \ \ d_m\left(\alpha_m\right)=1-\frac{q_m\left(\alpha_m\right)}{\alpha_m} \ \ and \ \ \psi_0\left(\boldsymbol{\varepsilon}\right)=\frac{1}{2}\boldsymbol{\varepsilon}_m:\mathbb{C}_m:\boldsymbol{\varepsilon}_m \tag{2.23}$$

where $\boldsymbol{\varepsilon}_m\left(\mathbf{x},t\right)$ is the strain tensor, α_m and q_m stand for the strain-like and stress-like internal variables, respectively. The ψ_0 term, in this model, is the elastic energy for the (undamaged) material. $\mathbb{C}_m$ is the Hooke's elastic constitutive tensor, whose expression is,

$$\mathbb{C}_m=\bar{\lambda}\left(\mathbf{1}\otimes\mathbf{1}\right)+2\bar{\mu}\mathbb{I} \tag{2.24}$$

where $\bar{\lambda}$ and $\bar{\mu}$ are the lame's parameters, $\mathbf{1}$ and $\mathbb{I}$ are the identity second and four order tensor, respectively. The $d_m \in \left[0,1\right]$, is the conventional continuum isotropic damage variable describing the elastic degradation: $d_m = 0$ represents the virgin material and $d_m = 1$ the completely degraded material.

Constitutive equation:	$\boldsymbol{\sigma}_m=\dfrac{\partial\psi_m}{\partial\boldsymbol{\varepsilon}_m}=\dfrac{q_m}{\alpha_m}\mathbb{C}_m:\boldsymbol{\varepsilon}_m$	(2.25)
Flow rule:	$\dot{\alpha}_m=\lambda_m,\ \ \alpha_m\geq\alpha_{m0}$	(2.26)
Softening law:	$\dot{q}_m=H_m\left(\alpha_m\right)\dot{\alpha}_m,\ \ 0\leq q_m\leq\alpha_{m0},\ \ q_{m0}=\alpha_{m0}$	(2.27)
Damage criterion:	$f_m\left(\boldsymbol{\varepsilon}_m,\alpha_m\right)=\eta_\varepsilon-\alpha_m\leq 0$	(2.28)
Complementary conditions and consistency condition:	$f_m\leq 0;\ \lambda_m\geq 0;\ \lambda_m f_m=0$ $\lambda_m\dot{f}_m=0\left(f_m=0\right)$	(2.29)

Box 2.1. Tension/compressive isotropic damage model.

The evolution equation for d_m is presented in equation (2.23)-b as the ratio of two thermodynamically conjugate internal variables of the model, i.e. α_m and q_m. The formulation presented in this work uses the damage model, which is summarized in Box 2.1

Equation (2.25) is the strain-stress relationship and equations (2.26) and (2.27) are the evolution laws of the strain-like and stress-like internal variables, respectively. The stress-like variable q_m in equation (2.27) evolves according to the softening law, which is ruled by the softening/hardening parameter H_m. The damage criterion in (2.28) is expressed in terms of the matrix effective stress field, which corresponds to,

$$\bar{\boldsymbol{\sigma}}_m = \mathbb{C}_m : \boldsymbol{\varepsilon}_m \tag{2.30}$$

The damage function in (2.28) is expressed in terms of the strain norm, or the so-called *equivalent strain*, η_ε, for the tensile/compressive damage model, which is used to compare different states of deformation,

$$\eta_\varepsilon = \theta\sqrt{\bar{\boldsymbol{\sigma}}_m : \left(\mathbb{C}_m\right)^{-1} : \bar{\boldsymbol{\sigma}}_m}, \; with \; \theta = \frac{\sum_{i=1}^3 \left\langle \bar{\boldsymbol{\sigma}}_i^m \right\rangle}{\sum_{i=1}^3 \left|\boldsymbol{\sigma}_i^m\right|}\left(1-\frac{1}{n_\sigma}\right)+\frac{1}{n_\sigma} \tag{2.31}$$

where $\langle \bullet \rangle$, denotes the Mac-Auley bracket, $n_\sigma = \sigma_m^{uc}/\sigma_m^{ut}$ is the ratio between the compressive, σ_m^{uc}, and tensile, σ_m^{ut}, ultimate strengths. The expression (2.31) also uses the effective stress tensor, in principal direction, $\bar{\boldsymbol{\sigma}}_i^m$, $i = 1, 2, 3$.

Damage occurs whether the strain norm exceeds the current value of the threshold (material strength), given by the following condition

$$\alpha_m = \max_{s \in [0,t]}\left\{\alpha_{m0}, \eta_\varepsilon\left(\boldsymbol{\varepsilon}_m\left(s\right)\right)\right\}, \; with \; \alpha_m\big|_{t=0} = \alpha_{m0} = \frac{\sigma_m^{ut}}{\sqrt{E_m}} \tag{2.32}$$

This equation identifies the strain-like internal variable evolution. In equation (2.32), E_m is the Young' modulus of the matrix material.

Rate form of the constitutive equation:

$$\dot{\boldsymbol{\sigma}}_m = \frac{q_m}{\alpha_m}\mathbb{C}_m : \dot{\boldsymbol{\varepsilon}}_m + \frac{H_m\alpha_m - q_m}{\left(\alpha_m\right)^2}\dot{\alpha}_m\bar{\boldsymbol{\sigma}}_m \tag{2.33}$$

Constitutive equation – Unloading case:

$$\mathbb{C}_m^{tg} = \frac{q_m}{\alpha_m}\mathbb{C}_m \tag{2.34}$$

Constitutive equation – loading case:

$$\mathbb{C}_m^{tg} = \left\{\frac{q_m}{\alpha_m}\mathbb{C}_m - \frac{H_m\alpha_m - q_m}{\left(\alpha_m\right)^3}\left(\frac{\left(\alpha_m\right)^2}{\theta}\left(\bar{\boldsymbol{\sigma}}_m \otimes \left(\mathbb{C}_m : \partial_{\bar{\sigma}}\alpha\right)+\theta^2\left(\bar{\boldsymbol{\sigma}}_m \otimes \bar{\boldsymbol{\sigma}}_m\right)\right)\right)\right\} \tag{2.35}$$

Box 2.2. Tensile/compressive isotropic tangent matrix of the constitutive operators.

Time differentiation of the equation (2.25) allows us to find the constitutive tangent tensor, both loading and unloading cases. The constitutive equation in elastic regime (also un-

loading case) is obtained, setting $\dot{\alpha}_m = 0$ and for loading case $\dot{\alpha}_m > 0$. The characterization of the loading/unloading conditions is provided in Box 2.2. The tangent operator in unloading and loading cases correspond to equations (2.34) and (2.35) respectively. More additional details are provided in (Linero 2006), where the expression of $\partial_{\bar{\sigma}}\alpha$ has been derived.

2.5.3. Fiber and debonding constitutive model

Typically, a uniaxial tensile test is chosen to estimate the parameters, which characterize the steel fibers response curve (Figure 2.8(a)), that are frequently used as reinforcement of HPFRC composites. The most important phenomenological properties in the uniaxial response of steel fibers can be identified as follows (De Souza Neto et al. 2008): **i.** The existence of an elastic domain, i.e., a range of stresses within the behavior of the material can be considered as purely elastic and without permanent (plastic) strains. **ii.** A yield stress and plastic yielding (or plastic flow). And, **iii.** The evolution of the plastic strain and evolution of the yield stress itself; this phenomenon is known as hardening. The aforementioned characteristics allow us to formulate a simple mathematical model containing all these essential features.
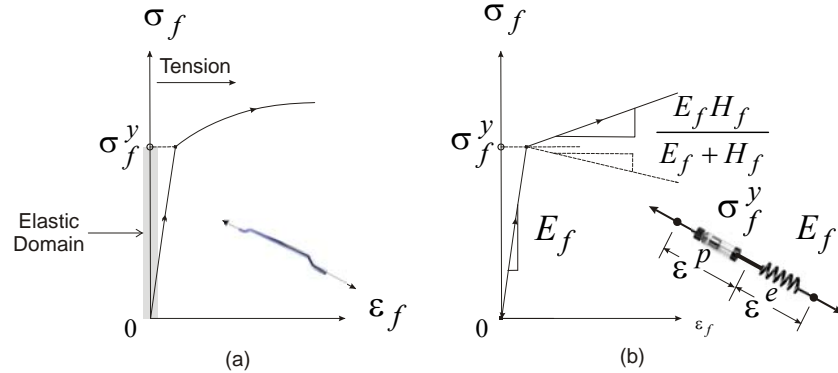
Figure 2.8. Unidimensional fiber plasticity model.

2.5.4. Plastic behavior in uniaxial tension

In the one dimensional plastic model, the uniaxial stress, corresponding to the total strain, ε_f, additively splits into an elastic part ε_f^e, assigned to the spring with constant E_f (Young modulus of the fiber), and a plastic strain part ε_f^p, on the friction device (Simo & Hughes 1998), that is

$$\varepsilon_f = \varepsilon_f^e + \varepsilon_f^p .$$
(2.36)

Equation (2.36) is the main hypotheses underlying in the small strain theory of plasticity. The total strain, ε_f, is the sum of an elastic, ε_f^e and a plastic, as follows:

$$\sigma_f = E_f \left(\varepsilon_f - \varepsilon_f^p \right) \qquad (2.37)$$

The additional ingredients of the constitutive relation connecting the uniaxial fiber stress: $\sigma_f = \boldsymbol{\sigma}_f : (\mathbf{r} \otimes \mathbf{r})$ with the uniaxial fiber strain: $\varepsilon_f = \boldsymbol{\varepsilon}_f : (\mathbf{r} \otimes \mathbf{r}) = (\overline{u}_r)_{,r} + \beta_{,r}$, where $\boldsymbol{\varepsilon}_f$ is defined in equation (2.14) are here presented. To connect both magnitudes, it is proposed a uniaxial standard elasto-plastic stress-strain model as it is presented in Box 2.3.

Free energy	$\psi_f \left(\boldsymbol{\varepsilon}_f \left(\nabla^s \overline{\mathbf{u}}, \nabla \boldsymbol{\beta} \right), \boldsymbol{\alpha}_f \right) = \frac{1}{2} E_f \left(\varepsilon_f - \varepsilon_f^p \right)^2 + \psi_f^h(\alpha_f); \qquad (2.38)$
Elastic stress-strain relationship:	$\sigma_f = E_f \left(\varepsilon_f - \varepsilon_f^p \right) \qquad (2.39)$
Plastic flow rule:	$\dot{\varepsilon}_f^p = \lambda_f sign \left(\sigma_f \right) \qquad (2.40)$
Internal variable evolution:	$\dot{\alpha}_f = \lambda_f \qquad (2.41)$
Yield condition:	$f_f \left(\sigma_f, \alpha_f \right) = \left| \sigma_f \right| - \left(q_f + \sigma_f^y \right) \qquad (2.42)$
Hardening law:	$\dot{q}_f = H_f \left(\alpha_f \right) \dot{\alpha}_f \qquad (2.43)$
Kuhn-Tucker complementary conditions and consistency condition:	$f_f \leq 0; \, \lambda_f \geq 0; \, \lambda_f f_f = 0 \quad \lambda_f \dot{f}_f = 0 \left(f_f = 0 \right) \qquad (2.44)$

Box 2.3. One dimensional rate independent plasticity model for the fiber tensile behavior with isotropic hardening.

In Box 2.3, we have introduced the yield function,

$$f_f \left(\sigma_f, \alpha_f \right) = \left| \sigma_f \right| - \left(q_f + \sigma_f^y \right). \qquad (2.45)$$

The yield criterion for this simple model reads,

$$\text{if } f_f \left(\sigma_f, \sigma_f^y \right) < 0 \Rightarrow \dot{\varepsilon}^p = 0,$$
$$\text{if } f_f \left(\sigma_f, \sigma_f^y \right) = 0 \Rightarrow \begin{cases} \dot{\varepsilon}^p = 0 \text{ for elastic unloading,} \\ \dot{\varepsilon}^p \neq 0 \text{ for plastic loading,} \end{cases} \qquad (2.46)$$

where $\dot{\varepsilon}^p$ is the plastic strain rate. The plastic flow rule for the uniaxial model corresponds to

$$\dot{\varepsilon}_f^p = \lambda_f sign \left(\sigma_f \right), \qquad (2.47)$$

where $sign(\bullet)$ stands for the sign function and $\dot{\lambda}^f$ for the plastic multiplier. Finally, the hardening law is defined as,

$$\dot{q}_f = H_f\left(\alpha_f\right)\dot{\alpha}_f. \tag{2.48}$$

Equation (2.48) completes the characterization of the uniaxial model.

The model is summarized in Box 2.3, in which Equation (2.41) represents the internal variable evolution and the Equation (2.43) stands for the hardening law. The hardening/softening evolution is characterized by the hardening/softening modulus, H_f, and the strain-like variable α_f, is the conjugate of the stress-like variable q_f.

The rate form of the elastic relationship (2.39) along with the Kuhn-Tucker complementary conditions and consistency condition in (2.44), yields the elastoplastic tangent modulus: $\left(\mathbb{C}_f^{tg}\right) = \partial\boldsymbol{\sigma}_f \, / \, \partial\boldsymbol{\varepsilon}_f$, which is given by:

$$\left(\mathbb{C}_f^{tg}\right) = E_f\left(\mathbf{r} \otimes \mathbf{r}\right) \otimes \left(\mathbf{r} \otimes \mathbf{r}\right);$$
$$\left(\mathbb{C}_f^{tg}\right) = \frac{E_f H_f}{E_f + H_f}\left(\mathbf{r} \otimes \mathbf{r}\right) \otimes \left(\mathbf{r} \otimes \mathbf{r}\right). \tag{2.49}$$

2.5.5.   Shear stress vs. slip relationship of the fiber matrix bond

In this section is introduced an expression for shear stress-slip relationship of the fiber-matrix bond in order to represent its mechanical behavior. Some researchers argue that the shear stress-slip relationship is of local nature. That is, this relationship is not unique but also depends on the location (Nammur 1989). Nevertheless, it is currently assumed that it is a material property, and hence, location independent. In the framework of the present model is assumed that the shear stress-slip relationship is a property of the material.

The shear stress-slip relationship, for a rebar in a concrete matrix, has been experimentally derived in association with pullout experimental results. In consequence, the primal problem is to predict a complete pullout load versus slip curve from an assumed bond stress versus slip relationship and, a dual problem, i.e., the bond stress versus slip is obtained from an experimental pullout curve (Naaman A. E & Alwan J.A 1993). Detailed analytical studies on bond, in fiber-reinforced cement composites, includes (Naaman et al. 1991), (Shannag et al. 1999), (Fantilli & Vallini 2007) and (Li & Stang 1997).

Recent contributions to the optimization of the geometrical properties of the fiber have been addressed by (Naaman 2003). These studies concluded that an increase of the lateral fiber surface area, for the same cross-section area, increases the frictional and adhesive bond resistance along the fiber length; in turn, the larger the lateral surface, the higher the pullout resistance is, and, therefore, the efficiency of the fiber.

According to Naaman (Naaman 2003) the fiber maximum pullout load $P_{\max}$, in cement matrices, can be written as in equation (2.50),:

$$P_{\max} = \begin{cases} \Pi d_f \tau_\Gamma L_e & \textit{Circular fiber} \\ \Psi \tau_\Gamma L_e & \textit{any cross} - \sec\textit{tional shape} \end{cases} \tag{2.50}$$

where Π is the perimeter of the circular fiber and d^f is the diameter, Ψ is the perimeter in a fiber with any other cross-sectional shape, L_e the embedded length of the fiber and τ_Γ is the average bond strength. Extensive tests have been carried out to correlate this pullout load and the bond stress, from which typical bond stress-slip relationship have been obtained, depending on the fiber geometrical and mechanical properties. In Figure 2.9 (a) and (b), the general relationship between the local bond stress and slip, for two types of rebars, is illustrated. In the case of smooth fiber, Fantilli and Vallini (Fantilli & Vallini 2007) provided expression for a model with exponential decay, after the maximum bond stress; some values of parameters are suggested taking into account the properties of the concrete matrix. Although, the matrix-fiber interface is generally, weak, inviscid and non-plastic, the properties of the interfacial zone are assumed, characterized by a plastic bond stress versus slip response. Therefore, a simple 1D plasticity model can be assumed to model the bond stress-slip relationship, in the interfacial transition zone.

Fiber type	Bond shear stress versus slip
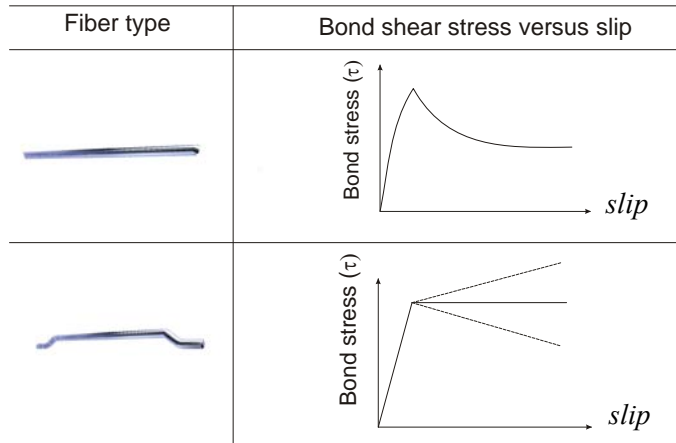
Figure 2.9. Bond shear stress versus slip relationship. (a) Smooth fiber, (b) Hook end fiber.

It is noted that the interfacial bond properties depend on many factors such as, strength on the matrix, fineness of the sand, and types of additives. As far as the value of the maximum bond stress, it is assumed to represent an average value. For the hooked end and other deformed fibers, an *equivalent bond strength or average value* can be determined by means of pullout tests. These values for smooth, hooked end and twisted fiber are given in (Kim et al. 2009).

Given the main features of the interfacial zone, the 1D plasticity model that represents the debonding process, basically contains the same ingredients of the plastic model used for the mechanical action of the fiber. The model in Box 2.4 basically consist of a linear-elastic response between the elastic component of the slip β defined as: $\beta^e = \beta - \beta^p$ and the average bond strength τ_{rs}, applied on the fiber matrix interface surface, where β is the total slip, β^p is the plastic component. β^e and τ_{rs} are related with an elastic modulus: G_Γ; and; up to reach the point where the stress is: τ_Γ, which marks, for the virgin material, the onset of the plastic process. After crossing this point, the bond-slip response follows a plastic har-

dening/softening rule. Thus, the evolution of the plastic component: β^p is given by the flow law (2.54) where λ_Γ represents the plastic multiplier. The hardening/softening rule is defined by the expressions (2.55) and (2.57), where the term: H_Γ represents the instantaneous hardening/softening modulus. The plasticity criterion is given by equation: $f_\Gamma = 0$, with f_Γ defined in (2.56). And the loading-unloading conditions by (2.58).

The rate form of the elastic relationship (2.53) along with the complementary conditions in (2.58) yields the elastoplastic tangent modulus: $\left(\mathbb{G}_\Gamma^{tg} \right) = \partial \tau_\Gamma / \partial \beta$, which is given by:

$$\mathbb{G}_\Gamma^{tg} = G_\Gamma (\mathbf{r} \otimes \mathbf{r});$$

$$\mathbb{G}_\Gamma^{tg} = \frac{G_\Gamma}{G_\Gamma + H_\Gamma} (\mathbf{r} \otimes \mathbf{r});$$

(2.51)

Specific free energy:	$\overline{\psi}_\Gamma(\beta^e, \alpha_\Gamma) = \dfrac{1}{2} \beta^e \cdot G_\Gamma \cdot \beta^e + \overline{\psi}_\Gamma^h(\alpha_\Gamma);$	(2.52)
Elastic stress-strain relationship:	$\tau_{rs} = G_\Gamma \left(\beta - \beta^p \right)$	(2.53)
Flow rule:	$\dot{\beta}^p = \lambda_\Gamma \, sign\left(\tau_{rs} \right)$	(2.54)
Isotropic hardening law:	$\dot{\alpha}_\Gamma = \lambda_\Gamma$	(2.55)
Yield condition:	$f_\Gamma \left(\tau_{rs}, \alpha_\Gamma \right) = \left| \tau_{rs} \right| - \left(q_\Gamma + \tau_\Gamma^u \right)$	(2.56)
Isotropic hardening law:	$\dot{q}_\Gamma = H_\Gamma \left(\alpha_\Gamma \right) \dot{\alpha}_\Gamma$	(2.57)
Complementary conditions:	$f_\Gamma \leq 0; \ \lambda_\Gamma \geq 0; \ \lambda_\Gamma f_\Gamma = 0$ $\lambda_\Gamma \dot{f}_\Gamma = 0 \quad \left(if \quad f_\Gamma = 0 \right)$	(2.58)

Box 2.4. One dimensional rate independent plasticity for the interface zone (IZ)

2.5.6.   Homogenized composite free energy according with the rule of mixtures with a unique bundle of fibers

In the multifield theory, the composite uses the same concepts of the standard continuum mechanics, but the presence of the fiber forces us to homogenize the stress field. Using the classical Taylor or homogeneous microscopic strain model, commonly known as the rule of mixtures, and assuming isothermal case, we can define the Helmotz free energy of the composite, as the addition of the free energies of all components, weighted by their volumetric participation factor. Let us first consider a unique fiber bundle oriented in the direction $\mathbf{r}$. In the next subsection we generalize the model including multiples fiber bundles oriented in

several directions. We denote k_f the volume fraction of the fiber and k_m the volume fraction of the cement, such that: $k_f + k_m = 1$.

The free energy of the composite is defined as follows:

$$\psi(\nabla^s \bar{\mathbf{u}}, \boldsymbol{\beta}, \nabla\boldsymbol{\beta}, \boldsymbol{\alpha}) = k_m \psi_m \left(\boldsymbol{\varepsilon}_m \left(\nabla^s \bar{\mathbf{u}} \right), \boldsymbol{\alpha}_m \right) + k_f \psi_f \left(\boldsymbol{\varepsilon}_f \left(\nabla^s \bar{\mathbf{u}}, \nabla\boldsymbol{\beta} \right), \boldsymbol{\alpha}_f \right) + k_f \delta\bar{\psi}_\Gamma(\boldsymbol{\beta}, \boldsymbol{\alpha}_\Gamma); \quad (2.59)$$

where ψ_m, ψ_f and $\bar{\psi}_\Gamma$ are the matrix, fiber and ITZ free energies assigned to each component and defined in previous sections. Note that each of these three components has their own set of internal variables, $\boldsymbol{\alpha}_m$, $\boldsymbol{\alpha}_f$ and $\boldsymbol{\alpha}_\Gamma$.

2.6.   Extension to HPFRC Composites having a random distribution of fiber directions

Composites with randomly distributed fibers are often both heterogeneous and anisotropic, thereby, their mechanical properties vary from point to point inside the material. The coupling effect in such materials, between deformation modes and loading conditions, causes difficulties in simulation, modeling and analysis, which are not easily to overcome. Considering the HPFRC composite response, two problems arise; first, how to include the constitutive behavior of each fiber, interfacial zone and the matrix in the material response and, second, how to detect the instant, in which localizes the response of the composite material. In fact, some compounds could fail, but the whole material could exhibit a non-localized response.

In previous sections, the stress-strain relationships of each compound were defined, however, in order to combine such models is invoked a homogenization methodology. One way is to resort a multiscale solid constitutive model. Within a general kinematical variational formulation De Souza et al (De Souza Neto et al. 2008), presented four classes of these models. We follow the hypothesis of homogeneous strain over the generally heterogeneous microstructure. This assumption is referred in De Souza's work as the Taylor model or homogeneous micro-cell strain model. This model is also referred, in the literature, to as the so-called *rule of mixtures*.

2.6.1.   Rule of mixtures theory

The classical rule of mixtures has been modified in order to include the existing constitutive non linearities, presented in the constituents ((Oller et al. 1996), (Car et al. 2002)). These modifications were made in the light of the themodynamical description of the compounds and provided a constitutive equation manager, as described by Martínez (Martínez 2008). The results obtained from the constituents can thus be used to predict the composite constitutive response. This idea is crucial in developing constitutive models by linear combination of the volume fractions and individual material properties.

According to (de Souza Neto & Feijóo 2010), one important limitation of the Taylor approximation is the fact that it does not consider mechanical interaction among the solid phas-

es. Moreover, the constitutive material model requires the connection between the strain of the compounds and the total strain, and also, between the stresses.

In the Taylor model, the following assumptions are considered:
1. All the components undergo the same strains,
2. Each component contribution, to the global behavior of the composite, is proportional to its volumetric participation.

From the second assumption, the *homogenized stress* is obtained using the stress of the compounds,

$$\boldsymbol{\sigma} = k_m \boldsymbol{\sigma}_m + k_f \boldsymbol{\sigma}_f \tag{2.60}$$

The recomposition of total stress tensor uses the volumetric participation, which is defined by the relation between the volume occupied by each component, V_c, and the total volume of the composite, V :

$$k_c = \frac{V_c}{V} \tag{2.61}$$

The mechanical model of a HPRFC having a fiber bundle in one direction, presented in section 2.5, can be generalized to account for a statistical distribution of fibers. In this case, n_f discrete directions are selected in the plane of analysis forming angles (with respect to the horizontal direction) that are regularly distributed in the interval $\left[0, \pi\right]$, These n_f fiber bundles with identical volume fractions represent a random fiber distribution. Then, as a generalization of the model, we extend it to consider n_f fiber bundles arbitrarily oriented.

Let us consider n_f fiber bundles. The i-th bundle, characterized with the super-index I ($I = 1, ..., n_f$), has assigned one volume fraction k_f^I, one direction vector $\mathbf{r}^I$ and one micromorphic field $\boldsymbol{\beta}^I = \beta^I(r, s)\mathbf{r}^I$ (no summation on the index I). Inclusion of new micromorphic fields implies that new associated microstresses $\mathbf{S}^I$ and microforces $\mathbf{z}^I$ arise for every considered index I. Also, it is required the fulfillment of additional balance equations (2.5)-b, for every index I.

Using the mixture theory, the free energy of the HPFRC is the linear combination of free energies of all the components weighted by their corresponding fraction volume. Then, the stress equation (2.60), in a composite with nf fiber bundles, results:

$$\boldsymbol{\sigma} = k_m \boldsymbol{\sigma}_m \left(\boldsymbol{\varepsilon}_m; \alpha_m \right) + \sum_{i=1}^{n_f} k_f^I \boldsymbol{\sigma}_f^I \left(\boldsymbol{\varepsilon}_f^I(\overline{\mathbf{u}}, \boldsymbol{\beta}^I); \alpha_f^I \right) \tag{2.62}$$

Figure 2.10 shows a schematic decomposition of the stresses at any point of the HPFRC composite. The total stress tensor in global axis is the transformation of the scalar contribution of the microstructural axial stress, σ_f^I,

$$\boldsymbol{\sigma}_f^I = E_f \left(\left(\overline{u}_r \right)_{,r} + \beta_{,r}^I \right)^e \left(\mathbf{r}^I \otimes \mathbf{r}^I \right) \tag{2.63}$$

where $\boldsymbol{\sigma}_f^I$ corresponds to the *I-th* fiber stress, which expression is given by the last term in (2.63) along the direction $\mathbf{r}^I$.

we denote:

$$\boldsymbol{\sigma} = \hat{\boldsymbol{\sigma}}\left(\mathbf{u}, \boldsymbol{\beta}, \nabla\boldsymbol{\beta}, \boldsymbol{\alpha}\right), \qquad (2.64)$$

the expression representing the complete set of the composite model constitutive equations. In this context, it is understood that the notation $\boldsymbol{\beta}$ and $\nabla\boldsymbol{\beta}$ stand for the complete set of micromorphic fields, with indices: $I = 1, ..., nf$.
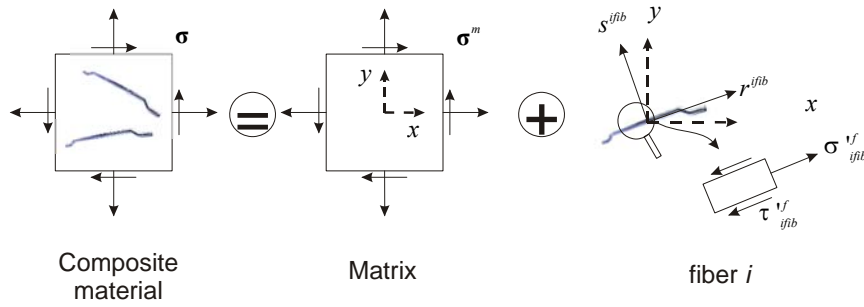
Figure 2.10 . Decomposition of the stresses in a material point of the HPFRC composite

2.6.2.   Tangent constitutive operator

In a nonlinear analysis, the tangent stiffness tensor provides the relation between an increment of stresses and an increment of strains, in the same way that it does the stiffness matrix in a linear analysis (Martínez 2008). In the Taylor model, the homogenized tangent operator is defined as the volume average of the microscopic constitutive tangent operators. To determine the constitutive relation, it is necessary to obtain the complete form of the homogenized stress tensor. We accomplish this, substituting the expression (2.63) in equation (2.60). Furthermore, the stress rate term equation can then be written as follows,

$$\dot{\boldsymbol{\sigma}} = k_m \dot{\boldsymbol{\sigma}}_m + \sum_{ifib=1}^{nfib} k_f^I \dot{\boldsymbol{\sigma}}_f^I. \qquad (2.65)$$

The strain rate and the stress rate tensors are related by the constitutive model, discussed previously, which are $\mathbb{C}_m^{tg} = \partial\boldsymbol{\sigma}_m/\partial\boldsymbol{\varepsilon}_m$, $\mathbb{E}_f^{tg} = \partial\boldsymbol{\sigma}_f/\partial\boldsymbol{\varepsilon}_f$ and $\mathbb{G}_f^{tg} = \partial\tau_\Gamma/\partial\beta$ for the matrix, fiber and the ITZ respectively.

Box 2.5 summarizes the constitutive relations between the stresses and strains in rate form. Under the compatibility of the strains between the components, the tangent constitutive equation of the composite can be written as:

$$\dot{\boldsymbol{\sigma}} = \mathbb{C}^{tg} : \dot{\boldsymbol{\varepsilon}}, \qquad (2.66)$$

where the tangent constitutive tensor $\mathbb{C}^{tg}$ is evaluated substituting the set of equations in Box 2.5 into equation (2.66), yielding,

$$\mathbb{C}^{tg} = k_m \mathbb{C}_m^{tg} + \sum_{i=1}^{n_f} k_f^I E_f^{tg^{(I)}} \left(\left(\mathbf{r}^I \otimes \mathbf{r}^I \right) \otimes \left(\mathbf{r}^I \otimes \mathbf{r}^I \right) \right) \qquad (2.67)$$

stress-strain rate relationship for matrix: $\dot{\boldsymbol{\sigma}}_m = \mathbb{C}_m^{tg} : \dot{\boldsymbol{\varepsilon}}_m$	(2.68)
stress-strain rate relationship for axial mechanical fiber action: $\dot{\boldsymbol{\sigma}}_f^I = \mathbb{E}_f^{tg} \dot{\boldsymbol{\varepsilon}}_f^I$	(2.69)
stress-strain rate relationship for debonding fiber action: $\dot{\tau}_\Gamma = \mathbb{G}_\Gamma^{tg} \dot{\beta}_\Gamma$	(2.70)

Box 2.5. One dimensional rate independent plasticity for the fiber tensile behavior with isotropic hardening

2.7.   Summary of the balance equations

The balance equations (2.5)-a, (2.20) jointly with the constitutive equations (2.64) and the conventional boundary terms in tractions: $\dot{\boldsymbol{\sigma}} \cdot \mathbf{n} = \dot{\mathbf{t}}^*$, defined in Γ_σ, or displacements: $\dot{\mathbf{u}} = \dot{\mathbf{u}}^*$, defined in Γ_u, jointly with the prescription $\boldsymbol{\beta} = \mathbf{0}$ in the Γ boundary (with $\Gamma_\beta = \Gamma = \Gamma_\sigma \cup \Gamma_u$), define the boundary value problem in strong form. These equations, that are written in terms of the macro-displacements $\mathbf{u}$ and the microslip $\boldsymbol{\beta}$, are summarized in Box 2.6.

It is remarked that the coupling between both macro- und mesostructure, is done via the morphological descriptor (or slip in the interfacial transition zone). The solution of the equation set provides the displacements $\dot{\mathbf{u}}$ and the slip $\dot{\boldsymbol{\beta}}$ in the whole domain. It is worth mentioning that a periodic structure is not required by the solution scheme.

In summary, following the framework of continuum with microstructure and the principles of thermodynamics, it was possible to link two objects of distinct nature, which are interacting and operate at different scales. The resulting set of partial differential equations models the composite material in terms of the macro- and microfields and the interaction between them by means of the morphological descriptor field defined at the interface. The model makes possible to represent the two different scales, without resorting to a complex formulation.

In general, in the macro-constitutive models, the balance equation for the mesostructure and the morphological descriptor associated to the matrix-fiber slip phenomena do not appear in a natural manner unlike in the continuum with microstructure theory. Additionally, in the model developed by means of the multifield theory arises the interaction force (i.e. the micromorfic force) at substructural level that accounts for direct action on the underlying substructure, and which is not accounted in a macrocostitutive approach.

Continuum with microstructure
Find: $\mathbf{u}, \beta$

Fulfilling:		
$\nabla \cdot \boldsymbol{\sigma} + \rho \mathbf{b} = \mathbf{0} \ \forall \mathbf{x} \in \Omega$	Macroscopic momentum balance equation	(2.71)
$\tau_f^i - \dfrac{A_f}{\Pi_f}(\sigma_f^i)_{,r} = 0, \quad \forall \mathbf{x} \in \mathcal{B}$ $(i = 1, ..., nf)$	Mesotructural momentum balance	(2.72)
$\boldsymbol{\sigma} \cdot \mathbf{n} = \mathbf{t}^* \quad \forall \mathbf{x} \in \Gamma_\sigma \ ;$	Natural boundary condition	(2.73)
$\mathbf{u} = \mathbf{u}^* \quad \forall \mathbf{x} \in \Gamma_u \ ;$	Essential boundary condition	(2.74)
$\boldsymbol{\beta}^i = 0 \quad (i = 1, ..., nf) \quad \forall \mathbf{x} \in \Gamma$		(2.75)
$\boldsymbol{\sigma} = \hat{\boldsymbol{\sigma}}(\mathbf{u}, \boldsymbol{\beta}, \nabla \boldsymbol{\beta}, \boldsymbol{\alpha}).$	Composite constitutive equation	(2.76)

Box 2.6. Boundary value problem definition for the HPFRC composite.

Finally, note that equations in Box 2.5 are not limited by the specific nature of the inter-facial transition zone and, therefore, it is expected that they can represent the mechanical behavior of the composites for interfacial transition zones with different properties. Thus, the model is general for abroad class of short fiber composites under some minor physical requirements.

Chapter 3
Variational approach and finite element formulations

3.1. Introduction

So far, we have dealt with the theoretical issues of HPFC composites as the governing equation of the behavior of the HPFRC composite including the micromechanics and the material constitutive relationships. In this chapter, we introduce a finite element formulation, as also its numerical implementation, to deal with this kind of theoretical model.

The finite element formulation of the HPFRC composite boundary value problem requires: 1) a finite element discretization that comprises a finite element approximation of the variational BVP presented in Chapter 2 and 2) a time discretization of the underlying constitutive initial value problem defined by the constitutive equations. After introducing both approximations, the original variational BVP is reduced to a set of (in general nonlinear) algebraic equations, which typically, can be solved by means of a Newton Raphson algorithm.

Explicit or implicit time integration algorithms can be selected for integration of the material model. Each integration scheme has advantages and disadvantages, which are summarized in (Oliver et al. 2008). However, the classical implicit (backward-Euler) integration scheme is usually chosen for nonlinear solid materials. An implicit/explicit integration scheme (IMPL-EX scheme) for nonlinear constitutive models was presented by (Oliver et al. 2008) which is here employed to perform the integration of the constitutive models. Details about these issues are provided along this chapter.

3.2.   Variational formulation

In order to derive the variational BVP for the HPFRC composite, the virtual variation of the configuration space is defined as follows:

$$V_0 = \left\{ \delta \mathbf{u} \;\; \middle| \;\; \delta \mathbf{u} = 0, \quad \forall \mathbf{x} \in \Gamma_u \right\};$$
$$V_0^\beta = \left\{ \delta \boldsymbol{\beta}^{(I)} = \delta \beta^{(I)} \mathbf{r}^{(I)} \;\; \middle| \;\; \delta \boldsymbol{\beta}^{(I)} = 0, \quad \forall \mathbf{x} \in \Gamma; \;\; \left(I = 1, \ldots, n_f \right) \right\}$$

(3.1)

where Γ stands for boundary surface of the body. Note that the variations of $\boldsymbol{\beta}$, one for every index I, are considered with a fixed direction. Then, the boundary value problem described in Box 2.6 is alternatively formulated using a variation approach:

$$\int_\mathfrak{B} \left(\nabla \cdot \boldsymbol{\sigma} + \mathbf{b} \right) \cdot \delta \mathbf{u} = \mathbf{0}, \quad \forall \delta \mathbf{u} \in V_0$$

(3.2)

and

$$\int_\mathfrak{B} \left(\tilde{\tau}_f^{(I)} - \frac{A_f}{\Pi_f} \left(\tilde{\sigma}_f^{(I)} \right)_{,r} \right) \cdot \delta \beta^{(I)} = \mathbf{0}, \quad \forall \delta \beta^{(I)} \in V_0^\beta; \;\; \left(I = 1, \ldots, n_f \right)$$

(3.3)

The microstructure variational equation (3.3) comes from admitting arbitrarily scalar variations, $\delta \beta^{(I)}$, which are associated with the r – component of $\beta^{(I)}$. Integrating (3.2) and (3.3) by parts, using the Green identity and including the boundary conditions (2.74) and (2.75), the variational BVP can be summarized as shown in Box 3.1

Continuum with microstructure Find: $\mathbf{u}(\mathbf{x}, t)$ and $\boldsymbol{\beta}(\mathbf{x}, t)$; $\forall \mathbf{x} \in \mathfrak{B}$, fulfilling,	
$\displaystyle \int_\mathfrak{B} \boldsymbol{\sigma} : \nabla^s \delta \mathbf{u} \, dV - \int_\mathfrak{B} \mathbf{b} \cdot \delta \mathbf{u} \, dV - \int_{\Gamma_\sigma} \mathbf{t}^* \cdot \delta \mathbf{u} \, dS = 0; \quad \forall \delta \mathbf{u} \in V_0$	Momentum balance equation
$\displaystyle \int_\mathfrak{B} \left(\tilde{\tau}_f^{(I)} \delta \beta^{(I)} - \frac{A^f}{\Pi^f} \tilde{\sigma}_f^{(I)} \left(\delta \beta^{(I)} \right)_{,r} \right) dV = 0; \quad \forall \delta \beta^{(I)} \in V_0^\beta; \;\; \left(I = 1, \ldots, n_f \right)$	Microstructure momentum balance equation

Box 3.1. Variational boundary value problem definition for the HPFRC composite.

3.3.   Finite element discretization of the variational formulation

A $\left(\mathbf{u} - \boldsymbol{\beta} \right)$ mixed finite element with equal order of interpolation is proposed here. Assuming a usual form to interpolate the displacement $\mathbf{u}(\mathbf{x}, t)$, and the microslip $\beta^{(I)}$ for $I = 1, \ldots, nf$, such that

$$\hat{\mathbf{u}}(\mathbf{x},t) = \sum_{j=1}^{j=n_{node}} \mathbf{N}_j(\mathbf{x})\mathbf{q}_j(t), \tag{3.4}$$

$$\hat{\beta}^i(\mathbf{x},t) = \sum_{j=1}^{j=n_{node}} N_j(\mathbf{x})p_j^I(t), \tag{3.5}$$

where n_{node} is the number of nodes of the finite element mesh, $\mathbf{N}_j(\mathbf{x})$ are the standard interpolation functions and $\mathbf{q}_j$ and p_j^I stand for the displacements and $i-th$ micro-slip of the node $j-th$, respectively. The corresponding discretization of the variational displacement fields $\delta\mathbf{q}$ and $\delta\mathbf{p}^I$ reads,

$$\delta\hat{\mathbf{u}}(\mathbf{x}) = \sum_{j=1}^{n_{node}} \mathbf{N}_j(\mathbf{x})\delta\mathbf{q}_j, \tag{3.6}$$

$$\delta\hat{\beta}(\mathbf{x}) = \sum_{j=1}^{n_{node}} N_j(\mathbf{x})\delta p_j^I, \tag{3.7}$$

where, $\delta\mathbf{q}_j$ and δp_j^i are the corresponding variations associated with the displacement and $i-th$ slip of the $j-th$ node, respectively.

3.3.1. Matrix notation

Using the Voigt notation, the discretized symmetric gradient in matrix form of the variations associated with the displacement and the $i-th$ slip can be written as,

$$\left\{\nabla^s \delta\mathbf{q}\right\}^e = \mathbf{B}^e \delta\mathbf{q}^e \text{ with}$$

$$\delta\mathbf{q}^e = \left[\delta\mathbf{q}_1^T, \quad \delta\mathbf{q}_2^T, \quad \ldots, \quad \delta\mathbf{q}_n^T\right]^T \quad and \quad \delta\mathbf{q}_j^T = \left[\delta q_x, \delta q_y\right]_j^T, \tag{3.8}$$

in equation (3.8), $\mathbf{B}^e$ is the strain-displacement matrix given by

$$\mathbf{B}^e = \left[\mathbf{B}_1^e, \quad \mathbf{B}_2^e, \quad \ldots, \quad \mathbf{B}_{nnode}^e\right] with$$

$$\mathbf{B}_j^e = \begin{bmatrix} \left(N_j^e\right)_{,x} & 0 \\ 0 & \left(N_j^e\right)_{,y} \\ \left(N_j^e\right)_{,y} & \left(N_j^e\right)_{,x} \end{bmatrix}. \tag{3.9}$$

The nodal shape functions of the variation associated with the $i-th$ slip are

$$\delta\beta^i = \left[\mathbf{N}\right]^e \left(\delta p^I\right)^e,$$

$$\left(\delta p^I\right)^e = \left[\delta p_1, \quad \delta p_2, \quad \ldots, \quad \delta p_n\right]^T, \tag{3.10}$$

where $\left[\mathbf{N}\right]^e$ are the nodal shape functions arranged as a vector. That is,

$$\left[\mathbf{N} \right]^e = \left[N_1, N_2, \dots, N_{mnode} \right].$$ (3.11)

The corresponding discretized gradient in matrix form can be written as,

$$\left(\delta \mathbf{p}^I \right)_{,r} = \left[\mathbf{N} \right]^e_{,r} \left(\delta p^I \right)^e$$ (3.12)

In equation (3.12), $\left[\mathbf{N} \right]^e_{,r}$ are the derivatives of the nodal shape function (respect to the $\mathbf{r}$ coordinate), arranged as a vector.

3.3.2.   Discrete form of the variation BVP

Being $\hat{\boldsymbol{\sigma}}$, the stress term provided by the constitutive model $\left(\hat{\boldsymbol{\sigma}}(\mathbf{p},\mathbf{q},\boldsymbol{\alpha}) \right)$, and similarly, $\left(\hat{\sigma}^I_f \right)$ and $\left(\hat{\tau}^I_f \right)$ the average fiber stress and the average bond shear stress in the interface zone and by substitution of the approximate solution (3.4) and (3.5) and the variational fields (3.6) and (3.7), into the variational BVP presented in Box 3.1, yields the discrete form that is initially written at element level.

$$\left(\mathbf{R}_u \right)^e = \int_{\Omega^e} \left(\mathbf{B}^e \right)^T \hat{\boldsymbol{\sigma}} d\Omega^e - \left(\mathbf{F}^{ext} \right)^e$$

$$\left(\mathbf{R}_\beta \right)^e = \int_{\Omega^e} \left(\left[\mathbf{N} \right]^e \hat{\tau}^{(I)}_f + \frac{A_f}{\Pi_f} \left[\mathbf{N} \right]^e_{,r} \hat{\sigma}^{(I)}_f \right) d\Omega^e \quad ; \quad \left(\forall I = 1,\dots,nf \right)$$ (3.13)

The implementation of the finite element method involves the assembling of the element contributions (3.13). Using the assemblage operator Λ and defining the global vector of external forces as $\mathbf{F}^{ext}$, the discrete form of the variational BVP is obtained. This is summarized in Box 3.2.

Continuum with microstructure	
Find: $\mathbf{q}(\mathbf{x},t)$ and $\mathbf{p}^I(\mathbf{x},t)$; $\left(\forall I = 1,\dots,nf \right)$, fulfilling,	
$$\mathbf{R}_u = \overset{nelem}{\underset{e=1}{\Lambda}} \int_{\Omega^{(e)}} \left(\mathbf{B}^e \right)^T \hat{\boldsymbol{\sigma}} d\Omega^e - \mathbf{F}^{ext}$$	Momentum balance equation
$$\mathbf{R}_\beta = \overset{nelem}{\underset{e=1}{\Lambda}} \int_{\Omega^e} \left(\left[\mathbf{N} \right]^e \hat{\tau}^i_f + \frac{A_f}{\Pi_f} \left[\mathbf{N} \right]^e_{,r} \hat{\sigma}^I_f \right) d\Omega^e \quad ; \quad \left(\forall I = 1,\dots,nf \right)$$	Microstructure momentum balance equation

Box 3.2. Discrete form of the variational boundary value problem definition for the HPFRC composite.

From Box 3.2, expressions for the internal forces are expressed as

$$\left(\mathbf{F}^{int} \right)^e = \int_{\Omega^e} \left(\mathbf{B}^e \right)^T \left(k_m \hat{\boldsymbol{\sigma}}_m + \sum_{I=1}^{nfib} k^I_f \hat{\boldsymbol{\sigma}}^I_f \right) d\Omega^e$$ (3.14)

where, it was substituted the total stress in terms of the matrix and fiber contributions. The second component of the internal forces is given by:

$$\left(\mathbf{f}^{\mathrm{int}}\right)^e = \int\limits_{\Omega^e}\left([\mathbf{N}]^e\,\hat{\tau}_f^{(I)} + \frac{A_f}{\Pi_f}[\mathbf{N}]^e_{,r}\,\hat{\sigma}_f^{(I)}\right)d\Omega^e \tag{3.15}$$

We define the global residual vector as:

$$\Re\left(\mathbf{q},\mathbf{p}^I\right) = \mathop{\Lambda}\limits_{e=1}^{nelem}\left\{\begin{array}{c}\left(\mathbf{F}^{\mathrm{int}}\right)^e - \left(\mathbf{F}^{\mathrm{ext}}\right)^e \\ \left(\mathbf{f}^{\mathrm{int}}\right)^e\end{array}\right\} = \mathbf{0}, \tag{3.16}$$

3.3.3.   Strains and microslips

The kinematical description obtained for the composite, in which the fiber-matrix displacement was included, is presented in equation (2.12). The matrix representation of the strain tensor in any point, using Voigt notation, is given by

$$\{\boldsymbol{\varepsilon}\}^e = \{\boldsymbol{\varepsilon}_m\} + \mathcal{H}_f\{\boldsymbol{\varepsilon}_f\} + \delta_\Gamma\{\boldsymbol{\gamma}\}, \tag{3.17}$$

where the vectors $\{\boldsymbol{\varepsilon}_m\}$, $\{\boldsymbol{\varepsilon}_f\}$, $\{\boldsymbol{\gamma}\}$ stand for matrix, fiber and fiber-matrix interface shear strains in the new notation, respectively. The discretized matrix strain vector related with the nodal displacement is given by

$$\{\boldsymbol{\varepsilon}_m\} = \mathbf{B}^e\mathbf{q}^e\ ,$$
$$\mathbf{q}^e = \left[\mathbf{q}_1^T,\quad \mathbf{q}_2^T,\quad \ldots,\quad \mathbf{q}_n^T\right]^T\quad and\quad \mathbf{q}_j^T = \left[q_x, q_y\right]_j^T, \tag{3.18}$$

where $\mathbf{B}^e$ is the strain-displacement matrix, in equation (3.9)-b, and $\mathbf{q}_j$ the displacement at $j-th$ node.

The fiber strain vector for the $ith-$ fiber bundle microstructure is decomposed as follows,

$$\{\boldsymbol{\varepsilon}_f^I\} = \{\boldsymbol{\varepsilon}_m\} + \{\beta_{,r}^I\} + \{\beta_{,s}^I\}, \tag{3.19}$$

where the $\{\boldsymbol{\varepsilon}_m\}$, $\{\beta_{,r}^I\}$ and $\{\beta_{,s}^I\}$ are the contributions from the matrix displacement and the slip-dependent components in the local direction $(\mathbf{r},\mathbf{s})$, respectively. Each of the components of the gradient of the slip corresponds to,

$$\{\beta_{,r}^I\} = \mathbf{T}_1[\mathbf{N}]^e_{,r}\left(p^I\right)^e \qquad , \qquad \mathbf{T}_1 = \left[r_x^2,\quad r_y^2,\quad r_x r_y\right]_I^T,$$
$$\{\beta_{,s}^I\} = \mathbf{T}_2[\mathbf{N}]^e_{,s}\left(p^I\right)^e \qquad , \qquad \mathbf{T}_2 = \left[r_x s_x,\quad r_x r_y,\quad 0.5\left(r_x r_y + r_y r_x\right)\right]_I^T, \tag{3.20}$$
$$\left(p^I\right)^e = \left[p_1,\quad p_2,\quad \ldots,\quad p_n\right]^T,$$

where $\mathbf{T}_1$ and $\mathbf{T}_2$ are the matrix representation of the products $\left(\mathbf{r}\otimes^s\mathbf{r}\right)$ and $\left(\mathbf{r}\otimes^s\mathbf{s}\right)$, respectively.

Finally, the strain vector for the $ith-$ fiber microstructure yields

$$\{\boldsymbol{\gamma}^I\} = \mathbf{T}_2 [\mathbf{N}]^e (p^I)^e ,\tag{3.21}$$

which contains the component of the interface slip of the microstructure.

The total uniaxial strain of the fiber $\varepsilon_f = \boldsymbol{\varepsilon}_f : (\mathbf{r} \otimes \mathbf{r})$ may be conveniently rewritten as,

$$\varepsilon_f = \mathbf{r} \cdot \boldsymbol{\varepsilon}_f \cdot \mathbf{r} ,$$

$$\varepsilon_f = \mathbf{T}_1^T \mathbf{B}^e \mathbf{q}^e + [\mathbf{N}]_{,r}^e (p^I)^e .\tag{3.22}$$

The equation (3.22)-b is obtained by replacing the value of $\boldsymbol{\varepsilon}_f$ from equation (2.14) and operating algebraically in (3.22)-a, then it is transformed to matrix notation. The strains and microstrains are summarized using matrix notation in Box 3.3.

Strains and microstrains	
$\{\boldsymbol{\varepsilon}_m\} = \mathbf{B}^e \mathbf{q}^e$	Matrix strain
$\{\boldsymbol{\varepsilon}_f^I\}^e = \mathbf{B}^e \mathbf{q}^e + \mathbf{T}_1 [\mathbf{N}]_{,r}^e (p^I)^e + \mathbf{T}_2 [\mathbf{N}]_{,s}^e (p^I)^e$	Fiber total strain $ith-$ fiber bundle
$\varepsilon_f^I = \mathbf{T}_1^T \mathbf{B}^e \mathbf{q}^e + [\mathbf{N}]_{,r}^e (p^I)^e \quad and \quad \beta^I = [\mathbf{N}]^e (p^I)^e$	Microstrains for $ith-$ fiber bundle
$\{\boldsymbol{\gamma}^I\} = \mathbf{T}_2 [\mathbf{N}]^e (p^I)^e$	Strain vector for the $ith-$ fiber bundle

Box 3.3. Boundary value problem definition for the HPFRC composite.

3.3.4.   The nonlinear incremental finite element equation

The equilibrium equation of the body under forces $\mathbf{b}, \mathbf{t}^*$ and $\mathbf{S} \cdot v$ at $t = t_n$, so that the stress fields $\boldsymbol{\sigma}_n$ and $(\tau_f^I)_n$, $(\sigma_f^I)_n$, imposes that:

$$\Re(\mathbf{q}_n, \mathbf{p}_n^I) = \mathbf{0}.\tag{3.23}$$

The proportional loading is characterized by body force and surface traction fields given, at an arbitrary instant t_{n+1} , by

$$\mathbf{b}_{n+1} = \lambda_{n+1} \overline{\mathbf{b}} ,$$

$$\mathbf{t}_{n+1} = \lambda_{n+1} \overline{\mathbf{t}} ,\tag{3.24}$$

where λ_{n+1} is the prescribed load factor at t_{n+1} and $\overline{\mathbf{b}}$ and $\overline{\mathbf{t}}$ are prescribed constant fields. The global external force vector corresponds to

$$\mathbf{F}_{n+1}^{ext} = \lambda_{n+1} \overline{\mathbf{F}}_{n+1}^{ext}.\tag{3.25}$$

After the standard finite element discretization presented in Box 3.2, the problem is reduced to find: the nodal displacements $\mathbf{q}_{n+1}$, the slip $\mathbf{p}_{n+1}^I$ in the $ith-$fiber, the updated internal variables of the damage model $d_{n+1}, \boldsymbol{\alpha}_{n+1}, \mathbf{q}_{n+1}$, the internal variables of the plastic model $\boldsymbol{\varepsilon}^p, (\boldsymbol{\alpha}_f)_{n+1}, (\mathbf{q}_f)_{n+1}$, the internal variables of the interface model $\beta_{n+1}^p, (\alpha_\Gamma)_{n+1}, q_{n+1}$, the total stresses and the microstresses $\{\boldsymbol{\sigma}\}$ and τ_f^I, σ_f^I, at the gauss point, respectively, at the end of the time step t_{n+1}, such that the incremental finite element equilibrium equation,

$$\mathfrak{R}\left(\mathbf{q}_{n+1}, \mathbf{p}_{n+1}^I\right) = \overset{nelem}{\underset{e=1}{\Lambda}} \left\{ \begin{array}{c} \mathbf{F}_{int}^e\left(\mathbf{q}_{n+1}, \mathbf{p}_{n+1}^I\right) - \mathbf{F}_{ext}^e \\ \mathbf{f}_{int}^e\left(\mathbf{q}_{n+1}, \mathbf{p}_{n+1}^I\right) \end{array} \right\} = \mathbf{0}, \tag{3.26}$$

is satisfied, where $\mathbf{F}_{int}^e$ and $\mathbf{f}_{int}^e$ are vectors of elemental forces, corresponding to

$$\mathbf{F}_{int}^e = \int_{\Omega^e} \left(\mathbf{B}^e\right)^T \hat{\boldsymbol{\sigma}}\left(\nabla^s \mathbf{q}_{n+1}, \mathbf{p}_{n+1}^I, \nabla \mathbf{p}_{n+1}^I, \boldsymbol{\alpha}_{n+1}\right) d\Omega^e,$$

$$\mathbf{f}_{int}^e = \int_{\Omega^e} \left([\mathbf{N}]^e \, \hat{\bar{\tau}}_f^{(I)}\left(\varepsilon_f\left(\nabla^s \mathbf{q}_{n+1}, \mathbf{p}_{n+1}^I, \nabla \mathbf{p}_{n+1}^I\right), (\alpha_f)_{n+1}\right) + \frac{A_f}{\Pi_f}[\mathbf{N}]_{,r}^e \, \hat{\bar{\sigma}}_f^{(I)}\left(\mathbf{p}_{n+1}^I, (\alpha_\Gamma)_{n+1}\right) \right) d\Omega^e. \tag{3.27}$$

The residual vector can be rewritten as a function of the global internal vector force, f_{int}^e defined as follows,

$$\mathfrak{R}\left(\mathbf{q}_{n+1}, \mathbf{p}_{n+1}^I\right) = \overset{nelem}{\underset{e=1}{\Lambda}} \left\{ f_{int}^e - f_{ext}^e \right\} = \mathbf{0},$$

$$f_{int}^e = \left\{ \begin{array}{c} \mathbf{F}_{int}^e\left(\mathbf{q}_{n+1}, \mathbf{p}_{n+1}^I\right) \\ \mathbf{f}_{int}^e\left(\mathbf{q}_{n+1}, \mathbf{p}_{n+1}^I\right) \end{array} \right\} \tag{3.28}$$

The set of equations (3.26) represents the HPFRC composite BVP problem, discretized in time and space, whose balance is established in equation (3.26). The t parameter stands for the increasing parameter (pseudo time identified as the loading factor or the arc length parameter). The equation (3.27) is a nonlinear one, and the source of nonlinearity is located in the constitutive functions that define the internal force vectors.

3.3.5.   The incremental solution procedure

The Newton Raphson algorithm is particularly attractive for solving of the nonlinear incremental equation (3.26). Due to its quadratic rates of asymptotic convergence, this method tends to produce generally robust and efficient incremental nonlinear finite element schemes (De Souza Neto et al. 2008). Nevertheless, in some cases, lack of robustness in nonlinear mechanics problems appears, for instance, as in modeling material failure for brittle materials. For a further thorough discussion the reader is addressed to (Oliver et al. 2008). Each iteration of the Newton Raphson scheme comprises the solution of the linearized version of the discrete incremental equilibrium equation (3.26). The linearized problem consists, then, in finding the fields $(\Delta \mathbf{q})^k$ and $(\Delta \mathbf{p}^I)^k$ at iteration k of the Newton Raphson as follows,

$$\mathfrak{K}_{tg}\Delta \mathrm{u}^k = -\mathfrak{R}^{k-1},$$

$$\Delta \mathrm{u}^k = \left\{ \begin{array}{c} (\Delta \mathbf{q})^k \\ (\Delta p^I)^k \end{array} \right\}, \tag{3.29}$$

where we have defined the Jacobian matrix (global tangent stiffness matrix):

$$\mathfrak{K}_{tg} = \frac{\partial \mathfrak{R}}{\partial \mathrm{u}_{n+1}}, \tag{3.30}$$

which is the assembly of the element tangent stiffness matrices. Further details of the form of this matrix are presented subsequently. Once the solution $\Delta \mathrm{u}^k$ of the linear system (3.29) is found, we can apply the correction to the global displacement

$$\mathrm{u}_{n+1}^k = \mathrm{u}_{n+1}^{k-1} + \Delta \mathrm{u}^k \tag{3.31}$$

The Newton Raphson iterative procedure is repeated till a convergence criterion is satisfied.

3.3.6.   Tangent stiffness matrix

The external forces in (3.26) do not depend on the current state u_{n+1}^{k-1}, then the expression (3.30) is reduced to:

$$\mathfrak{K}_{tg} = \frac{\partial f_{\mathrm{int}}}{\partial \mathrm{u}_{n+1}}. \tag{3.32}$$

Since the assembly operator is linear Λ, then:

$$\mathfrak{K}_{tg} = \overset{nelem}{\underset{e=1}{\Lambda}} \begin{bmatrix} K_{uu} & K_{u\beta} \\ K_{\beta u} & K_{\beta\beta} \end{bmatrix}^e, \tag{3.33}$$

where we have defined the submatrices,

$$\mathbf{K}_{uu} = \int_{\Omega_e} \left(\frac{\partial \mathbf{F}_{\mathrm{int}}^e \left(\boldsymbol{\sigma}_{n+1}^k \right)}{\partial \mathbf{q}_e \big|_{n+1}^k} \right) d\Omega_e,$$

$$\mathbf{K}_{u\beta} = \int_{\Omega_e} \left(\frac{\partial \mathbf{F}_{\mathrm{int}}^e \left(\boldsymbol{\sigma}_{n+1}^k \right)}{\partial \mathbf{p}_e^I \big|_{n+1}^k} \right) d\Omega_e, \tag{3.34}$$

$$\mathbf{K}_{\beta u} = \int_{\Omega_e} \left(\frac{\partial \mathbf{f}_{\mathrm{int}}^e \left(\left(\sigma_f \right)_{n+1}^k, \left(\tau_f \right)_{n+1}^k \right)}{\partial \mathbf{q}_e \big|_{n+1}^k} \right) d\Omega_e,$$

$$\mathbf{K}_{\beta\beta} = \int_{\Omega_e} \left(\frac{\partial \mathbf{f}_{\text{int}}^e \left(\left(\sigma_f\right)_{n+1}^k, \left(\tau_f\right)_{n+1}^k \right)}{\partial \mathbf{p}_e^I \big|_{n+1}^k} \right) d\Omega_e,$$

which stem from equation (3.32), when differentiation is performed respect to $\mathbf{q}_e$ and $\mathbf{p}_e^I$. By using the chain rule, equation (3.14) and equations in Box 3.3

$$\mathbf{K}_{uu} = \int_{\Omega_e} \left(\mathbf{B}_e^T \left\{ \frac{\partial \boldsymbol{\sigma}_{n+1}^k}{\partial \boldsymbol{\varepsilon}_{n+1}^k} \right\} \left\{ \frac{\partial \boldsymbol{\varepsilon}_{n+1}^k}{\partial \mathbf{q}_e \big|_{n+1}^k} \right\} \right) d\Omega_e,$$

$$\mathbf{K}_{uu} = \int_{\Omega_e} \left(\mathbf{B}_e^T \left\{ \frac{\partial \boldsymbol{\sigma}_{n+1}^k}{\partial \boldsymbol{\varepsilon}_{n+1}^k} \right\} \mathbf{B}_e \right) d\Omega_e, \tag{3.35}$$

$$\mathbf{K}_{uu} = \int_{\Omega_e} k_m \left(\mathbf{B}_e^T \left\{ \frac{\partial \left(\boldsymbol{\sigma}_m\right)_{n+1}^k}{\partial \boldsymbol{\varepsilon}_{n+1}^k} \right\} \mathbf{B}_e \right) d\Omega_e + \int_{\Omega_e} \sum_{I=1}^{nf} k_f^I \left(\mathbf{B}_e^T \left\{ \frac{\partial \left(\boldsymbol{\sigma}_f^I\right)_{n+1}^k}{\partial \boldsymbol{\varepsilon}_{n+1}^k} \right\} \mathbf{B}_e \right) d\Omega_e,$$

The total stress was substituted by their expression in terms of the concrete and the fiber stresses for each fiber bundle. The curly brackets indicate the conversion of the argument to matrix notation. The term $\mathbf{K}_{u\beta}$ is given by,

$$\mathbf{K}_{u\beta} = \int_{\Omega_e} \left(\mathbf{B}_e^T \left\{ \frac{\partial \boldsymbol{\sigma}_{n+1}^k}{\partial \boldsymbol{\varepsilon}_{n+1}^k} \right\} \left\{ \frac{\partial \boldsymbol{\varepsilon}_{n+1}^k}{\partial \mathbf{p}_e^I \big|_{n+1}^k} \right\} \right) d\Omega_e,$$

$$\mathbf{K}_{u\beta} = \int_{\Omega_e} \left(\mathbf{B}_e^T \left\{ \frac{\partial \boldsymbol{\sigma}_{n+1}^k}{\partial \boldsymbol{\varepsilon}_{n+1}^k} \right\} \left(\mathbf{T}_1 \left[\mathbf{N}\right]_{,r}^e + \mathbf{T}_2 \left[\mathbf{N}\right]_{,s}^e \right) \right) d\Omega_e,$$

$$\mathbf{K}_{u\beta} = \int_{\Omega_e} k_m \left(\mathbf{B}_e^T \left\{ \frac{\partial \left(\boldsymbol{\sigma}_m\right)_{n+1}^k}{\partial \boldsymbol{\varepsilon}_{n+1}^k} \right\} \left(\mathbf{T}_1 \left[\mathbf{N}\right]_{,r}^e + \mathbf{T}_2 \left[\mathbf{N}\right]_{,s}^e \right) \right) d\Omega_e + \dots \tag{3.36}$$

$$\int_{\Omega_e} \sum_{I=1}^{nf} k_f^I \left(\mathbf{B}_e^T \left\{ \frac{\partial \left(\boldsymbol{\sigma}_f\right)_{n+1}^k}{\partial \boldsymbol{\varepsilon}_{n+1}^k} \right\} \left(\mathbf{T}_1 \left[\mathbf{N}\right]_{,r}^e + \mathbf{T}_2 \left[\mathbf{N}\right]_{,s}^e \right) \right) d\Omega_e.$$

The submatrix $\mathbf{K}_{\beta u}$ corresponds to the following expression,

$$\mathbf{K}_{\beta u} = \int_{\Omega_e} \left(\frac{A}{\Pi} \left[\mathbf{N}\right]_{,r}^e \left\{ \frac{\partial \left(\sigma_f\right)_{n+1}^k}{\partial \varepsilon_e^f \big|_{n+1}^k} \right\} \left\{ \frac{\partial \varepsilon_e^f \big|_{n+1}^k}{\partial \mathbf{q}_e \big|_{n+1}^k} \right\} \right) d\Omega_e,$$

$$\mathbf{K}_{\beta u} = \int_{\Omega_e} \left(\frac{A}{\Pi} \left[\mathbf{N}\right]_{,r}^e \left\{ \frac{\partial \left(\sigma_f\right)_{n+1}^k}{\partial \varepsilon_e^f \big|_{n+1}^k} \right\} \mathbf{T}_1 \mathbf{B}^e \right) d\Omega_e, \tag{3.37}$$

and finally, the term $\mathbf{K}_{\beta\beta}$ is

$$\mathbf{K}_{\beta\beta} = \int_{\Omega_e} \left([\mathbf{N}]^e \left\{ \frac{\left(\tau_f\right)^k_{n+1}}{\partial \beta^f_e\big|^k_{n+1}} \right\} \left\{ \frac{\partial \beta^f_e\big|^k_{n+1}}{\partial \mathbf{p}^I_e\big|^k_{n+1}} \right\} + \frac{A}{\Pi}[\mathbf{N}]^e_{,r} \left\{ \frac{\left(\sigma_f\right)^k_{n+1}}{\partial \varepsilon^f_e\big|^k_{n+1}} \right\} \left\{ \frac{\partial \varepsilon^f_e\big|^k_{n+1}}{\partial \mathbf{p}^I_e\big|^k_{n+1}} \right\} \right) d\Omega_e,$$

$$\mathbf{K}_{\beta\beta} = \int_{\Omega_e} \left([\mathbf{N}]^e \left\{ \frac{\left(\tau_f\right)^k_{n+1}}{\partial \beta^f_e\big|^k_{n+1}} \right\} [\mathbf{N}]^e + \frac{A}{\Pi}[\mathbf{N}]^e_{,r} \left\{ \frac{\left(\sigma_f\right)^k_{n+1}}{\partial \varepsilon^f_e\big|^k_{n+1}} \right\} [\mathbf{N}]^e_{,r} \right) d\Omega_e.$$

(3.38)

Equations (3.35) to (3.38) complete the expressions defining the Jacobian matrix, as also, the linear approximation presented in equation (3.29).

3.3.7. The algorithmic tangent operators

To complete the algorithmic procedure discussed in previous subsections, it is required to derive the expressions of the coefficients:

$$\mathbf{C}_m^{a\lg} = \left\{ \frac{\partial \left(\boldsymbol{\sigma}_m\right)^k_{n+1}}{\partial \boldsymbol{\varepsilon}^k_{n+1}} \right\}, \quad \mathbf{C}_f^{a\lg} = \left\{ \frac{\partial \left(\boldsymbol{\sigma}_f^I\right)^k_{n+1}}{\partial \boldsymbol{\varepsilon}^k_{n+1}} \right\}, \quad \mathbf{C}_\Gamma^{a\lg} = \left\{ \frac{\left(\tau_f\right)^k_{n+1}}{\partial \beta^f_e\big|^k_{n+1}} \right\}$$

(3.39)

where $\mathbf{C}_m^{tg}$ is referred to as the *constitutive tangent operator* in matrix form. i.e. the fourth order tensor presented in Box 3.2, which is rewritten as a 3x3 matrix for plane stress and strain cases. In general, the matrix tangent operator for 2D problems is represented as,

$$\mathbf{C}_m^{tg} = \begin{bmatrix} C_{xxxx} & C_{xxyy} & C_{xxxy} \\ C_{yyxx} & C_{yyyy} & C_{yyxy} \\ C_{xyxx} & C_{xyyy} & C_{xyxy} \end{bmatrix}$$

(3.40)

The $ith-$ fiber tangent constitutive operator has the following form,

$$\mathbf{C}_f^{tg} = \begin{cases} E_f^I \mathbf{T}_3^I & iff \quad \left(f_f\right)^{trial}_{n+1} \leq 0 \\ \dfrac{E_f^I}{E_f^I + H_f^I} \mathbf{T}_3^I & iff \quad \left(f_f\right)^{trial}_{n+1} > 0 \end{cases}$$

(3.41)

$$\mathbf{T}_3^I = \begin{bmatrix} r_x^2 r_x^2 & r_x^2 r_y^2 & r_x^3 r_y \\ r_x^2 r_y^2 & r_y^2 r_y^2 & r_x r_y^3 \\ r_x^3 r_y & r_x r_y^3 & r_x^2 r_y^2 \end{bmatrix}$$

(3.42)

and the interface zone tangent constitutive operator is

$$\mathbf{G}_m^{tg} = \begin{cases} G_\Gamma^I & iff \quad \left(f_\Gamma\right)^{trial}_{n+1} \leq 0 \\ \dfrac{G_\Gamma^I}{G_\Gamma^I + H_\Gamma^I} & iff \quad \left(f_\Gamma\right)^{trial}_{n+1} > 0 \end{cases}$$

(3.43)

3.4.   Linear triangular and quadrangular elements with three degrees of freedom per node

The mixed formulation discussed in the preceding sections for the continuum with micro-structure based-model summarized in Box 3.2, is implemented by means of two types of linear finite elements, triangular and quadrangular elements. The triangular element with linear displacement interpolation is depicted in Figure 3.1-a, which has three degrees of freedom per node. According to the Gauss-Legendre quadrature rule, linear functions can be integrated exactly with one gauss point. Additional Lobatto integration scheme is also included to evaluate the kernel related with the bond shear stress term in the tangent stiffness matrix $\mathbf{K}_{\beta\beta}$, which is a *like-mass term*, as is shown later. The quadrilateral element is presented in Figure 3.1-b.
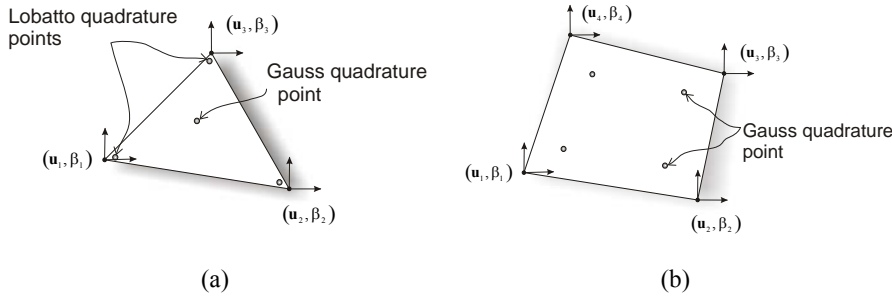
Figure 3.1. Linear triangular and linear quadrilateral elements.

3.4.1.   Internal force vector computation using triangular elements

As it can be observed in Box 3.4, the computational implementation of the force vector in the monolithic formulation, which is explained in the following section, has basically three steps. Note that the Lobatto integration rule is required by the mass-like term. Therefore, the procedure is divided in two integration steps. In step (iii) the integration with one gauss point is carried out to integrate the terms of equation (3.27) except the one associated with the mass-like term, and in step (iv) the term associated with the mass-like term is integrated using the Lobatto quadrature.

3.4.2.   Internal force vector computation using quadrilateral elements

The developed expressions for nodal forces and the residual vector also can be evaluated using quadrilateral elements as the one shown in Figure 3.1-b. The difference respect to the triangular element is the use of a four Gauss point quadrature, so that the Lobatto rule is not necessary in the calculation of the mass-like term.

Internal force vector computation for triangular element.

i.   Compute the standard $\mathbf{B}^{(e)}$ matrix (at the Gauss points ξ)

Compute test function $\mathbf{N}^{(e)}$ matrix (at the lobatto points $\tilde{\xi}$)

Compute test function $\left[\mathbf{N}\right]_{,r}^{e}$ matrix (at the Gauss points ξ)

ii. Set Gauss point coordinates ξ_i, and weights w_i, and Jacobian determinants j_i

iii.   DO $i_{gauss} = 1, n_{gauss}$

$$\left\{\boldsymbol{\sigma}^{m}\right\} := \Sigma^{m}\left(\boldsymbol{\varepsilon}_{m}, \alpha_{m}\right), \text{ compute matrix stresses vector}$$

DO $i_{fib} = 1, n_{fib}$

$$\left\{\boldsymbol{\sigma}_{f}^{I}\right\} := \Sigma^{f}\left(\left\{\boldsymbol{\varepsilon}_{f}^{I}\right\}, \alpha_{f}^{I}\right), \text{ compute global fiber stresses}$$

END DO

$$\left\{\boldsymbol{\sigma}\right\} = k_{m} \cdot \left\{\boldsymbol{\sigma}_{m}\right\} + \sum_{I=1}^{nfib} k_{f}^{I} \cdot \left\{\boldsymbol{\sigma}_{f}^{I}\right\}$$

Calculate the element internal force vector

$$\mathbf{F}_{int}^{(e)} := \mathbf{F}_{int}^{(e)} + w_{i} j_{i} \left(\mathbf{B}^{T}\right)^{e} \left\{\boldsymbol{\sigma}\right\}$$

$$\mathbf{f}_{int}^{(e)} := \mathbf{f}_{int}^{(e)} + \frac{A^{f}}{\Pi^{f}} w_{i} j_{i} \left[\mathbf{N}\right]_{,r}^{e} \mathbf{T}_{1} \left\{\boldsymbol{\sigma}_{f}^{I}\right\}$$

END DO

iv. Integrate of the mass term at the Lobatto points $\tilde{\xi}_{I_{lob}}$

DO $I_{lob} = 1, n_{lob}$

$$\tau_{f}^{I} := \hat{\tilde{\tau}}\left(\mathbf{p}^{I}, \alpha_{\Gamma}\right), \text{ compute fiber stress}$$

$$\mathbf{f}_{int}^{(e)} := \mathbf{f}_{int}^{(e)} + w_{I_{lob}} j_{I_{lob}} \left[\mathbf{N}\right]^{e} \left\{\tau_{f}^{I}\right\}$$

END DO

Box 3.4. Procedure for the internal force vector computation (triangular element).

3.4.3.   Computation of triangular and quadrilateral elemental matrices

For the triangular element, the computation of the element matrices follows the procedure given in Box 3.5. The operations at Gauss point level involve the total evaluation of the $\mathbf{K}_{uu}^{(e)}$, $\mathbf{K}_{u\beta}^{(e)}$ and $\mathbf{K}_{\beta u}^{(e)}$ terms. The $\mathbf{K}_{\beta\beta}^{(e)}$ contribution is partially evaluated at Gauss point level in step (iv) and in step (v) the mass-like term is computed using the Lobatto quadrature rule.

Elemental tangent stiffness matrix computation for triangular element.

i.   Compute the standard $\mathbf{B}^{(e)}$ matrix (at the Gauss points ξ)

Compute test function $\mathbf{N}^{(e)}$ matrix (at the Lobatto points $\tilde{\xi}$)

Compute test function $\left[\mathbf{N}\right]_{,r}^{e}$ matrix (at the Gauss points ξ)

ii.   Set Gauss point coordinates ξ_i, and weights w_i, and Jacobian determinants j_i

iii.   DO $i_{gauss} = 1, n_{gauss}$

DO $I = 1, n_{fib}$

E_{tg}^{I}, G_{tg}^{I} compute fiber and interface zone tangent constitutive operator, respectively. Equations (3.41) and (3.43)

END DO

Calculate element matrix $\mathbf{K}_{uu}^{(e)}$, $\mathbf{K}_{u\beta}^{(e)}$, $\mathbf{K}_{\beta\beta}^{(e)}$ according to equations (3.35) to (3.38)

END DO

iv.   Calculate the integrant of the mass term the Lobatto points $\tilde{\xi}_I$

v.   DO $I_{lobatto} = 1, n_{lobatto}$

G_{tg}^{I} , compute fiber stress

Calculate element matrix $\mathbf{K}_{\beta\beta}^{(e)}$ $\mathbf{K}_{\beta\beta}^{(e)} = \mathbf{K}_{\beta\beta}^{(e)} + \sum_{I=1}^{nf}\left[\mathbf{N}\right]G_{tg}^{I}\left[\mathbf{N}\right]w_{I_{lob}} j_{I_{lob}}$

END DO

Box 3.5. Procedure for elemental tangent stiffness matrix computation for triangular elements

The implementation of the quadrilateral element involves slight differences respect to the triangular element case. All the contributions to the tangent stiffness matrix are computed using the Gauss quadrature rule.

3.4.4.   Evolution of the mass-like term of the triangular element

In order to compute adequately the internal force vector, the proposed scheme requires the integration of the mass-like by means of the Lobatto quadrature rule. The first term of equation (3.15) is given by,

$$\int_{\Omega^{(e)}} [\mathbf{N}]^e \, G_{tg}^{ifib} \, [\mathbf{N}]^e \cdot dV = \int_{\Omega^{(e)}} G_{tg}^{ifib} \begin{bmatrix} N_1^2 & N_1 N_2 & N_1 N_2 \\ & N_2^2 & N_1 N_2 \\ Sym & & N_3^2 \end{bmatrix} dV \ , \tag{3.44}$$

a lumped, diagonal mass-like matrix can be obtained by the Lobatto integration rule, with the quadrature points coinciding with the nodes

$$\int_{\Omega^{(e)}} [\mathbf{N}]^e \, G_{tg}^{ifib} \mathbf{N}^e \cdot dV = \sum_{I_{lob}=1}^{n_{lobatto}} G_{tg}^{ifib} N_{I_{lob}} N_{I_{lob}} \mathbf{I} w_{I_{lob}} j_{I_{lob}} \ . \tag{3.45}$$

3.5.   Time integration scheme

The selection of the time integration methods depends, among other aspects, on: the type of partial differential equations and the smoothness of the data and the response of interest. However, for general coupled problems, two strategies are available: monolithic and fractional step methods (also known as staggered techniques) (Patrick et al. 1993). The first approach consists of solving simultaneously all the fields involved in the problem. This procedure usually involves a very large system of equations. In the second approach, the system is partitioned in several smaller and simpler subsystems that take advantage of the physical nature of the problem. In some specific cases, this strategy leads to a much lower computational cost and modularity in the implementation that allows efficient combination of methods.

The discrete problem in time and space, equation (3.26), corresponds to the coupled model for the HPFRC composite. As shown there, in this system, there exist a clear dependence between the unknown variables $\mathbf{q}$ and $\mathbf{p}^I$, which suggests an integration algorithm that solves simultaneously both fields. However, we will show that this system of equations can alternatively be integrated using a staggered solution procedure, which originates as many partitions as families of fibers are consider in the analysis plus one ($nf + 1$). This procedure will be explained in more detail in section 3.5.2.

3.5.1.   Monolithic scheme

A single discretization method is applied to the coupled system, using the space-time finite elements in equation (3.26) in the case of the monolithic scheme. The whole problem is treated as a monolithic entity, and all components advanced simultaneously in time. The Newton Raphson scheme for the solution of the residual equation (3.26) is shown in Box 3.6.

<div style="border:1px solid">

Small strain, small displacement formulation for the triangular and quadrangular element, Newton-Raphson loop

$k := 0$, set the initial guess and the residual

i.   Compute the consistent tangent matrices

$$\mathbb{C}_{tg}^m = \partial\boldsymbol{\sigma}^m / \partial\boldsymbol{\varepsilon}^m, \quad E_{tg}^f = \partial\sigma'^f / \partial\varepsilon'^f, \quad G_{tg}^f = \partial\tau'^f / \partial\beta^f$$

ii.   Compute the elemental matrix contributions $\mathbf{K}_{uu}^{(e)}$, $\mathbf{K}_{u\beta}^{(e)}$, $\mathbf{K}_{\beta u}^{(e)}$, $\mathbf{K}_{\beta\beta}^{(e)}$ and the assembly in the global matrix

$$\left(\mathbf{K}_{tg}\right)^e = \begin{bmatrix} \mathbf{K}_{uu} & \mathbf{K}_{u\beta} \\ \mathbf{K}_{\beta u} & \mathbf{K}_{\beta\beta} \end{bmatrix}, \qquad \mathfrak{K}_{tg} = \overset{n^{elem}}{\underset{e=1}{\Lambda}} \left(\mathbf{K}_{tg}\right)^e$$

iii.   Solve the linearised equation for $\Delta\mathbf{q}$ and $\Delta\mathbf{q}$

$$\mathfrak{K}_{tg}\Delta u^{(k)} = -\mathfrak{R}; \quad \Delta u^{(k)} = \begin{Bmatrix} \Delta\mathbf{q}^{(k)} \\ \Delta\mathbf{p}^{(k)} \end{Bmatrix}$$

iv.   Apply Newton-Raphson correction to the nodal displacement vector

$$\mathbf{q}^{(k)} = \mathbf{q}^{(k-1)} + \Delta\mathbf{q}$$
$$\mathbf{p}^{(k)} = \mathbf{p}^{(k-1)} + \Delta\mathbf{p}$$

v.   Compute the elemental internal forces and assemble in the global vector

$$f_{int}^{(e)} = \begin{Bmatrix} \mathbf{F}_{int}^{(e)} \\ \mathbf{f}_{int}^{(e)} \end{Bmatrix}, \qquad f^{int} = \overset{n^{elem}}{\underset{e=1}{\Lambda}} \left\{ f_{int}^{(e)} \right\}$$

vi.   Compute the residual vector $\mathfrak{R} = f^{int} - f^{ext}$

vii.   Check convergence. If $\left\| \mathfrak{R} \right\| \le \epsilon_{tol}$ then accept $(\cdot)^{(k)}$ as the solution and exit. Else, set $k := k+1$ and GOTO (i)

</div>

Box 3.6. Monolithic scheme

The procedure in Box 3.6 is presented as the monolithic scheme because both equations in (3.26) are solved simultaneously for $\Delta \mathbf{q}$ and $\Delta \mathbf{p}^I$,. The main part of the procedure is the calculation of the nodal internal forces and the tangent matrix, which follows the procedures explained in Box 3.4 and Box 3.5 for the triangular element and quadrangular element, respectively.

3.5.2.   Staggered scheme

In the staggered scheme, the coupled system of equations written as an incremental finite element problem (3.26) can be partitioned into $nf+1$ field model, where nf is the numbers of fiber bundles considered, and it is computationally treated as isolated entities that are separately stepped in time. Interaction effects are viewed as forcing effects that are communicated between the individual components using prediction and substitution techniques (Felippa et al. 2001). Partitioning of the set of equations can be represented as in Figure 3.2, in which the $nf+1$ different fields $\mathbf{q}$ and $\mathbf{p}^I$ $\left(\forall I = 1,\dots,nf \right)$ are the solutions of the partitioned system.
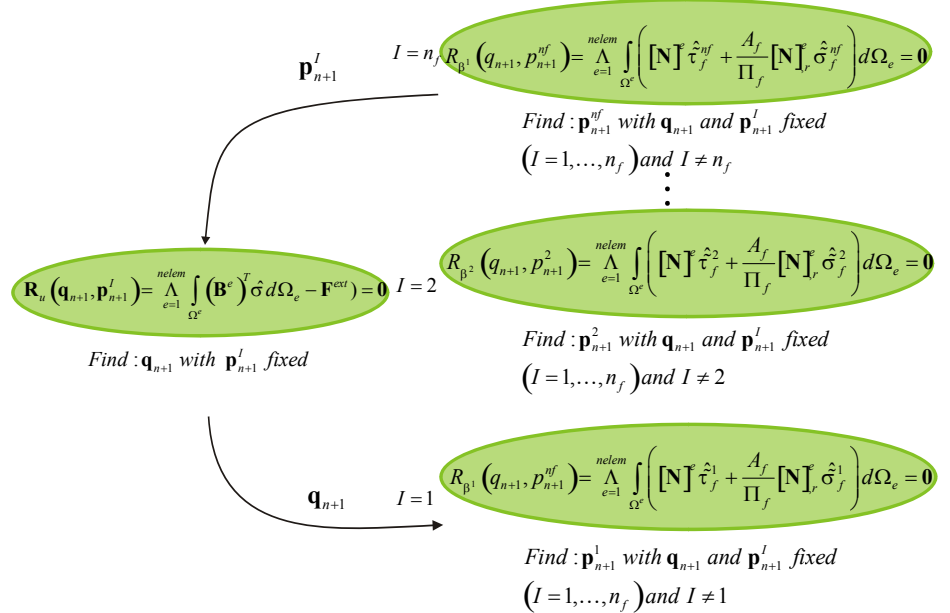
Figure 3.2. Staggered scheme for solving the coupled equation system.

The partitioned solution procedure is obtained by substituting the integration scheme by the following,

$$\mathbf{q}_{n+1}^k = \mathbf{q}_n + \Delta \mathbf{q}_{n+1}^k ,$$

$$\left(\mathbf{p}^I \right)_{n+1}^k = \left(\mathbf{p}^I \right)_{n+1}^P + \left(\Delta \mathbf{p}^I \right)_n^k ,$$

(3.46)

where the prediction of the slip, $\left(\mathbf{p}^I\right)_{n+1}^P$, is given by,

$$\left(\mathbf{p}^I\right)_{n+1}^P = \left(\mathbf{p}^I\right)_n + \Delta\mathbf{p}^I \frac{\Delta t_{n+1}}{\Delta t_n}. \tag{3.47}$$

where, $\Delta\mathbf{p}^I$ is the increment of the solution of $\mathbf{p}^I$ in the previous step. Here, the linear extrapolation of the slip $\left(\mathbf{p}^I\right)_n$ of the fiber bundle I is $\left(\mathbf{p}^I\right)_{n+1}^P$. This value is chosen as the predictor and it keeps the stability of the algorithm.

After substituting (3.46), the set of equations (3.30) becomes,

$$\begin{bmatrix} \mathbf{K}_{uu} & \mathbf{0} \\ \mathbf{K}_{\beta u} & \mathbf{K}_{\beta\beta} \end{bmatrix} \begin{Bmatrix} \Delta\mathbf{q} \\ \Delta\mathbf{p}^I \end{Bmatrix} = \begin{Bmatrix} -\mathbf{R}_u - \mathbf{K}_{u\beta}\left(\mathbf{p}^I\right)_{n+1}^P - \mathbf{K}_{u\beta}\left(\mathbf{p}^I\right)_n \\ -\mathbf{R}_\beta \end{Bmatrix} \tag{3.48}$$

In the first set of equation (3.48), the only unknown is $\Delta\mathbf{q}$, i.e.

$$\Delta\mathbf{q} = -\mathbf{K}_{uu}^{-1}\left(\mathbf{R}_u - \mathbf{K}_{u\beta}\left(\left(\mathbf{p}^I\right)_{n+1}^P - \left(\mathbf{p}^I\right)_n\right)\right) \quad with \quad \mathbf{q}_{n+1}^k = \mathbf{q}_n + \Delta\mathbf{q} \tag{3.49}$$

Then, the value of $\mathbf{p}_{n+1}^k$ is obtained by freezing the value of $\mathbf{q}_{n+1}^k$ and solving the second equation in (3.48), as follows:

$$\Delta\mathbf{p} = \mathbf{K}_{\beta\beta}^{-1}\left(-\mathbf{R}_\beta - \mathbf{K}_{\beta u}\left(\mathbf{q}_{n+1}^k - \mathbf{q}_n\right)\right) \tag{3.50}$$

The solution of the equation system (3.48) is therefore accomplished following the basic steps that are displayed in Box 3.7.

Basic steps		
1. Prediction :	$\left(\mathbf{p}^I\right)_{n+1}^P = \left(\mathbf{p}^I\right)_n + \Delta\mathbf{p}^I \dfrac{\Delta t_{n+1}}{\Delta t_n}$	(3.51)
2. Advance:	$\Delta\mathbf{q}^k = \left(\mathbf{K}_{uu}\right)^{-1}\left(-\mathbf{R}_u - \mathbf{K}_{u\beta}\left(\left(\mathbf{p}^I\right)_{n+1}^P - \left(\mathbf{p}^I\right)_n\right)\right)$	(3.52)
3. Substitute:	$\mathbf{q}_{n+1}^k = \mathbf{q}_n + \Delta\mathbf{q}_{n+1}^k$	(3.53)
4. Advance:	$\left(\Delta\mathbf{p}^I\right)^k = \left(\mathbf{K}_{\beta\beta}\right)^{-1}\left(-\mathbf{R}_\beta - \mathbf{K}_{\beta u}\left(\mathbf{q}_{n+1}^k - \mathbf{q}_n\right)\right)$	(3.54)

Box 3.7. Basic steps of the staggered solution

The main achievement is that the set of equations in (3.48) can be solved now in tandem. A graphical representation of the proposed scheme, with time along the horizontal axis, is shown in Figure 3.3.
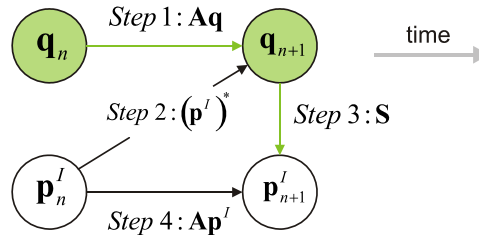
Figure 3.3. Staggered solution. Time stepping diagram.

In the staggered approach, the equations are solved first for $\Delta\mathbf{q}$ and based on this, equations are computed for the slip $\Delta\mathbf{p}^I$ at each fiber bundle. The overall algorithm for the integration of the staggered scheme is listed in Box 3.8. This algorithm is divided in $nf + 1$ partitions; the first partition is computed once, while the partition solving the second equation in (3.54) is repeated as many times as fiber bundles are considered in the analysis.

This scheme has two main advantages with respect to the monolithic one: i) the staggered scheme is based on a simpler implementation when the number of fiber bundles change; also, ii) the staggered scheme provides a reduction in the size of matrices involved in the solution of each subsystem. Therefore, a significant saving in computational cost can be expected, being more important when the number of fiber bundles increases.
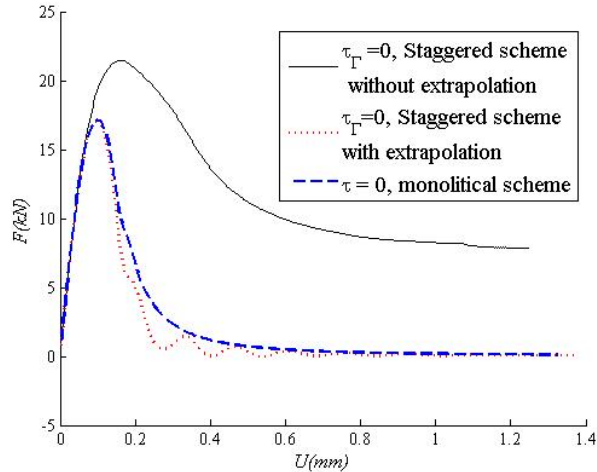
Figure 3.4. Linear triangular and linear quadrangular elements.

The staggered scheme implies that the value of $\mathbf{p}^I$ is frozen in the first partition and the value of $\mathbf{q}$ is frozen in the partition 2 to $n_{partition}$. The application of the strategy summarized in Box 3.8 showed that staggering does not harm stability if the predictor is used as the extrapolation of the $\mathbf{p}_n^I$, otherwise, it was observed instability in the results. This effect can be seen in Figure 3.4, which represents the response of the beam in example 5 when the effect of the interface zone vanishes. It seems that the use of $\mathbf{p}_n^I$ as a predictor generates a spurious strength. However, the use of the predicted value of $\mathbf{p}^I$ as the linear extrapolation of

$\mathbf{p}_n^I$ (equation (3.47)), instead of $\mathbf{p}_n^I$ reduces the amplification of the error and improves the performance or the staggered approach.

Steps of staggered scheme procedure.

LOOP over time steps: $n+1$

i.
Prediction: set $\left(\mathbf{p}_{n+1}^I\right)^P = \mathbf{p}_n^I + \Delta\mathbf{p}^I \dfrac{\Delta t_{n+1}}{\Delta t}$ $\forall I = 1,\ldots,nf$

Initialize: $\left(\mathbf{p}_{n+1}^I\right)^0 = \left(\mathbf{p}_{n+1}^I\right)^P$; $\left(\mathbf{p}_{n+1}^I\right)^{-1} = \left(\mathbf{p}_n^I\right)$; $\left(\mathbf{q}_{n+1}\right)^0 = \mathbf{q}_n$

WHILE NOT CONVERGE: iteration k

ii.   Advance : .

Given $\left(\mathbf{p}_{n+1}^I\right)^{k-1}$, $\mathbf{q}_{n+1}^{k-1}$, Compute the nodal displacement vector $\mathbf{q}_{n+1}$

Apply Newton Raphson for solving the linearised equation for $\Delta\mathbf{q}$

$$\mathbf{q}_{n+1}^k = \mathbf{q}_{n+1}^{k-1} + \left(\mathbf{K}_{uu}\right)^{-1}\left(-\mathbf{R}_u - \mathbf{K}_{u\beta}\left(\left(\mathbf{p}^I\right)_{n+1}^P - \left(\mathbf{p}^I\right)_n\right)\right)$$

iii.   Substitution:

Set $\mathbf{q}_{n+1}^k = \mathbf{q}_n + \Delta\mathbf{q}_{n+1}^k$

iv.   Advance:

Given $\mathbf{q}_{n+1}^{k+1}$, $\left(\mathbf{p}_{n+1}^I\right)^{k-1}$, Compute the nodal displacement vector $\mathbf{p}_{n+1}^I$

DO $I = 1,\ldots,n_f$

Apply Newton Raphson for solving the linearised equation for $\Delta\mathbf{p}^I$

$$\left(\mathbf{p}^I\right)_{n+1}^k = \left(\mathbf{p}^I\right)_{n+1}^{k-1} + \left(\mathbf{K}_{\beta^I\beta^I}\right)^{-1}\left(-\mathbf{R}_{\beta^I\beta^I} - \mathbf{K}_{\beta^I u}\left(\mathbf{q}_{n+1}^k - \mathbf{q}_n\right)\right)$$

$$\mathbf{p}_{n+1}^I = \mathbf{p}_n^I + \Delta\mathbf{p}^I$$

END DO

END WHILE

END LOOP over time steps

Box 3.8. Staggered scheme procedure.

When using the staggered scheme, accuracy is usually degraded with respect to that attainable by the monolithic scheme. In order to recover the accuracy of the monolithic scheme, one global iteration at the same step to find new values of $\mathbf{p}_{n+1}^I$ and $\mathbf{q}_{n+1}$ can also be performed, once the fields are substituted in the initial residual equation (3.26).

3.5.3.   IMPL-EX scheme

Implicit integration schemes using the Newton-Raphson procedure often show lack of robustness when material failure problems are addressed. In (Oliver et al. 2008) the IMPLEX algorithm was presented based on two general families of constitutive models, namely, continuum damage and elasto-plasticity. A typical material non-linear solid mechanics problem can be written in the form presented in Box 3.9 after the selection of the discretization scheme and the time marching algorithm.

Find:	$u_{n+1}; \alpha_{n+1}; \boldsymbol{\sigma}_{n+1}$	(3.55)
Such that:		
Equilibrium equations	$f_{\text{int}}\left(u_{n+1}, \boldsymbol{\sigma}_{n+1}, t_{n+1}\right) - f_{ext}\left(t_{n+1}\right) = \mathbf{R}\left(u_{n+1}, \boldsymbol{\sigma}_{n+1}, t_{n+1}\right) = \mathbf{0}$	(3.56)
Internal variable evolution equations	$g\left(\alpha_{n+1}, \Delta\alpha_{n+1}, \boldsymbol{\sigma}_{n+1}, t_{n+1}\right) = 0$	(3.57)
Constitutive equation	$\dot{\boldsymbol{\sigma}}_{n+1} = \dfrac{\boldsymbol{\sigma}_{n+1} - \boldsymbol{\sigma}_n}{\Delta t_{n+1}} = \Sigma\left(\boldsymbol{\varepsilon}\left(u_{n+1}\right), \alpha_{n+1}, \boldsymbol{\sigma}_{(\cdot)}\right)$	(3.58)

Box 3.9. Typical material non-linear solid mechanics model.

where u_{n+1} are the nodal displacement at the end of the step $n+1$, α_{n+1} stands for strain like variables and $\boldsymbol{\sigma}_{n+1}$ for the stresses at the sampling point. Here is considered a typical step over the time interval $[t_n, t_{n+1}]$. According to the proposed methodology considered in the IMPL-EX algorithm, the integration can be written as a fractional step method for the integration of a global time evolution problem. The first step constitutes the explicit stage of the IMPL-EX scheme and the non linear system of equations has to be iteratively solved to find the value of u_{n+1}. However, it was shown by Oliver et al (Oliver et al. 2008) that for the damage model and for the linear plastic flow cases, it becomes a linear system of equations. The second step corresponds to the IMPL-EX implicit stage. Then, the value u_{n+1} remains frozen and the implicit integration of the constitutive model is done. In Box 3.10 is summarized the IMPL-EX integration scheme for the global time evolution problem.

In the explicit step, equation (3.60) constitutes an explicit extrapolation of the internal variable , α , at the time step t_{n+1}, in terms of the implicit variables obtained in the previous time steps n and $n+1$. $\Delta\alpha$ is the increment of the internal variable determined implicitly in the previous steps n and $n-1$; $\Delta\alpha = \alpha_n - \alpha_{n-1}$. Then, the stresses are computed, in equation

(3.49), using backward-Euler integration scheme and finally the balance equation (3.59) is solved to find $\mathfrak{u}_{n+1}$.

IMPLEX scheme

Explicit stage: $\mathfrak{u}_{n+1}$

$$f_{\text{int}}\left(\mathfrak{u}_{n+1},\tilde{\boldsymbol{\sigma}}_{n+1},t_{n+1}\right)-f_{ext}\left(t_{n+1}\right)=\mathbf{0} \qquad (3.59)$$

$$\tilde{\alpha}_{n+1}=\alpha_n+\frac{\Delta t_{n+1}}{\Delta t_n}\Delta\alpha_n \qquad (3.60)$$

$$\dot{\tilde{\boldsymbol{\sigma}}}_{n+1}=\frac{\tilde{\boldsymbol{\sigma}}_{n+1}\left(\mathfrak{u}_{n+1}\right)-\boldsymbol{\sigma}_n}{\Delta t_{n+1}}=\Sigma\left(\boldsymbol{\varepsilon}\left(\mathfrak{u}_{n+1}\right),\tilde{\alpha}_{n+1},\tilde{\boldsymbol{\sigma}}_{n+1}\right) \qquad (3.61)$$

Implicit stage: $\alpha_{n+1},\boldsymbol{\sigma}_{n+1}$

$$\dot{\mathfrak{u}}_{n+1}=0 \qquad (3.62)$$

$$g\left(\alpha_{n+1},\boldsymbol{\sigma}_{n+1},t_{n+1}\right)=0 \qquad (3.63)$$

$$\dot{\boldsymbol{\sigma}}_{n+1}=\frac{\boldsymbol{\sigma}_{n+1}\left(\mathbf{d}_{n+1}\right)-\boldsymbol{\sigma}_n}{\Delta t_{n+1}}=\Sigma\left(\boldsymbol{\varepsilon}\left(\mathfrak{u}_{n+1}\right),\alpha_{n+1},\boldsymbol{\sigma}_{n+1}\right) \qquad (3.64)$$

Box 3.10. Implex scheme

Since the constitutive equation of the composite material and the compounds are path-dependent, i.e., they depend on the history of the strains to which the solid has been subjected, the stresses are the solution of a constitutive initial value problem. Therefore, an appropriate numerical algorithm is an essential requirement for the integration of the rate constitutive equation. In general, algorithms for the integration of the rate constitutive equations are obtained by adopting some kind of time discretization. Here, it is considered the time increment $\left[t_n,t_{n+1}\right]$ and Backward Euler scheme. In this time interval, given the sets $\alpha_n,\left(\alpha_f\right)_n,\left(\alpha_\Gamma\right)_n$ of internal variables at t_n and strains $\left(\boldsymbol{\varepsilon}_m\right)_{n+1},\left(\boldsymbol{\varepsilon}_f\right)_{n+1},\beta$ at time t_{n+1} must be determined the stresses $\left(\boldsymbol{\sigma}_m\right)_{n+1},\left(\boldsymbol{\sigma}_f\right)_{n+1}$ and τ_{n+1} uniquely through the integration algorithm. The incremental constitutive functions $\hat{\boldsymbol{\sigma}}_m,\hat{\tilde{\boldsymbol{\sigma}}}_f,\hat{\tilde{\tau}}$ are

$$\left(\boldsymbol{\sigma}_m\right)_{n+1}=\hat{\boldsymbol{\sigma}}_m\left(\left(\alpha_m\right)_n,\left(\boldsymbol{\varepsilon}_m\right)_{n+1}\right),$$

$$\left(\boldsymbol{\sigma}_f\right)_{n+1}=\hat{\tilde{\boldsymbol{\sigma}}}_f\left(\left(\alpha_f\right)_n,\left(\boldsymbol{\varepsilon}_f\right)_{n+1}\right), \qquad (3.65)$$

$$\tau_{n+1}=\hat{\tilde{\tau}}_f\left(\left(\alpha_\Gamma\right)_n,\beta_{n+1}\right).$$

The solution procedure of the nonlinear incremental equation (3.65) requires two fundamental operations:

1. The state update procedure, which gives the stresses $\left(\boldsymbol{\sigma}_m\right)_{n+1}, \left(\boldsymbol{\sigma}_f\right)_{n+1}$ and τ_{n+1}, and the internal variables. The stresses delivered by the incremental constitutive function are used to assemble the elemental incremental force vector.
2. The computation of the associated constitutive tangent modulus to be used to evaluate the tangent stiffness matrix.

Denoting the IMPL-EX variables at time $n+1$ with the symbol $(\tilde{\ })$ and the implicit ones without a specific symbol, then the IMPL-EX, strain-like internal variable can be determined as follows:

$$\tilde{\alpha}_{n+1} = \alpha_n + \Delta\tilde{\alpha}_{n+1} \quad ; \quad \Delta\tilde{\alpha}_{n+1} = \left(\alpha_{n+1} - \alpha_n\right)\frac{\Delta t_{n+1}}{\Delta t_n} \tag{3.66}$$

And the stress-like variables are:

$$\tilde{q}_{n+1} = q_n + H\left(\alpha_n\right)\Delta\tilde{\alpha}_{n+1} \tag{3.67}$$

After replacing these IMPL-EX internal variables in the constitutive equation, Boxes (2.1), (2.3) and (2.4) The incremental (rate) stress term, $\Delta\tilde{\sigma}_{n+1}$ is determined from these equations, and the IMPL-EX stress at time $n+1$ is given by:

$$\tilde{\sigma}_{n+1} = \sigma_n + \Delta\tilde{\sigma}_{n+1} \tag{3.68}$$

It can be shown (see (Oliver et al. 2006a)) that, even during the material softening regime, the consistent tangent matrices, arising from this integration algorithm, are constant and positive definite. Thus, it is introduced the IMPL-EX stress $\tilde{\sigma}_{n+1}$ into the equilibrium equations of Box 3.2 in order to find the displacement solution of the corresponding discrete problem.

The tangent operator is required for the evaluation of the new stiffness tangent matrix. They are calculated using expressions (3.40) to (3.45) in the implicit case. However, in the context of nonlinear solid problems, the tangent operators are positive definite at initial stages of the analysis and loose this character at those points where material failure occurs (Oliver et al. 2008). In consequence, eventually, the global tangent stiffness matrix may be close to singular, (the condition number of the global stiffness matrix is close to zero), and the convergence could fail. Results of using of the IMPL-EX algorithm showed that it provides tangent matrices which are in all cases symmetric and semi-positive definite. Therefore, the condition number of the resulting algorithmic stiffness matrix remains positive all along the analysis. This feature of the IMPL-EX integration scheme remedies dramatically the problems associated with loose of positive definiteness and provides robustness of the numerical simulations. The computation of the tangent stiffness matrix in the IMPLEX scheme requires the evaluation of the IMPL-EX algorithmic tangent operator corresponding to

$$\tilde{\mathbf{C}}_{n+1}^{a\lg} = \frac{\partial\tilde{\boldsymbol{\sigma}}_{n+1}}{\partial\boldsymbol{\varepsilon}_{n+1}}. \tag{3.69}$$

which is symmetric in all cases and semi-positive definite. Additionally, it is constant for the damage model and the elasto-plastic model for the linear plastic flow. Further detailed dis-

cussion about this topic is addressed in the work presented by Oliver and coworkers (Oliver et al. 2008).

Chapter 4
Modeling material failure of HPFRC composites

4.1.   Introduction

In HPFRC composites, three typical deformation stages are associated with the uniaxial tensile response, namely, elastic deformation, multiple cracking and damage localization. Physically, the damage progression sequence begins with initial flaws or microcracks that are always presented in the cementitious composite, as illustrated Figure 4.1.

When load is first applied to the HPFRC composite, areas of stress concentration develop at the tips of the initial cracks. With additional loading, microcracks form, grow and coalesce into macrocracks (Kim et al. 2002). However, the energy needed to open a critical crack exceeds the energy that is necessary to form new microcracks, provoking multiple cracking before crack localization, as a direct effect of the presence of the fibers. The fibers retard the strain localization by means of the "bridging effect". In fact, a bridged crack can absorb more or less energy depending on their bond characteristics. The energy absorption, during multicracking, also depends on the fiber deformation during pullout, which contributes directly to the total deformation of the composite (Suwannakarn 2009). This explains the ductility properties of the HPFRC composite. The failure process is completed, when the microcracking reaches a saturated level, and their coalescence triggers the formation of a macrocrack, then it propagates rapidly causing failure.
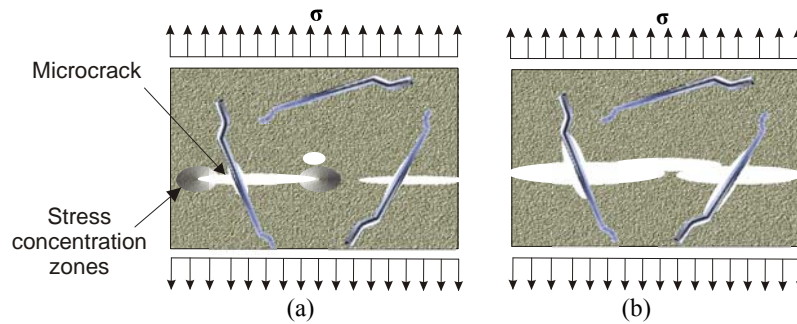
Figure 4.1. (a) Crack configuration prior to coalescence and, (b) after coalescence, adapted from
(Lange-Kornbak & Karihaloo 1997)

Different criteria have been formulated and used to predict the initiation of macroscopic material failure under various loading conditions, which are usually characterized by using local concepts. The physical foundation for these failure criteria might be different, and the individual validity may be restricted to specific types of material and structural problems (Li 2001). For steel fiber reinforced concrete composite materials, the difficulties imposed by the macro- and micromechanical heterogeneities and the complexity of the failure mechanism, limit the use of the failure criteria available. Some of these models appear in (Beghini et al. 2007) and (Hu et al. 2003). In the present chapter, the fracture model adopted for the prediction of the mechanical failure of the HPFRC composite is described, as well as the implementation issues.

4.1.1.   Continuum approach to material failure

In computational failure mechanics, the global material failure under quasi-static loads for ductile and quasi-brittle material is characterized, from the macroscopical point of view, by the onset and propagation of failure lines (in 2D) or failure surfaces (in 3D) (Oliver & Huespe 2004b). Continuum approaches based on the classical continuum (strain localization, smeared cracking, or the enriched continuum) aim at modeling the concentration of the strain in narrow bands, via the introduction of constitutive strain softening, whose propagation makes eventually the structure to fail (Oliver & Huespe 2004a). The use of standard finite elements and classical continuum stress-strain constitutive models equipped with strain softening, suffers from classical spurious mesh size and mesh-bias dependence. Mesh size effect is overcome by using an appropriate regularization of the softening modulus value based on fracture energy concepts. However, in the classical approach the spurious mesh-bias dependence is not easily removed and it is required some additional sophistication. Due to the poor kinematical representation of the standard finite elements, (Simo et al. 1993) and (Simo & Oliver 1994) proposed a methodology based on the concept of strong discontinuity. In the strong discontinuity approach (SDA), the real discontinuity in the displacement field is aimed at being modeled and captured via an appropriate mechanical theory and different

families of standard finite elements enriched by discontinuous deformation modes (Dias 2012). The proposed methodology in this work includes:

1. The softening modulus regularization: On the pure mechanical grounds, the post peak softening of the material cannot depend on the assumed discretization, in other words, it would completely depend on the number of elements or the element size. This theoretical difficulty was detected and described by Bažant as a not objective property (Bažant & Planas 1998). Therefore, softening modulus regularization is required to achieve mesh size objectivity.

2. The prediction of the instant at which the localization process onsets. It requires the bifurcation analysis.

3. The injection of constant strain localization modes via mixed finite element formulations to the injection domain, which will be defined in the following sections.

The material failure model is based on the approach presented by (Dias 2012), in which the strain localization methods are combined with the injection of constant strain modes and elemental strong discontinuity modes. However, in the fracture model adopted for the HPFRC composite, only elemental enrichment with constant strain modes is performed to remove the spurious mesh orientation. This is considered sufficient to provide enough information on the involved phenomena for the purposes of assessment of the proposed micromorphic approach.

4.1.2.   Strain localization

Strain localization is a feature that naturally occurs to materials displaying softening. The phenomenon manifests in the form of localization bands that are narrow zones of intense straining. Let us consider a bar, which material displays strain softening, under axial stretching, as is sketched in Figure 4.2.
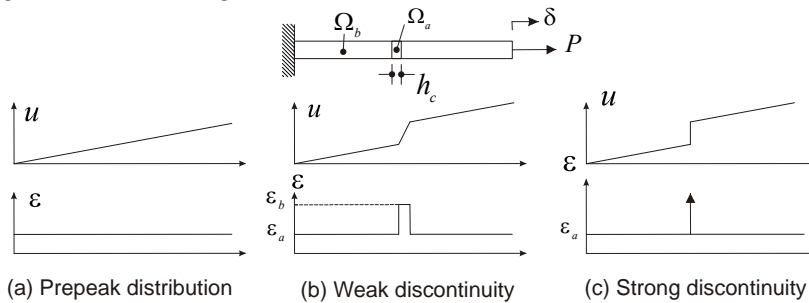
Figure 4.2. Bar with a strain softening material under axial stretching.

The bar of length L and cross section A has elastic behavior, which is defined by the elastic modulus E, up to the tensile strength σ_y. For simplicity, let us consider that the bar has a discrete number of segments which can be subjected to softening, while the remaining part of the bar stays elastic. The load versus horizontal displacement δ solutions considering 1, 2, 3, and 4 segments of the bar in softening are plotted in Figure 4.3. Depending on the

number of these segments, it can be obtained infinite solutions in the post peak branch. All these solutions satisfy the equilibrium, compatibility, and constitutive equations at any point of the domain, as also, in all boundary conditions.
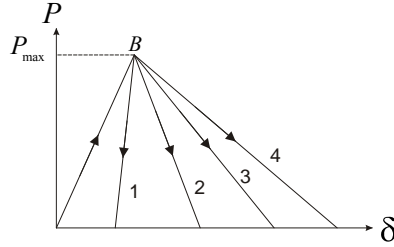
Figure 4.3. Stretching of a 1-D bar with different negative slopes.

We can assume, without loss of generality, that there is a narrow central band in the bar, Ω_a, with width, l_a, coinciding with one segment of the above mentioned discrete ones, which has a lower value of the tensile strength than the surrounding material Ω_b $\left(\sigma_y^a < \sigma_y^b\right)$. Therefore, the specimen exhibits a uniform strain distribution up to σ_y^a and after yielding, softening onsets in the band. Under the increase of prescribed displacement, the stress is the same for two different points inside and outside the band (Ω_a and Ω_b, respectively), due to equilibrium of stress, but the points undergo different strain levels ($\varepsilon_a \neq \varepsilon_b$). The material in the region Ω_a is under loading conditions, while the surrounding material (in Ω_b) is in un-loading condition. The zone, where strain concentration arises is known as *strain localization band* h_c.

The width of the localization band is a central issue in localization phenomena. When choosing a particular spatial discretization, one of these solutions is obtained. This strong dependence of the structural solution with the size of the localized band can be alleviated by reinterpreting the role of the continuum softening modulus, H, in the formulation of the constitutive model (Hernández 2008), as will be discussed in the following subsection.

4.1.3.   Definition of an intrinsic softening modulus

As commented above, constitutive equations considering strain softening induce strain loca-lization and non-objectivity with respect to the size of the finite element mesh. To overcome the problem and achieve objectivity, the constitutive law can be modified according with an energetic procedure. Let us consider the dissipated energy, W, which is divided by the cross section area of the bar, A. This term is denoted fracture energy G_f and can be considered, with good approximation, a constant material parameter. Then, from the bar test and taking a softening segment of length l_a, it could be found that:

$$G_f = \frac{W}{A} = \frac{1}{2}\frac{\sigma_y^2}{|H|}l_a.$$

(4.1)

where H represents the softening modulus of the material. This equation suggests that, by adopting the material parameter G_f, the softening parameter could be redefined as a function of energy and the localization bandwith l_a, as follows,

$$|H| = \left(\frac{1}{2} \frac{\sigma_y^2}{G_f} \right) l_a \Rightarrow |H| = |\bar{H}| l_a \qquad (4.2)$$

This so called "softening modulus regularization" allows overcoming the bandwidth dependence of the results commented above (Oliver 1989).

4.2.   Concrete fracture model

A realistic representation of the crack process would require some additional sophistication in terms of the model capturing the discontinuity. In a recent work of (Dias et al. 2011a), it was proposed the use of a localized strain injection via mixed formulations, in order to remove the flaws of the classical numerical methods to capture strain localization. The classical strain localization concept is brought to the approach, so that, no strong discontinuity enrichment is made and standard constitutive models are used in a classical strain localization settings. Then, in order to remove the spurious mesh orientation dependence, constants strain localization modes are injected, via mixed finite elements formulations (Dias et al. 2011b).

4.2.1.   Bifurcation analysis of the material composite

From the mechanical point of view, strain localization is connected with bifurcation and stability analysis. In fact, material instabilities are classically associated with the loss of ellipticity of the governing set of partial differential equations.

Let us consider the body in Figure 4.4, where the discontinuity of the displacement field occurs at the discontinuity line S. Restricting the analysis to small deformation settings, the development of a localized band entails the following kinematical condition

$$\dot{\boldsymbol{\varepsilon}}_S = \dot{\boldsymbol{\varepsilon}}_{\Omega/S} + \dot{\gamma} \left(\mathbf{m} \otimes \mathbf{n} \right)^s \qquad (4.3)$$

where $\dot{\boldsymbol{\varepsilon}}_S$ and $\dot{\boldsymbol{\varepsilon}}_{\Omega/S}$ are the symmetric strain rates inside and outside the band, respectively, $\mathbf{n}$ is the unit normal vector to the localized band and $\mathbf{m}$ is the vector defining the direction of the displacement jump. By equilibrium condition, the traction vector continuity across S must be imposed, yielding:

$$\dot{\mathbf{t}}^+ - \dot{\mathbf{t}}^- = \mathbf{0} \Rightarrow \mathbf{n} \cdot \left(\dot{\boldsymbol{\sigma}}_{\Omega/S} - \dot{\boldsymbol{\sigma}}_S \right) = \mathbf{0} \qquad (4.4)$$
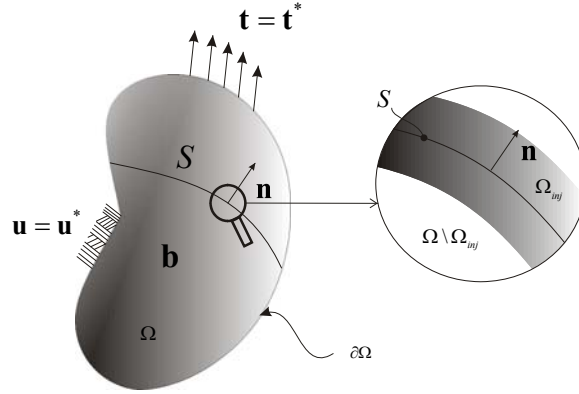
Figure 4.4.Discontinuity line S and injection zone Ω_{inj} . (Oliver et al. 2010a)

The constitutive response at localization is not necessarily continuous. This is the case of the *discontinuous bifurcation* (Rice & Rudnicki 1980). Using the constitutive equation defined in the expression (2.72), the following expression is obtained,

$$\left(\mathbf{n}\cdot\mathbb{C}^{tg}\left(t_{B}\right)\cdot\mathbf{n}\right)\cdot\mathbf{m}=\mathbf{0}, \tag{4.5}$$

which can be written in term of the localization tensor $\mathbb{Q}_{loc}=\mathbf{n}\cdot\mathbb{C}^{tg}\cdot\mathbf{n}$, as follows,

$$\mathbb{Q}_{loc}\left(t_{B},\mathbf{n}\right)\cdot\mathbf{m}=0. \tag{4.6}$$

Thus, equation (4.6) imposes the singularity of $\mathbb{Q}_{loc}$, or equivalently, the null value of one of its eigenvalues that is a necessary and sufficient condition for the material bifurcation at point $\mathbf{x}$ at time t_{B} (Oliver et al. 2010b). Therefore, a necessary condition for appearance of localization, for $\mathbf{n}$, is that

$$\det\left(\mathbb{Q}_{loc}\left(t_{B},\mathbf{n}\right)\right)=0. \tag{4.7}$$

This is known as Rice's criterion and it characterizes the onset of the bifurcation. Refreshing this equation in terms of the constitutive tensor $\mathbb{C}^{tg}$, in equation (2.72), yields,

$$\mathbb{Q}_{loc}=k_{m}\mathbb{Q}_{loc}^{m}+\sum_{i=1}^{nfib}k_{f}^{i}\left(\left(\mathbf{n}^{i}\cdot\mathbf{r}^{i}\right)^{2}\left(\mathbf{r}^{i}\otimes\mathbf{r}^{i}\right)E_{f}^{tg}\right). \tag{4.8}$$

where, $\mathbb{Q}_{loc}^{m}$ is the localization tensor of the matrix, which was presented in (Linero 2006) for the tensile/compressive damage model. The analytical solution of the bifurcation problem, for specific non-linear material models, has been an issue of great concern. However, the numerical resolution of the discontinuous material bifurcation problem can be solved in an effective and accurate way, using a numerical algorithm, based on the iterative resolution of a coupled eigenvalue problem in terms of the localization tensor. This algorithm was presented by Oliver et al (Oliver et al. 2010b).

4.2.2.   Injection domain

The structural strength of HPFRC composites is highly dependent on the crack evolution across the meso and macro-structure. The non-linear response displayed by this material takes place during the cement cracking stage and the complete response depends dramatically on the strong interaction between concrete cracks and the fiber-matrix bond slip mechanism, which model was presented in the previous chapter. Thus, besides considering the bond-slip mechanisms, it is necessary to account for the concrete crack phenomena to establish a satisfactory constitutive model of the composite material.

There have been numerous approaches in the literature for modeling concrete fracture problems. Some contributions in this field, following the strong discontinuity approach, are presented in Oliver et al. (Oliver et al. 2002), (Oliver & Huespe 2004b) and Sánchez et al. (P.J. Sánchez & Sonzogni). A book, with an up to date description of different techniques and models addressed to this problems, has been recently published by Hofstetter and Meschke (Hofstetter & Meschke 2011).

In order to remove the flaws of the classical strain localization methods (stress-locking and mesh bias dependence) an injection of constant strain localization modes into the finite element mesh discretizing the body was proposed (Oliver et al. 2010a). Likewise, the spurious mesh orientation dependence is partially alleviated. This additional strain mode is injected via a mixed finite element formulation.

4.2.3.   Strain injection techniques for computational modeling of material failure

Let us consider standard irreducible quadrilateral finite elements that will be termed as the underlying elements. In order to remove the well-known flaws of this classical element for capturing and simulating evolution of cracks, constant strain localization modes are injected to the path of elements that are going to capture the cracks. The technique is mathematically consistent and is based on an (assumed strain) mixed variational formulation. This procedure is adopted because it has been shown that mixed formulations, in general, have better abilities to capture and propagate localizations modes if compared to irreducible formulations. Even though, stress locking effects may still remain in mixed formulations. The next items describe in details the implementation of both procedures.

4.2.4.   Assumed strain mixed formulation: the injection domain

The material bifurcation analysis is based on the acoustic tensor singularity presented in equation (4.7), where $\mathbb{C}^{tg}\left(t_B\right)$ is the constitutive tangent tensor of the overall response given by equation (2.72). Equation (4.7) provides the bifurcation time t_B, as well as, the normal vector $\mathbf{n}$ to the possible crack surface.

After the criterion (4.7) has been satisfied in a given finite element, we equip the element with an assumed strain model that is formulated in the context of a mixed two-field $\left(u-\varepsilon\right)$ variational approach. In this case, the interpolated displacement field remains the same as that of the irreducible quadrilateral finite element model presented at the beginning of the

finite element formulation, see equations (3.4) to (3.7). While, the strain field, ε_m, is interpolated with functions taken from V_ε, where V_ε is the space of element-wise constant functions. Then, strains ε_m are associated with displacements through the following variational equation:

$$\int_\Omega \left(\varepsilon_m - \nabla^s \dot{u}\right) : \delta\varepsilon \, d\Omega = 0 \quad ; \quad \forall \delta\varepsilon \in V_\varepsilon \tag{4.9}$$

From where, the strain matrix (3.18)-a in the element e can be written as:

$$\left[\varepsilon_m\right]^e = \overline{B}^e q^e \quad ; \quad \overline{B}^e = \frac{1}{\Omega^e} \int_{\Omega^e} B^e \, d\Omega^e = 0 \tag{4.10}$$

and equation (3.19) is consequently evaluated by using the modified strain-displacement matrix $\overline{B}^e$ instead of B^e.

The variational equilibrium expression of the momentum of balance in Box 3.1, is rewritten as follows:

$$\int_\mathfrak{B} \hat{\sigma}\left(\varepsilon^e\right) : \delta\varepsilon \, dV - \int_\mathfrak{B} b \cdot \delta u \, dV - \int_{\Gamma_\sigma} t^* \cdot \delta u \, dS = 0 \quad ; \quad \forall \delta u \in V_0; \ \forall \delta u \in V_\varepsilon \tag{4.11}$$

and after replacing the interpolation of displacement and strain fields and changing the matrix B^e by: $\overline{B}^e$, this equation can be identically written to the expression in Box 3.2.

The domain where the constant strain mode is injected, is defined as the geometrical locus of the points satisfying:

$$\Omega_{inj}\left(t\right) := \left\{x \in \Omega \mid t \geq t_B\left(x\right); \dot{r}_m\left(x,t\right) > 0\right\} \tag{4.12}$$

where the last condition $\left(\dot{r}_m\left(x,t\right) > 0\right)$ means that the matrix component of the composite should be evolving in a loading condition.

4.3.   Strain injection methodology

This methodology presented by Dias et al. (Dias et al. 2011a) injects a constant strain mode by mean of a mixed finite element formulation. This injected mode is applied to the finite elements that are going to capture the crack. According to (Oliver et al. 2010a) the injection procedure requires the following steps, (i) Determination of the injection domain, and (ii) Injection of the specific deformation mode.

4.3.1.   Step 1. Determination of the injection domain.

The discontinuous bifurcation analysis is used to identify the onset and the propagation direction of the weak discontinuity. The time of the crack onset is associated with the bifurcation time t_{bif} at a given point of the material. Consequently, the bifurcation analysis should be performed at every time step, and for that, the localization tensor has to be computed in terms of the tangent constitutive operator $\mathbb{C}^{tg}\left(\mathbf{x}, t_B\right)$, which stems from the chosen constitu-

tive method. This analysis is carried out as the first step of the procedure summarized in Box 4.2. The problem consists of finding the bifurcation time t_{bif} corresponding to the instant that it is produced a non trivial solution for the normal to the weak discontinuity $\mathbf{n}$.

During this step is also defined the injection zone, this was defined in section 4.2.4 and corresponds to those in-loading bifurcated points. Into this region of the continuum, the specific strain mode will be applied in the second step.

4.3.2. Elemental constant strain mode

For the numerical implementation of the injection procedure, it was selected the four node quadrilateral element with four Gauss points (Figure 3.1-b) and with a central additional point. The bifurcation time is characterized in terms of the calculations in the central point. In the second step, as soon as a given finite element fulfills the condition described in Step 1, i.e. falls over the region of bifurcated elements, a constant strain mode is injected via a mixed $\mathbf{u}\text{-}\boldsymbol{\varepsilon}$ formulation as illustrated in Figure 4.5, where Ω_{mixed} is the injection domain. The use of the mixed formulation is motivated by the better performance of the mixed formulation compared to the irreducible standard one. In fact, as discussed in (Dias et al. 2011a) there exists a better kinematic flexibility deriving from the weakly enforcement of the compatibility equation and it exhibits remarkable properties for the correct propagation of the strain localization in initial stages.
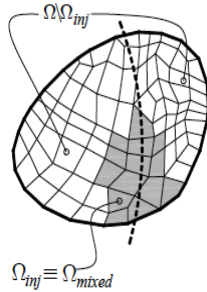
Figure 4.5.Discontinuity line S and injection zone Ω_{inj}. Adapted from (Dias 2012).

The injection of the constant strain mode is restricted to the injection domain Ω_{inj}; therefore, the variational boundary value problem in Box 3.1 is rewritten as follows,

$$\int_{\Omega \setminus \Omega_{inj}} \nabla^s \delta \mathbf{u} : \hat{\boldsymbol{\sigma}}\left(\nabla^s \mathbf{u}\right) dV + \sum_{e \in \Omega_{inj}} \int_{\Omega^{(e)}} \nabla^s \delta \mathbf{u} : \hat{\boldsymbol{\sigma}}\left(\overline{\nabla^s \mathbf{u}}^{e}\right) dV - \mathbf{F}_{ext} = 0 \quad \forall \delta \mathbf{u} \tag{4.13}$$

$$\int_{\Omega \backslash \Omega_{inj}} \left(\delta\beta^{(I)} \tilde{\tau}_f^{(I)}(\beta) - \frac{A^f}{\Pi^f} \left(\delta\beta^{(I)} \right)_{,r} \tilde{\sigma}_f^{(I)} \left(\varepsilon^f \right) \right) dV$$

$$+ \sum_{e \in \Omega_{inj}} \int_{\Omega \backslash \Omega_{inj}} \left(\delta\beta^{(I)} \tilde{\tau}_f^{(I)} \left(\overline{\beta} \right) - \frac{A^f}{\Pi^f} \left(\delta\beta^{(I)} \right)_{,r} \tilde{\sigma}_f^{(I)} \left(\overline{\varepsilon}^f \right) \right) dV = 0; \qquad (4.14)$$

$$\forall \delta\beta^{(I)} \in V_0^\beta; \quad \left(I = 1, \ldots, n_f \right)$$

where Ω_{inj} indicates the injection domain and $\Omega \backslash \Omega_{inj}$ indicates the remained domain. The values of the injections correspond to the solution of the weak form of the deformation compatibility. This reads as follows,

$$\int_{\Omega^{(e)}} \boldsymbol{\mu}^e : \left\{ \nabla^s \mathbf{u} - \overline{\boldsymbol{\varepsilon}}^e \right\} dV = 0 \qquad \forall e \in \Omega_{inj}$$

$$\int_{\Omega^{(e)}} \boldsymbol{\eta}^e : \left\{ \left(\boldsymbol{\varepsilon}^f \right)^e - \left(\overline{\boldsymbol{\varepsilon}}^f \right)^e \right\} dV = 0 \qquad \forall e \in \Omega_{inj} \qquad (4.15)$$

$$\int_{\Omega^{(e)}} \boldsymbol{\varphi}^e : \left\{ \beta^e - \overline{\beta}^e \right\} dV = 0 \qquad \forall e \in \Omega_{inj}$$

where $\boldsymbol{\mu}^e, \boldsymbol{\eta}^e$ and $\boldsymbol{\varphi}^e$ stand for the element-wise constant weighting function, $\overline{\boldsymbol{\varepsilon}}^e, \left(\overline{\boldsymbol{\varepsilon}^f} \right)^e$ and $\overline{\beta}^e$ are the element-wise constant injected strain. The substitution of these element-wise constant strain fields yields equations (4.24) and (4.25). The reader could observe that, the strain field $\overline{\nabla^s \mathbf{u}}^e$, $\overline{\varepsilon^f}^e$ and $\overline{\beta}^e$ are injected in the elements that belong to the injection zone Ω_{inj}. For simplicity in the notation, we will express $\overline{\boldsymbol{\sigma}}^e = \hat{\boldsymbol{\sigma}} \left(\overline{\nabla^s \mathbf{u}}^e \right)$, $\left(\overline{\sigma}^f \right)^e = \tilde{\sigma}^f \left(\overline{\varepsilon}^f \right)$ and $\left(\overline{\tau}^f \right)^e = \tilde{\tau}^f \left(\overline{\beta} \right)$ as the stress fields associated with the injected constant strain fields.

4.3.3. Step 2. Injection of elemental constant strain mode

In the work of (Dias et al. 2011a), the equilibrium equations were presented in rate form, which is used in the implementation of the continuum with microstructure based model developed as well. This is convenient to avoid sudden changes in the total stiffness. The incremental strategy is based in evaluation of the increment of the total stress as follows:

$$\Delta \hat{\boldsymbol{\sigma}}_{n+1}^e = (1-\gamma) \left(\overline{\boldsymbol{\sigma}}_{n+1}^e - \overline{\boldsymbol{\sigma}}_n^e \right) + \gamma \left(\boldsymbol{\sigma}_{n+1}^e - \boldsymbol{\sigma}_n^e \right),$$

$$\Delta \hat{\boldsymbol{\sigma}}_{n+1}^e = (1-\gamma) \Delta \overline{\boldsymbol{\sigma}}_{n+1}^e + \gamma \Delta \boldsymbol{\sigma}_{n+1}^e . \qquad (4.16)$$

For the axial fiber stress, it is obtained by

$$\Delta \left(\tilde{\sigma}_f^{(I)} \right)_{n+1}^e = (1-\gamma^e) \left(\overline{\left(\tilde{\sigma}_f^{(I)} \right)}_{n+1}^e - \overline{\left(\tilde{\sigma}_f^{(I)} \right)}_n^e \right) + \gamma^e \left(\left(\tilde{\sigma}_f^{(I)} \right)_{n+1}^e - \left(\tilde{\sigma}_f^{(I)} \right)_n^e \right),$$

$$\Delta \left(\tilde{\sigma}_f^{(I)} \right)_{n+1}^e = (1-\gamma^e) \Delta \overline{\left(\tilde{\sigma}_f^{(I)} \right)}_{n+1}^e + \gamma^e \Delta \left(\tilde{\sigma}_f^{(I)} \right)_{n+1}^e . \qquad (4.17)$$

$$\text{where:} \qquad \begin{array}{l} \gamma^e = 0.0 \quad \forall e \in \Omega_{inj} \\ \gamma^e = 1.0 \quad \forall e \in \Omega \backslash \Omega_{inj} \end{array}$$

and the increment of the interfacial stress is

$$\Delta\left(\tilde{\tau}_f^{(I)}\right)_{n+1}^e = \left(1-\gamma^e\right)\left(\overline{\left(\tilde{\tau}_f^{(I)}\right)}_{n+1}^e - \overline{\left(\tilde{\tau}_f^{(I)}\right)}_{n}^e\right) + \gamma^e\left(\left(\tilde{\tau}_f^{(I)}\right)_{n+1}^e - \left(\tilde{\tau}_f^{(I)}\right)_{n}^e\right)$$

$$\Delta\left(\tilde{\tau}_f^{(I)}\right)_{n+1}^e = \left(1-\gamma^e\right)\Delta\overline{\left(\tilde{\tau}_f^{(I)}\right)}_{n+1}^e + \gamma^e\Delta\left(\tilde{\tau}_f^{(I)}\right)_{n+1}^e$$

(4.18)

Box 4.1 summarizes the incremental strategy, in which the incremental values of the stresses (4.16) to (4.18) are substituted. The procedure in Box 4.1 is applicable to the monolithic integration scheme described in subsection 3.5.1 and the procedure of Box 4.2 is applicable for the staggered integration one.

Injection of the constant strain $\overline{\mathbf{\varepsilon}}^{(e)} = \overline{\nabla^s\mathbf{u}}^{(e)}$ in the matrix

$$\underset{e\in\Omega}{\Lambda}\int_{\Omega^e}\nabla^s\delta\mathbf{u} : \hat{\mathbf{\sigma}}_{n+1}^e dV - \mathbf{F}_{ext} = 0, \quad \forall\delta\mathbf{u}$$

$$\hat{\mathbf{\sigma}}_{n+1}^e = \hat{\mathbf{\sigma}}_n^e + \Delta\hat{\mathbf{\sigma}}_{n+1}^e$$

(4.19)

Injection of the constant strain and slip in the fiber and the interface

$$\underset{e\in\Omega}{\Lambda}\int_{\Omega^e}\left(\delta\beta^{(I)}\left(\tilde{\tau}_f^{(I)}\right)_{n+1}^e - \frac{A^f}{\Pi^f}\left(\delta\beta^{(I)}\right)_{,r}\left(\tilde{\sigma}_f^{(I)}\right)_{n+1}^e\right)dV = 0; \quad \dots$$

$$\forall\delta\beta^{(I)}\in V_0^\beta; \quad \left(I=1,\dots,n_f\right)$$

(4.20)

Injection of the constant slip in the interface $\beta^e = \overline{\beta}^e$

$$\left(\tilde{\tau}_f^{(I)}\right)_{n+1}^e = \left(\tilde{\tau}_f^{(I)}\right)_n^e + \Delta\left(\tilde{\tau}_f^{(I)}\right)_{n+1}^e$$

(4.21)

Injection of the constant strain in the fiber $\left(\varepsilon^f\right)^e = \overline{\varepsilon^f}^{(e)}$

$$\left(\tilde{\sigma}_f^{(I)}\right)_{n+1}^e = \left(\tilde{\sigma}_f^{(I)}\right)_{n+1}^e + \Delta\left(\tilde{\sigma}_f^{(I)}\right)_n^e$$

(4.22)

Box 4.1. Injection methodology in incremental form for the monolithic integration scheme.

Step 1   Find t_{bif}

Such that:

$$Q\big(n(x),t_B\big) = n \cdot \mathbb{C}\big(x,t_B\big) \cdot n \tag{4.23}$$

$$\det Q\big(x,t_B\big) = 0$$

Step 2   Partition $i_{partition} = 1$, injection of the elemental constant mode

$$\int_{\Omega \backslash \Omega_{inj}} \nabla^s \delta u : \hat{\sigma}\big(\nabla^s u\big) dV + \sum_{e \in \Omega_{inj}} \int_{\Omega^{(e)}} \nabla^s \delta u : \hat{\sigma}\bigg(\overline{\nabla^s u}^{(e)}\bigg) dV - F_{ext} = 0 \tag{4.24}$$

Partition $i_{partition} = 2 \ldots n_{partition}$, injection of the elemental constant mode

$$\int_{\mathfrak{B} \backslash \mathfrak{B}_{inj}} \left(\delta\beta^{(I)} \tilde{\tau}_f^{(I)}(\beta) - \frac{A^f}{\Pi^f}\big(\delta\beta^{(I)}\big)_{,r} \tilde{\sigma}_f^{(I)}\big(\varepsilon^f\big) \right) dV + \cdots$$

$$\sum_{e \in \mathfrak{B}_{inj}} \int_{\mathfrak{B} \backslash \mathfrak{B}_{inj}} \left(\delta\beta^{(I)} \tilde{\tau}_f^{(I)}\big(\overline{\beta}\big) - \frac{A^f}{\Pi^f}\big(\delta\beta^{(I)}\big)_{,r} \tilde{\sigma}_f^{(I)}\big(\overline{\varepsilon}^f\big) \right) dV = 0; \ldots \tag{4.25}$$

$$\forall \delta\beta^{(I)} \in V_0^\beta; \quad \big(I = 1,\ldots,n_f\big)$$

Box 4.2. Injection procedure in incremental form for staggered scheme.

Chapter 5
Representative numerical simulations

5.1.   Introduction

The fundamental equations, the numerical components of the algorithm and the additional techniques required for the numerical simulation of the mechanical behavior of the HPFRC composites have been presented in the preceding chapters. Following the framework of the continua with microstructure, a model has been introduced to represent the mechanical behavior of the HPFRC composite, which incorporates two substructural actions: the fiber axial stress and the fiber-matrix interface debonding. So far, the set of governing equations in strong form, the corresponding weak form and the variational ones were deduced. They were appropriately implemented in an in-house finite element code in order to reproduce experimental tests. In order to ascertain the suitability of the proposed formulation on describing the structural composite response, a selected set of experimental results is taken from literature. Elastic, hardening and localization stages are examined. The main concern in this chapter is to examine the model predictive ability. The aim is to find suitable experimental results and compare them with the results obtained from simulations, with a view towards validating the present model.

Tests used to monitor and characterize the entire mechanical behavior of HPFRC composites are: 1) the direct uniaxial test, 2) the wedge-splitting test and 3) the bending test. Post-cracking behavior properties (e.g. flexural toughness, energy absorption capacity, and fracture mechanisms) can be estimated by using the results of these tests. Nevertheless, in the practice, to measure the toughness, the flexural test is commonly used, because it reproduces more realistically the conditions occurring in many real situations and, additionally, it is simpler to conduct than the tensile test.

Several factors contribute to improve ductility and toughness of concrete. As mentioned throughout this monography, a variety of fracture process mechanisms associated with the presence of fibers operates to produce changes in the composite properties. In brittle matrix/ductile-fiber-reinforced composite systems, such as cement matrix/steel-short-fiber, the interface could control the cracking propagation and the subsequent failure. The continuum with microstructure-based approach for the HPFRC composites, proposed in this research, aim at reproducing two relevant and influential mechanisms, namely, the fiber pullout phenomenon and the subsequently fiber plastification. In order to show these model features, some tests are particularly addressed in the following sections.

Physical observations show that failure patterns of HPFRC composite depend upon the distribution of the fiber, the fiber contents and the type of fiber within the specimen. By numerical simulation, we want to verify the validity of this assertion by using the proposed model. For this, comparison between the simulated and experimental crack patterns will be carried out, expecting that the model might replicate the microcracking pattern, prior to strain localization, as well as the strain localization representing the macrocracks.

5.2.   Test 1: Notched strip under uniaxial loading.

Numerical evaluation of a small specimen, such as shown in Figure 5.1, is taken into account to examine several features of the model. We consider the specimen subjected to a simple unidirectional uniaxial load. In this simple case, the imposition of a uniform stress state is a key element in the determination of the stiffness and strength characteristics of the concrete composite. The presence of the microfibers introduces coupled effects between actions in the mesoscale and the macroscale, which we aim at analyzing in this section.
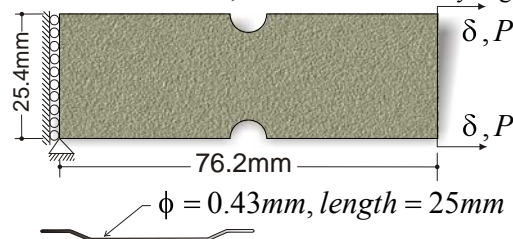
Figure 5.1. Set-up of notched strip under uniaxial loading test.

The notched strip is clamped at its left end and pulled at the right end. The notches are situated in the middle of the specimen to ensure damage localization in this area. The region of concern is the area close to the notches, where the pullout process is expected. This example addresses three main issues: 1) the pullout behavior of the specimen with aligned fibers respect to the loading condition, 2) the pullout behavior of the specimen with inclined fibers and 3) the effect that the finite element formulation has on the mechanical response, confining our attention principally to effects on capturing the strain localization phenomena.

5.2.1.   Pullout behavior of a specimen with aligned steel fibers

In order to investigate the sensitivity of the proposed model to the bond shear strength properties, the simplest case of aligned fibers respect to the loading direction is considered. Numerical simulations with identical mechanical and geometrical characteristics are carried out, but varying the bonding properties of the fiber-matrix interface. The set of parameters is summarized in Box 5.1. Note that six different ultimate bond shear stress values are adopted and only one bundle fiber, longitudinal oriented, is considered. This fiber bundle is horizontally oriented.

Matrix	Fiber	Interface zone
$f_c' = 2.0 MPa$	$\sigma_u^f = 210 MPa$	$\tau_u^f = 1e-3, 0.1, \ldots$ $0.6, 1, 5, 50 MPa$
$E^m = 15 GPa$	$E^f = 200 GPa$	$E^d = 1e+8 GPa$
$\upsilon^m = 0.2$	$H^f = 0 MPa$	$H^d = 100 MPa$
$G_f = 100\, N/m$	$\theta = 0°$	$V_f^0 = 0.5\%$

Box 5.1. Mechanical properties of the compounds in the notched strip under uniaxial loading test.

From experiments, we recall that the HPFRC composite response in tension shows three stages: linear elastic (which ends once the first point of the structure begins the cracking process), multicracking or hardening stage (which ends at structural peak load), and a final localization stage. Also in order to discuss the results, it is important to recall that the main difference in the tensile load-displacement response between the HPFRC composite and conventional FRC is the multicracking stage, which may not exist in the conventional FRC.

Figure 5.2 compares the load versus displacement response of the composite material for the selected set of values of the ultimate bond shear stress τ_Γ^u. These numerical results show that the load-displacement curve can generally be subdivided in two different behaviors: ascending and descending branches. The ascending behavior consists, as we will explain later, of perfectly bonded state between fibers and matrix and partially debonded state. Then, the hardening behavior is related to the fiber-matrix debonding process.

The numerical results show, as expected, brittle behavior of the plain material. The response for the smallest value of the ultimate bond shear stress ($\tau_u^f = 1e-3 Mpa$) considered in this example, closely resembles the curve reached by the plain concrete case. After crossing the peak load, the material softens almost in a brittle mode. The absence of hardening stage can be caused by rapid loss of bonding strength.
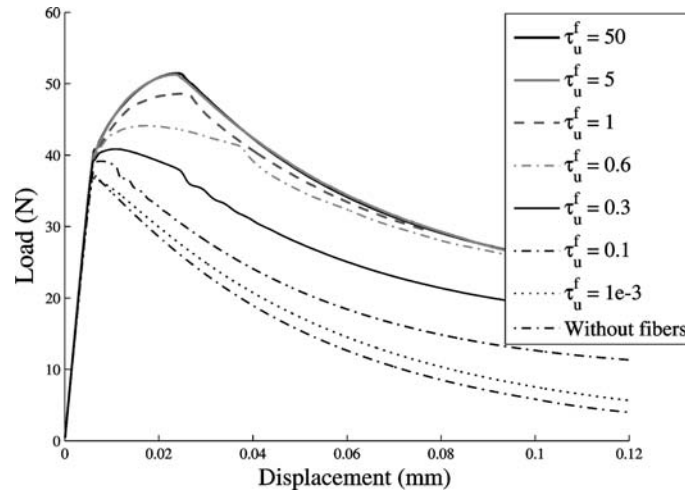
Figure 5.2. Notched strip under uniaxial loading test: Comparison between different load P
versus displacement curves at different ultimate bond shear stresses.

The load displacement curves for other values of τ_u^f, display a hardening response, as also, higher values of the peak load as the τ_u^f value increases. The increase of the bond strength, τ_u^f, leads to a direct increase of the postcracking strength, toughness and energy absorption capacity. The higher the value of τ_u^f, the larger the hardening stage. However, if the value of the ultimate bond shear strength exceeds $\tau_u^f = 5MPa$, the response of the material does not vary significantly. As the value of the bond strength beyond $5MPa$ the mechanical behavior is not altered and we could assert, for this particular case, that this value represents a limit.

The final damage distributions observed in the matrix, for different cases of τ_u^f, are depicted by means of iso-color maps in Figure 5.3. For plain concrete limit, the damage distribution in Figure 5.3 (a) shows damage concentration around the notch. As τ_u^f increases, according with Figure 5.3 (b-f), the zone affected by damage grows, suggesting that more fibers develop pullout forces and, in consequence, the material toughness increases.

For the identical time steps, sequential portraits of fiber yielding, matrix damage and debonding of the matrix-fiber interface distributions can be superimposed to visualize the failure characteristics of each compound. The analysis of the microstructural level reveals various failure mechanisms whose synergistic interaction accounts for the larger strength and higher toughness properties. The analysis is undertaken with three values of $\tau_u^f \left[1e-3, 0.6, 50MPa\right]$. We classify these three cases, depending on the debonding failure mechanisms, as fully debonded, partially debonded and fully bonded

(a)Without fibers	(b) $\tau_u^f = 1e-3$	(c) $\tau_u^f = 0.1$	(d) $\tau_u^f = 0.6$

(d) $\tau_u^f = 1$	(e) $\tau_u^f = 5$	(f) $\tau_u^f = 50$
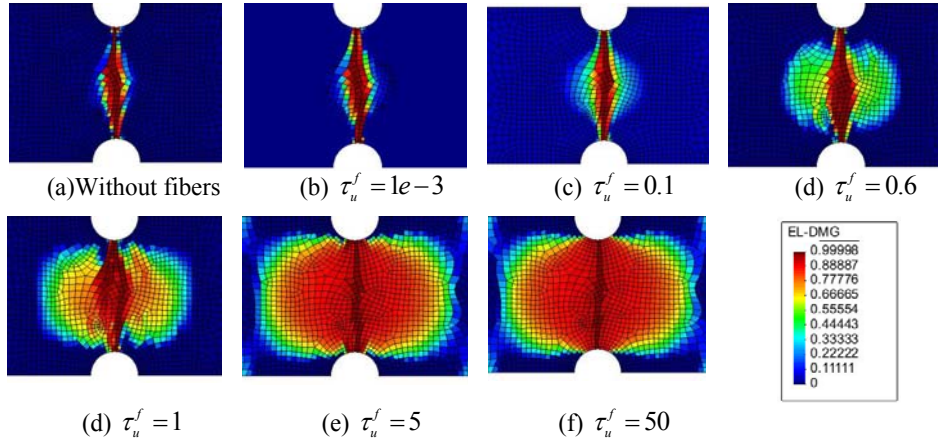
Figure 5.3. Set-up of notched strip under uniaxial loading test. Iso-color maps indicating the damage distribution of cement matrix with different matrix-fiber bond strength parameters.

.

5.2.1.1. Fully debonded case

Weak interfaces between fiber and matrix are generally associated to a low fracture toughness of the composite. In the composite, a weak interface produces poor stress transfer abilities between matrix and fibers and, therefore, fibers are not fully utilized. According to the results in Figure 5.2, low ductility can be associated with $\tau_u^f = 1.0e-3MPa$. This value can be considered as a weak interface. Under tensile loads, the model shows a sudden de-bonding in the whole domain, as it is observed in the debonding distribution of Figure 5.4 and consequently, deactivation of the composite effect. In this case, we verify that for enough small values of the ultimate bond strength, the model is able to represent weak fiber-matrix interfaces. In fact, this is a consequence of the Capriz balance equation, which go-verns the microstructural behavior. When using $\tau_u^f \approx 0.0$, the fiber bond strain also ap-proaches to zero and, therefore, the fiber is pulled out immediately after the load is applied. This also implies that the slip can take any value, when the bond strength is exhausted. Cer-tainly, the value of the slip is of the same order of the x-displacement, as shown in Figure 5.5(b), where the slip and x-displacement are plotted along the length of the strip in different stages of the loading curve as indicated in Figure 5.5(a). The concentration of the damage in the notched section is due to the inability of the fiber-matrix interface to transfer the stresses. Figure 5.4 illustrates the plasticity, damage and debonding in the specimen. For the plasticity and debonding, the darker blue color represents that the element is in elastic regime and the darker red color indicates that the element is in inelastic loading one. In accordance with the damage and debonding results (Figure 5.4), small axial strain in the fibers is developed due to the sudden debonding and consequently yielding is not achieved, as confirmed in the plas-ticity distribution.

Figure 5.4. Results for $\tau_u^f = 1.0e - 3MPa$. Portraits of plasticity in the fiber, debonding in the IZ and damage in the matrix in the end of the load-displacement curve. For plasticity and debonding, darker blue indicates elements in elastic regime and darker red, elements in inelastic regime.
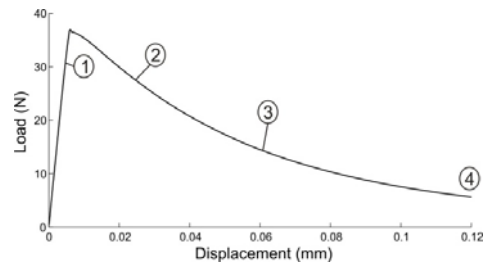
(a)
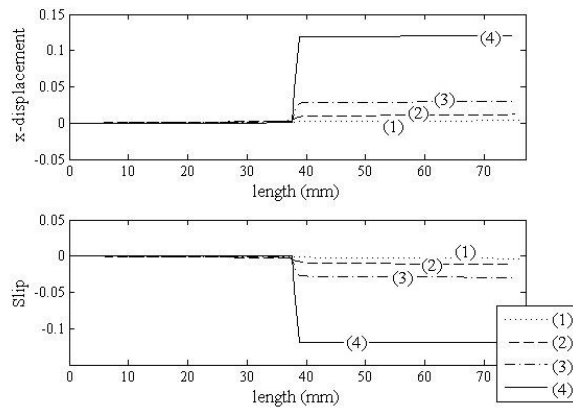
(b)

Figure 5.5. (a) Load-displacement curve for $\tau_u^f = 1.0e - 3MPa$. (b) Evolution of the slip and the x-displacement in the middle section of the strip for the stages in (a) marked with the numbers from 1 to 4 in the load vs. displacement curve.

5.2.1.2. Partially debonded case

Steel fibers possess some kind of bonding properties resulting from chemical reactions during cement hydration or from mechanical anchorage. If this chemical or mechanical adhesion is not very strong, the scenario presented during the fracture process encompasses a lot of possible situations, in which the combination of the micro-mechanisms is addressed by the fiber matrix interface properties. Then, we could say that the material behavior is characterized by partial debonding. In the case simulated with $\tau_u^f = 0.6 MPa$, which in accordance with the Figure 5.2 displays semi-ductile behavior, represents a partially debonded example. The results obtained in this case are shown in two different instants indicated in Figure 5.6: The first instant represents a stage during the initial softening process. The second instant represents a stage at the end of the localization process.
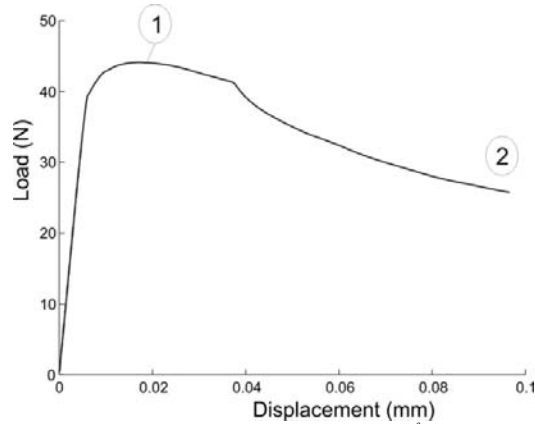
Figure 5.6. Load vs displacement curve for $\tau_u^f = 0.6 MPa$.

The assumed perfect plastic material behavior adopted for the matrix-fiber bond shear-slip relationship gives rise to slip when the ultimate bond shear strength is reached, and subsequently the shear deformation is increased. In the first considered instant (Figure 5.7 (a)), it is noticeable that fiber-matrix interface debonding evolves as a consequence of the increase in the slip. Fiber-matrix interface debonding and matrix damage may be triggered because of their weakness to resist shear stresses. This behavior indicates that the matrix damage and sliding frictional resistance of fiber pullout largely determine the composite toughness and the hardening properties (Beyerlein & Phoenix 1996). Inspection of the plots for damage and plasticity in Figure 5.7 (b) (second stage) indicates that the crack opening in the notch, due to cumulative damage, is accompanied with loss of adhesive bond in the matrix-fiber interface and plastic strain in fibers. Not surprisingly, only few more points in the specimen achieve the ultimate bond shear strength when the final state is reached and the debonding distribution scarcely changes, as indicated in Figure 5.7.
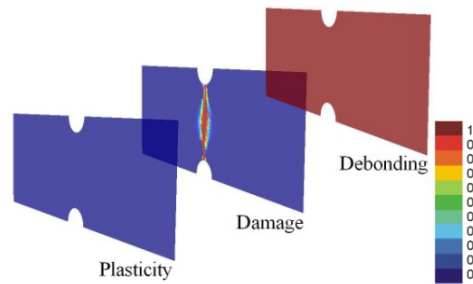
Figure 5.7. Results for $\tau_u^f = 0.6 MPa$. Portraits of plasticity in the fiber, debonding in the IZ and damage in the matrix in the end of the load-displacement curve. (a) Instant (1) (depicted in Figure 5.6) during the hardening process. (b) Instant (2) (depicted in Figure 5.6) during in the end of the loading process.

5.2.1.3. Fully bonded case

High adhesive interfaces can be achieved by improving, at microstructural level, the properties of fiber surface. However, a strong interface may result in lower toughness, because this effect does not allow interfacial debonding, which is one of the main mechanisms to relieve stress concentrations produced by the oncoming crack (Jiang et al. 2000). With a view towards investigating this possibility, simulations were performed for $\tau_u^f = 5.0 MPa$ and $\tau_u^f = 50.0 MPa$.

Observing the load displacement curves for $\tau_u^f = 5.0 MPa$ and $\tau_u^f = 50.0 MPa$ in Figure 5.2, they suggest that for high values of τ_u^f, the model predicts similar structural responses. The reason of this behavior is not clear. Even more remarkable is the fact that plasticity and damage exhibit similar distribution patterns as the end of the loading process. It seems reasonable to propose, based on these results, that in both situations, the dominant failure mesomechanism at the mesoscale is the fiber plasticity. Although the debonding distribution is distinctively different, this effect does not seem to affect significantly the structural response.

Experimental results corroborate that if the fiber matrix interface strength is much higher than the matrix strength in shear, then, the matrix damage will occur instead of fiber matrix debonding. This experimental fact is also supported through numerical simulation by observing results for $\tau_u^f = 50.0 MPa$ in Figure 5.8. Although the matrix multicracking is much more significant in this case, fibers plastic deformation occurs in the path of the critical crack. In summary, the pullout process, and in consequence the failure mechanism for high adhesives interfaces, involve essentially matrix damage and plasticity.

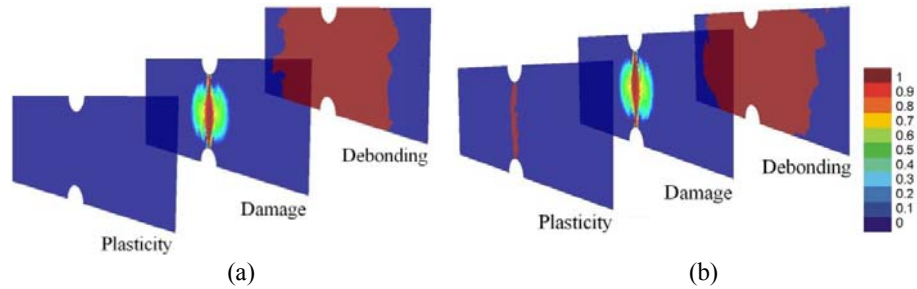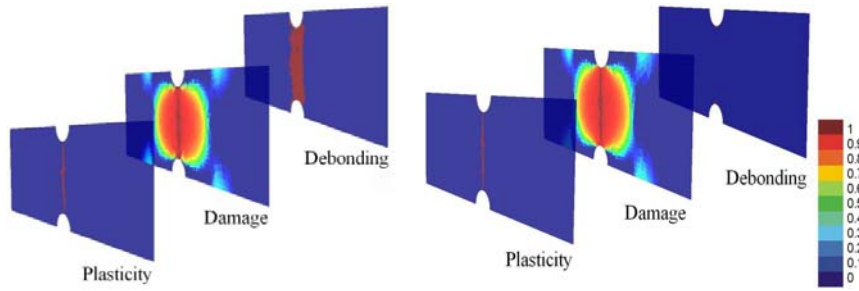Figure 5.8. Results for $\tau_u^f = 5.0MPa$ and $\tau_u^f = 50.0MPa$. Portraits of plasticity in the fiber, debonding in the IZ and damage in the matrix in the end of the load-displacement curve. (a) Instant in the end of the loading process for $\tau_u^f = 5.0MPa$. (b) Instant in the end of the loading process $\tau_u^f = 50.0MPa$.

5.2.2. Assessment of the crack prediction considering different finite element formulations

In order to analyze the role played by the element formulation during the localization process, the reinforced concrete notched strip under uniaxial tensile stress of section 1.2 and shown in Figure 5.1, is discretized by using three different element formulations. The mechanical properties of the components are summarized in Box 5.2.

Matrix	Fiber	Debonding
$f_c' = 2.0MPa$	$\sigma_u^f = 210MPa$	$\tau_u^f = 5.0MPa$
$E^m = 15GPa$	$E^f = 200GPa$	$E^d = 1e + 8GPa$
$\upsilon^m = 0.2$	$H^f = 0MPa$	$H^d = 100MPa$
$G_f = 100\,N/m$	$\theta = 0°, 45°$	$V_f^0 = 0.5\%, V_f^{45} = 0.5\%$

Box 5.2. Compound mechanical properties notched strip under uniaxial loading test.

Two families of fibers oriented at 0° and 45° respect to the loading direction are considered. Three finite element formulations are contemplated: i) the standard triangular, ii) the standard quadrilateral element and iii) the injection of an elemental constant strain mode in the quadrilateral element. In the preliminary study presented by (Dias et al. 2011a), the effectiveness of the localized strain injection was assessed in capturing strain localization in simple material. We demonstrate in the example that the formulation, based on strain injection, provides results which are mesh independent also in the simulation of composite materials.

The load vs displacement curves, for the three numerical alternatives are compared in Figure 5.9. Loading of the strip in tension causes damage in the matrix and subsequently hardening due to the pull out effect of the fibers. It may be noted that the homogenization method for which the rule of mixtures, also known as Taylor assumption, is considered, has the ability to incorporate ductility due to the combined effects of the materials. Hence, the load does not drop abruptly as in tensile test of simple concrete. It is apparent in the plot that the numerical results prior the peak load, does not seem to be influenced by the element formulation. Conversely, it is noted that the post peak response is affected by the finite element approach. This fact is evident in the iso displacement plots presented in Figure 5.10.
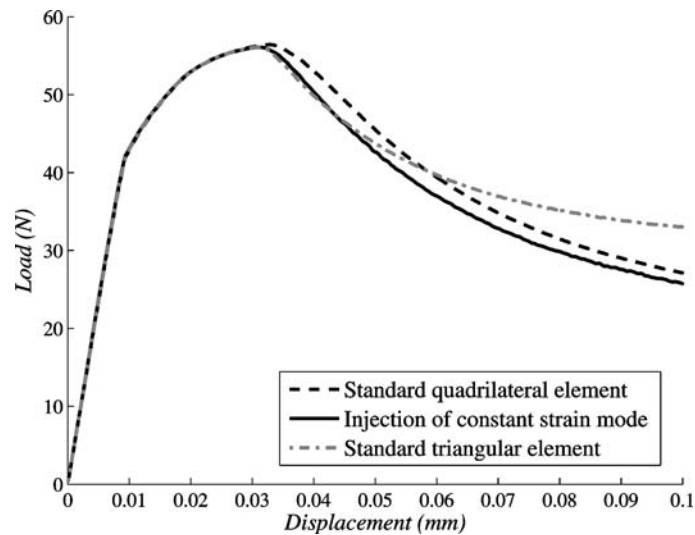
Figure 5.9. Load as a function of displacement of a fiber reinforced cement strip under uniaxial tensile stress state for the three different approaches.

Figure 5.9 (a-c) shows iso-displacement contours representing the strain localization patterns, corresponding to each of the alternatives. The stress locking is not very noticeable in Figure 5.9. However, in Figure 5.10, it can be noted that the triangular approach exhibits stress-locking (spurious stress transfer across a widely open crack), which is caused by a poor kinematical representation of the discontinuous displacement field around the macroscopic crack in the central part of the specimen. Alternatively, the quadrilateral element does not display this deficient response. Even more, the quadrilateral element with the injection of a constant mode on the same element exhibits an improvement respect to the triangular formulation.

(a)   (b)   (c)
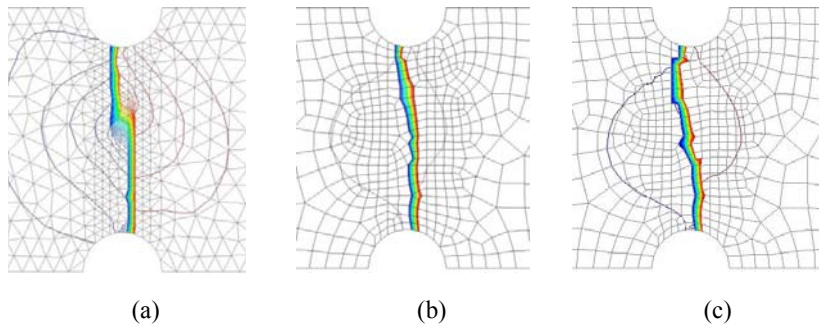
Figure 5.10. Localization patterns depicted through iso-displacement curves with different approaches for the notched strip under uniaxial tensile, (a) triangular elements (b) standard quadrilateral elements (c) injection of a constant strain mode.

Application of the strain injection methodology requires the solution of the discontinuous material bifurcation problem, proceeding the time for the weak discontinuity onset, in order to determine the injection domain. The evolution of the injection domain is depicted in Figure 5.11, along different times of analysis. It can be observed the progress of the injection domain (defined in eq. (3.15)); the bifurcated elements are injected with a constant strain mode while they remain in loading. As soon as a finite element is detected to belong to the injection domain, it is approached with a constant strain field. During the initial injection stage (t = 1,2), the material bifurcation is detected in those elements close to the notch. In posterior stages, (t = 3, 4), soon later, most of the bifurcated elements unload, leave the injection domain and recover the standard formulation. In the final stage, (t=6), only a single band is further injected, where strain remains localizing.

t_1 t_2 t_3

t_4 t_5 t_6
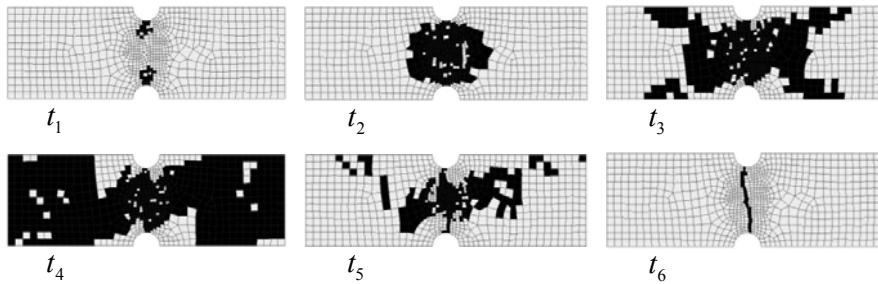
Figure 5.11. Evolution of the injection domain for different times of the analysis. Injected finite elements are depicted in black.

5.3.   Test 2: Beam with horizontally oriented fibers

We consider now, the test reported by Jiang and co-workers (Jiang et al. 2000). The four-point bending test evaluates the feasibility of using bone-shaped short BSS steel wires for improving the toughness in concrete. The test was motivated from experimental observation on (BSS) fibers composites, made of glass, polymer, and steel, which reveled a substantially higher toughness, and more crack resistance than conventional straight short (CSS) steel–wire-reinforced cement. From experimental results, they observed that problems, in short fiber composites, have largely to do with the fiber-matrix interface. Particularly, for a short fiber, a strong interface is desired to effectively transfer the load from matrix to fiber. On the other hand, for ductile BSS fiber reinforced composites, a weak interface can reduce significantly stress concentration and the toughness will improve since the fibers can effectively bridge cracks without premature fracture. With this information in hand, the test was addressed to simultaneously improve both the strength and the toughness of short-fiber composites by modifying the geometry of short fibers instead of the fiber/matrix interface.

From the experimental point of view, there are considerable difficulties to manufacture a unidirectional specimen with short fibers; however, it is advantageous in judging the results. Therefore, this example, although simple, is ideal and may bring us a step closer to understanding of crack initiation and propagation phenomena in cement composites.

5.3.1.   Specimen description

Three types of four-point bending test specimens were manufactured: i) unreinforced cement, ii) CSS-steel-wire-reinforced cement, and iii) BSS-steel-wire-reinforced cement. The reinforcement wires are commercial grade utility steel with yield strength of 260 MPa, and a failure strain of 12.6%. Both, BSS wires and CSS short wires, have a diameter of 0.84 mm and a length of 25 mm. The BSS steel wires have been obtained by cutting the wire into a length of 28 mm, and then, melting both ends with a torch, resulting in enlarged wire ends with an average diameter of 1.6 mm (see Figure 5.12 (a) and (c)). The properties indicated in Box 5.3 are kept constant for the simulation of the specimens, except for the value of the volumetric fraction of fibers, selected as 0.86% and 1% for the CSS- and BSS-wire-reinforced specimen, respectively. The template used for manually laying the steel wires is depicted schematically in Figure 5.12 (c).

The mesh, assuming a 2-D plane stress model, is made of triangular elements, with three degrees of freedom at each node (associated to the fields u_x, u_y, β respectively). It is shown in Figure 5.12(b). In the absence of experimental estimations of the ultimate bond stress value τ_u^f, for this specific case, the purpose of the simulation is to find a value, such that, it satisfactorily predict the mechanical composite response. Therefore, tuning of the fiber-matrix interface ultimate bond strength parameter is needed to achieve the best fit. In this respect and based on our experience with the model, the range of values $\tau_u^f \in [0, 7.5MPa]$, should be enough.
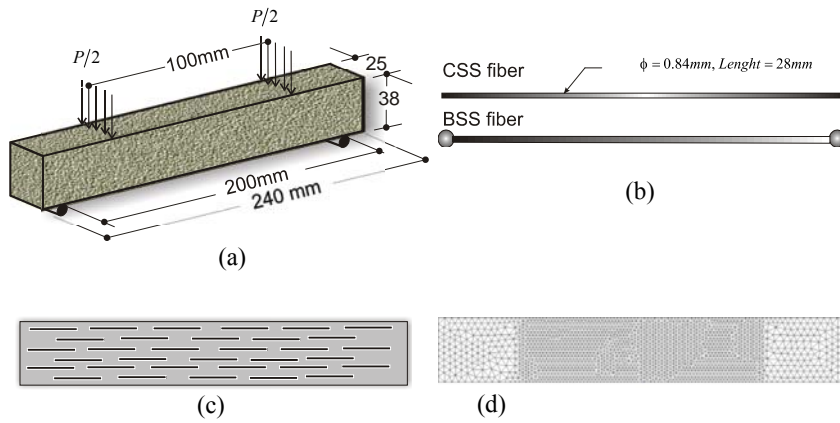
Figure 5.12. Schematic illustration of the four point bending test. (a)Set-up of bending test (Jiang et al. 2000). (b) Fiber geometries. (c) Fiber layout. (d) Finite element mesh

Matrix	Fiber	Interface zone
$f_c' = 4.0 MPa$	$\sigma_u^f = 260 MPa$	$\tau_u^f \in [0, 7.5 MPa]$
$E^m = 21 GPa$	$E^f = 180 GPa$	$E^d = 1e+8 GPa$
$\upsilon^m = 0.2$	$H^f = 700 MPa$	$H^d = 100 MPa$
$G_f = 100 N/m$	$\theta = 0°$ $\phi_f = 0.84$	$V_f = 0.86\%$

Box 5.3. Bending test: mechanical properties of each compound.

In our model, the geometry of fiber ends is not explicitly considered as a user defined parameter in the micro-model, but translated to the numerical model through an increase of the fiber matrix bond strength.

5.3.2.   Influence of the ultimate bond shear strength on the flexural response of the HPFRC composite

For different values of ultimate bond shear strength τ_u^f, the application of the model produces the numerical results as indicated in Figure 5.13. It compares the load P versus cross-head displacement response during the test for the reinforced CSS- and BSS-wire-reinforced specimens along with the numerical results for the values of τ_u^f considered. Typically, the beam performance is governed mainly by the combined contribution of fiber and matrix

during the ascending elastic branch of the equilibrium curve. Note that, however, after the first crack initiation (or deviation from linearity), the micromechanics dominate the mechanical response and different values of the ultimate bond strength trigger two clearly distinct types of failure processes: (1) deflection-softening and (2) deflection-hardening.
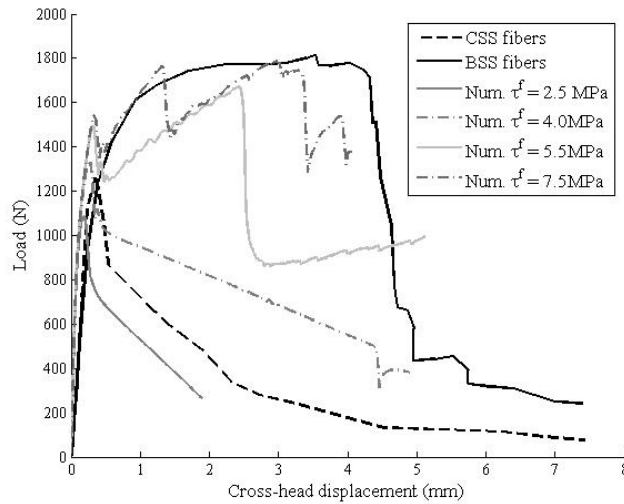
Figure 5.13. Beam test. Load as a function of cross head displacement steel-wire-reinforced cement specimens.

By comparing the experimental results with the simulated ones, as shown Figure 5.13, the BSS-wire reinforced specimen and the numerical response for $\tau_u^f = 7.5MPa$ are in good agreement, as also, CSS-wire reinforced test result and the curve for $\tau_u^f = 2.5MPa$. This preliminary comparison is an attempt to recognize the possible values that the ultimate bond strength parameter could take for this example. Moreover, further inspection of the crack pattern prompts this conjecture.

The iso-displacement contours in Figure 5.14 (a-d) show the crack patterns in the specimen at the different ultimate bond stress levels and the damage patterns in Figure 5.14 (e-h) for each case. Figure 5.14 (i) shows the failure mode observed in the experimental test of the specimen reinforced with CSS-wires, which fails with a single crack. And Figure 5.14 (j) displays the failure mode of the specimen reinforced with BSS-wires, which in contrast, presents a distribution of multi-cracks.

An exam of the numerical results provides some insights on how the value of the ultimate bond strength affects the fracture process. A single opening crack pattern at the central part of the specimen, almost perpendicular to the longitudinal direction, can be identified from the iso-displacement contours for $\tau_u^f = 2.5MPa$, which reproduces the experimental observation with CSS-wires. The single crack pattern repeats for $\tau_u^f = 4.0MPa$ and $\tau_u^f = 5.5MPa$ but the cracks propagates horizontally, indicating thereby, that a stronger interface arrests the additional development of the crack trough the transverse direction of

the specimen. Experimentally, in the CSS-wire reinforced specimen, the crack branched out of the transverse plane at the end of the test as in the picture Figure 5.14(i), which coincides more with the crack patterns for $\tau_u^f = 4.0 MPa$ and $\tau_u^f = 5.5 MPa$.

(a) $\tau_u^f = 2.5 MPa$ (e) $\tau_u^f = 2.5 MPa$

(b) $\tau_u^f = 4.0 MPa$ (f) $\tau_u^f = 4.0 MPa$

(c) $\tau_u^f = 5.5 MPa$ (g) $\tau_u^f = 5.5 MPa$

(d) $\tau_u^f = 7.5 MPa$ (h) $\tau_u^f = 7.5 MPa$

(i) CSS-wire reinforced beam   (j) BSS-wire-reinforced beam
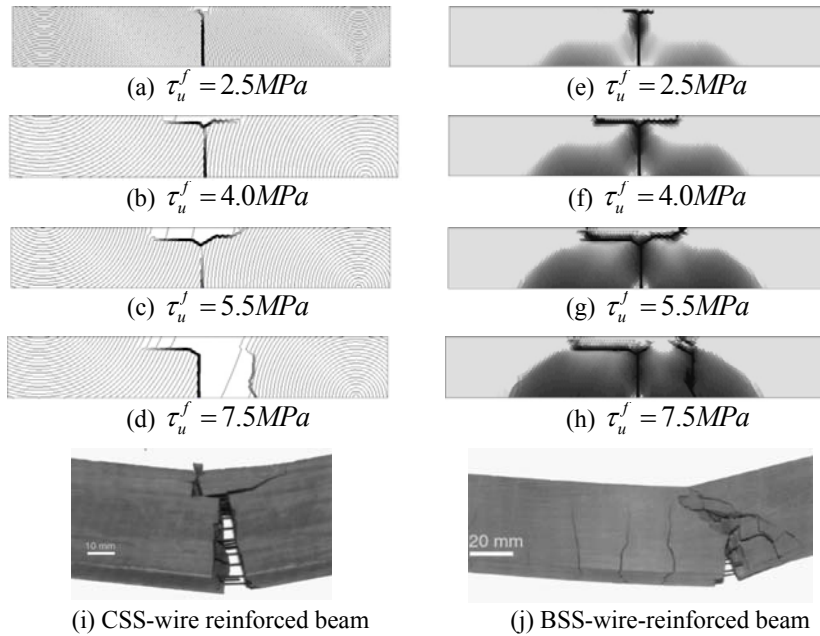
Figure 5.14. CSS- and BSS-wire reinforced beam ($V_f = 1\%$) of the beam test: (a-d) numerical (indicated by the displacement contours) and (i-j) experimental crack patterns for different values of the ultimate bond shear strength. (e-h) Damage iso-color maps.

Figure 5.14 (e-h) shows the iso-color maps for the damage parameter: darker colors represent more degraded material. According to the results of Figure 5.14 (e-h), the extension of the damaged area depends on the ultimate bond strength, as far as the considered cases are concerned. The damaged area around the main crack is usually small for small values of the ultimate bond strength, in other words, the fiber-matrix interface is so weak that the matrix strain is not transferred to the fiber. The damaged areas spread gradually as the interface strength increases. For $\tau_u^f = 7.5 MPa$, damage localization is noticeable and induces propagation of two main cracks. It is apparent, from the preceding discussion and from the pictures of the experimental specimens in Figure 5.14 (i-j), that the crack pattern for CSS-wire reinforced beam resembles the crack pattern found by numerical simulation with small values of τ_u^f and BSS-wire reinforced beam displays a failure mode that is significantly consistent to that of the simulation response for $\tau_u^f = 7.5 MPa$.

5.3.2.1. Deflection-softening

The name deflection-softening performance is adopted for HPFRC composites showing a loss of the structural loading carrying capacity after reaching the first cracking point, as classified by (Kim et al. 2008). Note that according to the above definition, structural responses for $\tau_u^f = 2.5MPa$ and $\tau_u^f = 4.0MPa$ fall into this category. It is apparent that fiber-matrix bond strength is responsible for the ineffective load transfer between both compounds and consequently insufficient stress distribution capability between them. This effect is observed in the damage distributions presented in Figure 5.14 (e-h).

Figure 5.15. (a) Plasticity maps and; (b) debonding maps in the beam with $\tau_u^f = 2.5MPa$. The red color indicates elements in inelastic regime.

Figure 5.15 represents the contour plots of debonding and plasticity in the beam using $\tau_u^f = 2.5MPa$, as the fiber matrix ultimate bond strength. Inspection of Figure 5.15(a) shows that the postcracking failure mechanisms involve plasticity along the crack path. Accordingly, the experimental observation shows that nearly all CSS-wires are easily pulled out without much deformation of the fiber. However, the fibers deforms because of bending at crack location during crack opening. On the other hand, the first distinctive feature in the plots of Figure 5.15(b) is the sudden increase of the area affected by fiber debonding (t = 1), which evolves progressively to neighboring regions, as well as areas under compression (t = 2 and t = 3). Note that the debonding domain affects the middle third of the beam covering not only the macrocrack surrounding but also regions relatively remote from it. Therefore, as it may be surmised, low ultimate bond strength reduces the bridging effect (or the capacity to transfer stresses between the matrix and the fiber) and directly decreases the interface toughness (pullout energy). In this case, a bridging zone is clearly detectable in the beam center, where the fibers are pulled out, as shown in the results in Figure 5.15 (a) and (b). Admittedly, bridging force, which are the discrete forces acting on the microcrack when it opens (Radtke et al. 2010), must be interpreted to be of continuous nature in the current model, although from physical evidence these forces have discrete nature.

5.3.2.2. Deflection-hardening response.

Deflection hardening response is characterized by multiple cracking after the first point in the specimen initiates the crack processing, as observed in Figure 5.14 (h). This behavior could be attributed to the high pullout resistance and slip capacity originated from the straightening of the fiber. In fact, significant damage in the cement matrix occurs for BSS-steel wires, as a result of the pull out forces. Figure 5.16 (a) and (b) describe the debonding and plasticity evolution, respectively, during the fracture process. It is important to remark that the red areas show the points, which exceeded the threshold value. These results suggest that, in order to be effective in concrete, pullout of fibers should involve plasticity and de-bonding fracture processes, so as to provide much more ductility and toughness.

Various failure modes including, among others, damage, plasticity, spalling and debonding are encountered in beam bending tests of HPFRC composites. It is recognized from Figure 5.16 (a) and (b) that fiber pull-out mainly concentrate at the actual macrocrack surfaces as a mechanism to arrest the crack propagation, whereas, in the rest of the specimen, the behavior of the composite material remains under complete composite condition. As in experimental observations, plasticity is predicted around the crack path during pulling out the fiber, as in Figure 5.16 (a), which is largely caused by the fiber straightening and bending. In the experimental case, straightening implies deformation of the mechanical anchorage owing to interlocking between the enlarged end of the BSS-steel wires and the matrix. Therefore, well-anchored fibers deform plastically, providing a toughness increase to bending performance. In addition, development of plasticity indicated in the beam top is probably promoted by buckling in fibers under compression. As depicted in Figure 5.16 (b), a sequence of the debonding distribution results display fiber-matrix interface failure in the surrounding macrocrack areas. The beam simulation results show large slip ability during pull out which generates much higher pullout energy.

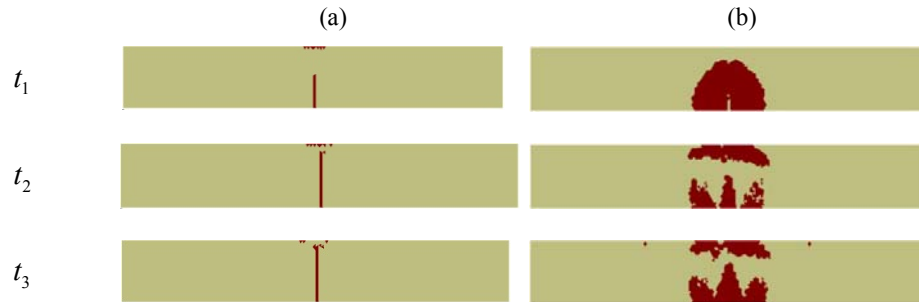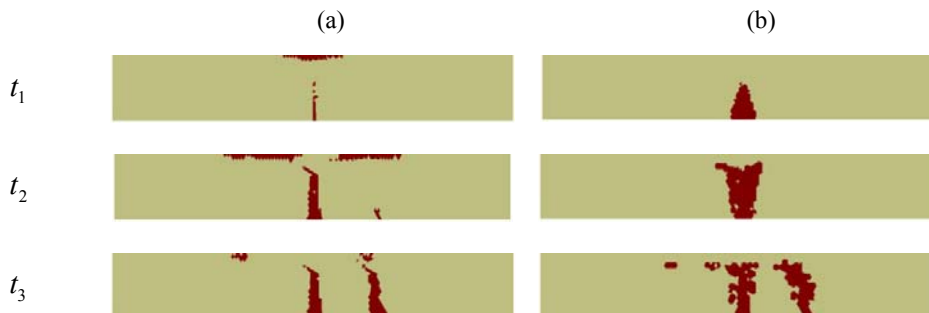

Figure 5.16. (a) Plasticity maps and; (b) debonding maps in the beam with $\tau_u^f = 7.5MPa$. The red color indicates elements in inelastic regime.

5.4.   Test 3: Beam with randomly distributed fibers

Randomly orientated fibers reinforced composites are frequently the case in the practice. This reason motivates to perform a test similar to the one in section 5.3, but for randomly distributed fibers. The experimental evaluation of this example was presented by (Bencardino et al. 2010). The three point bending test on notched specimen was carried out according to the RILEM specification (162-TDF 2002). The beam geometry is described in Figure 5.17 (a), the notch is situated in the middle span and it is sufficiently small to avoid undesirable effects. Figure 5.17 (b) represents in detail the cross section in which is indicated the notch dimension.

(a)   (b)
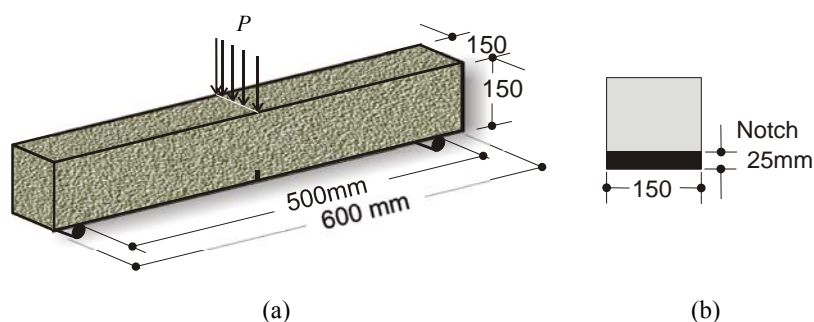
Figure 5.17. Set-up of bending flexural test (Bencardino et al. 2010).

The beam contains the steel fibers Dramix® of hooked end. In Box 5.4, the mechanical properties of the matrix, fiber bundles and interface zone are defined. Nine fiber bundles were included in the analysis and it is assumed that this number represents sufficiently well the random distribution of the fibers.

Matrix	Fiber	Debonding
$f_c' = 1.25 MPa$	$\sigma_u^f = 1050 MPa$	$\tau_u^f = 5.1 MPa$
$E^m = 13.89 GPa$	$E^f = 210 GPa$	$E^d = 1e + 8 GPa$
$\upsilon^m = 0.2$	$H^f = 100 MPa$	$H^d = 100 MPa$
$G_f = 100 N/m$	$\theta = \begin{bmatrix} 0°, 10°, 20°, 30°, \dots \\ 45°, 60°, 70°, 80°, 90° \end{bmatrix}$ $\phi_f = 0.3 mm$	$V_f = 1.0\%$

Box 5.4.Bending test with randomly distributed fibers: Compound mechanical properties

5.4.1.   Flexural tensile behavior

Characteristic brittle behavior is observed in experimental unreinforced specimen, as is shown in Figure 5.18. The complete separation of the specimens into two parts occurred in the test, as illustrates Figure 5.19-a. Likewise, in the finite element simulation, a single crack is observed, as in Figure 5.19-b (The deformed mesh is scaled 15 times to see the crack). The simulation parameters are summarized in Box 5.5.

Number of nodes	Number of elements	Type of element	Type of formulation
4032	3938	quadrilateral	Standard and injection of a strain constant mode

Box 5.5. Description of the numerical test.

The load deflection displacement curve of the fiber reinforced concrete specimen with 1% of fiber volume fraction is presented in Figure 5.18, ((Bencardino et al. 2010)), along with the response of the simulated specimen. Experimental and numerical curves agree quite well up to the peak load, but after this point, the proposed model slightly overestimates the load.
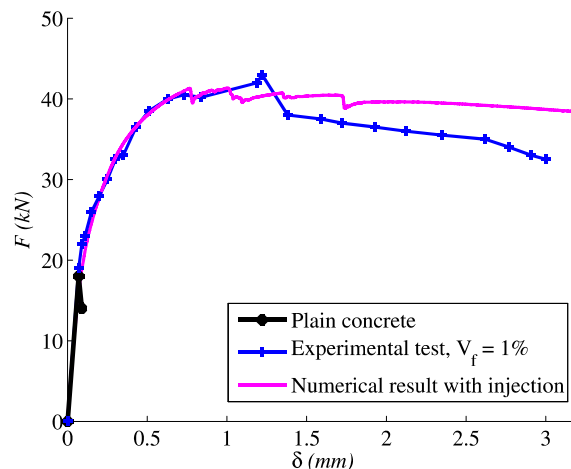
Figure 5.18. Numerical and experimental load versus deflection in three point notched beam test.

The damage distribution at the end of the loading process is represented in Figure 5.19-c, for plain concrete. Not surprisingly, the damage concentrates in the notched region. The crack pattern of the reinforced specimen displays a single crack when using the approach presented in this work. This is represented in Figure 5.20-a. The corresponding experimental crack pattern also presents a single crack (see Figure 5.20-b). However, the specimen does not split abruptly in two parts as for the unreinforced beam. The deformed configuration of

the beam after loading is scaled by 10 in Figure 5.20-c. Comparing Figure 5.20-c and Figure 5.19-b is evident that the deformation of the reinforced beam is much larger than the unreinforced one.

(a)

(b)

(c)
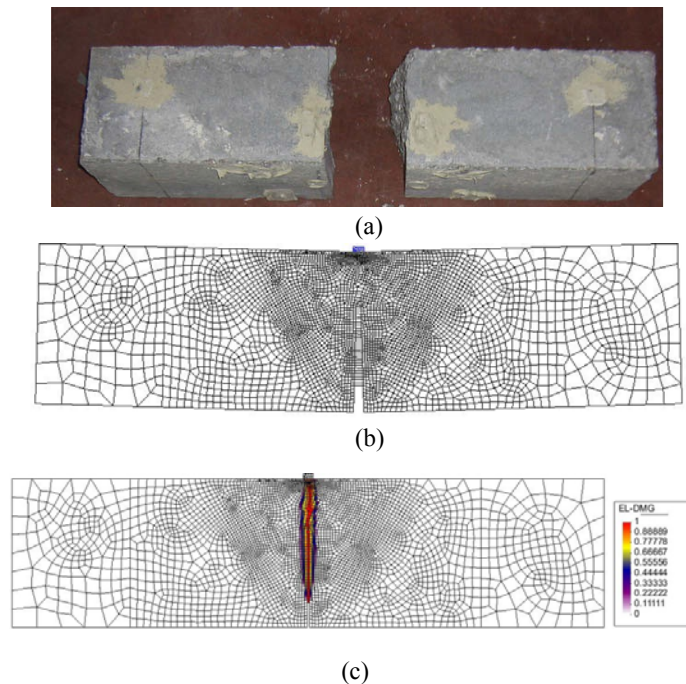
Figure 5.19. Numerical and experimental load versus deflection in three point notched unreinforced beam test (a) Experimental crack pattern (b) Simulation result, deformed and crack pattern for the beam. Deformed factor =15. (c) Damage iso color map.

5.4.2.   Mesostructural behavior

It is noticeable the manner in which the introduction of the balance equation of the mesomechanic allows the model to represent the ductility of the material response (Figure 5.18). The coupled effect of the fiber matrix interface debonding and the axial plastic strain in the fiber affect the composite behavior in such a manner that the brittleness of the unreinforced material is removed. The three linear response of the fiber reinforced composite is now clearly associated with an extensive cracking process. Figure 5.21 and Figure 5.22 display the evolution of the simultaneous loss of adhesion in the IZ and the plastic strain of fibers, respectively. For easy understanding, three bundle fibers and different representative states along the load deflection curve were chosen to be analyzed. According to these results, both processes

concentrate in the region near to the notch, where is expected to occur the crack propagation. The attention is addressed initially to analysis of the debonding distribution of the fiber bundles oriented 0º and 45º respect to the longitudinal direction (Figure 5.21(a) and (b) respectively). These results suggest that the loss of the adhesion in the interfacial zone happens from initial loading stages. However, for the bundle fiber oriented 90º, (Figure 5.21(c)), the distribution displays that the process begins later and it does not affect the area located near to the notch.

(a)   (b)

(c)
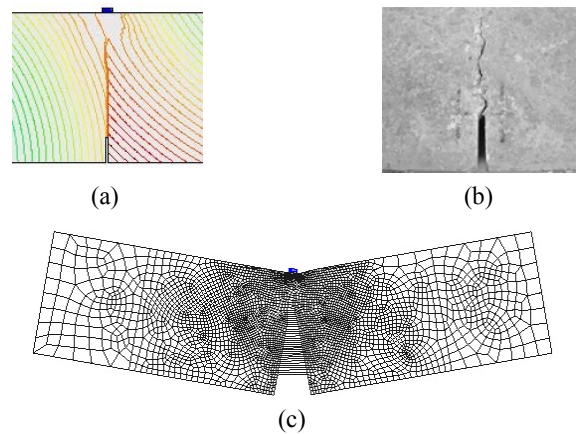
Figure 5.20. Numerical and experimental load versus deflection in three point notched beam test with reinforcement. (a) Iso displacement contours. (b) Experimental crack pattern. (c) Deformed beam, numerical result, deformed factor = 10.

(a) 0º   (b) 45º   (c) 90º
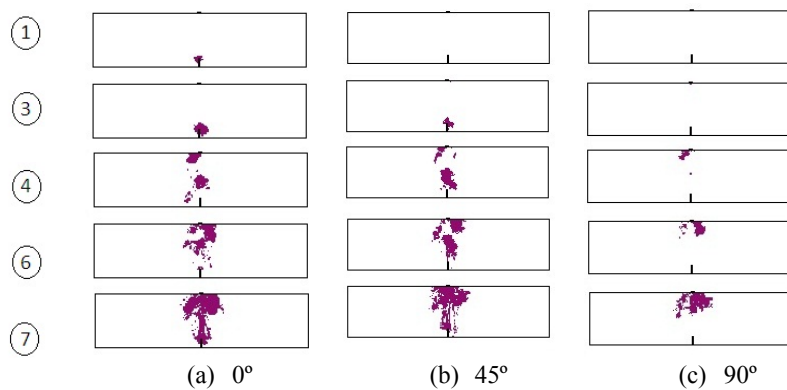
Figure 5.21. Numerical evolution of the debonding process in the notched beam test. The magenta color indicates elements in inelastic regime.

The distribution of yielding represented in Figure 5.22 shows that fibers located along the crack path yield as a consequence of the crack opening when they are oriented at 0º and 45º (Figure 5.22(a) and (b), respectively). However, for the bundle fiber oriented in the perpendicular direction respect to the longitudinal beam axis, the areas showing yielding (Figure 5.22(c)) is much smaller than those in fiber bundles oriented in other directions (in this particular case 0º and 45º). This result suggests that the smaller the inclination angle of the fiber bundle the more is the amount of the yielding generated.

(a) 0º   (b) 45º   (c) 90º
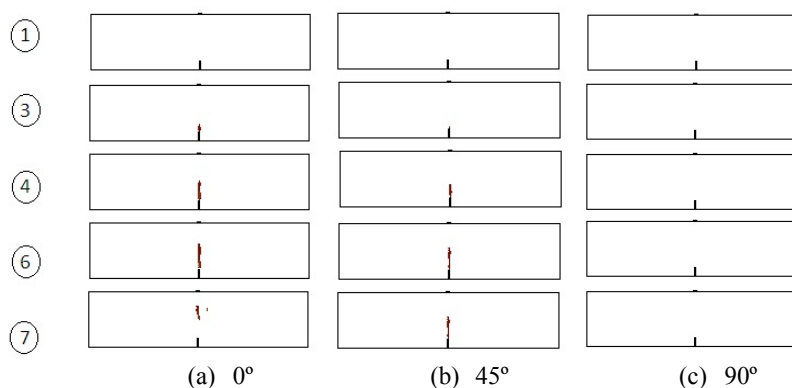
Figure 5.22. Numerical evolution of the plasticity in three point notched beam test with reinforcement. The red color indicates elements in inelastic regime.

5.4.3.   Damage evolution and localization process

Microcracking in the cement matrix occurs simultaneously with debonding and yielding during the fracture process. Figure 5.23 displays the load versus displacement curve, in which seven points were tagged with numbers throughout the curve indicating different stages of the damage evolution in the beam. On the right side of the curve, the corresponding damage iso color maps are shown.

In the stages 1 and 2, few elements around the notch are damaged. As loading progresses, the damage region spreads over beyond the notch section. In the stage 3, some elements in the bottom part of the beam begin to damage. From stage 3, the damaged region covers the middle third and remains almost unaltered until the end of the loading process. Darker red color stands for completed damage material. According to the iso color map in the stage 7, severe degraded material is presented in the notch proximity and in the symmetrical region around it. However, comparing this result and the iso displacement contours in Figure 5.20(a) only a single macrocrack is developed in the notch, in other words, no multiple cracks are shown in this case. It is remarkable in the iso-color maps Figure 5.23 in that the white areas show undamaged material. From this result and Figure 5.21 and Figure 5.22, it follows that a good part of the material remains elastic and it behaves as a composite during the complete loading process
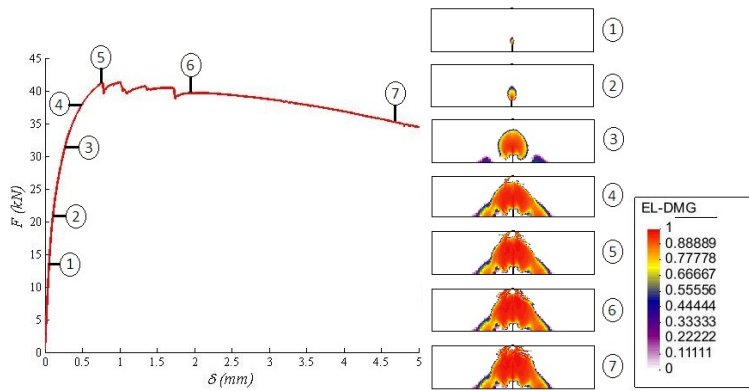
Figure 5.23. Numerical and experimental load versus deflection and damage evolution in three point notched beam test.

The evolution of the injection of the constant strain mode in the bifurcated domain is illustrated in Figure 5.24. Dark blue coloured areas display the elements injected in the beam for different stages indicated with the tagged points in the load versus deflection curve. During the hardening loading part of the curve, stages 1 to 5, the bifurcation domain resembles the damage evolution presented in Figure 5.23 with slightly differences. However, the injected domain changes suddenly and it is reduced to a line of element where the localization of deformation concentrates (stages 6 and 7).
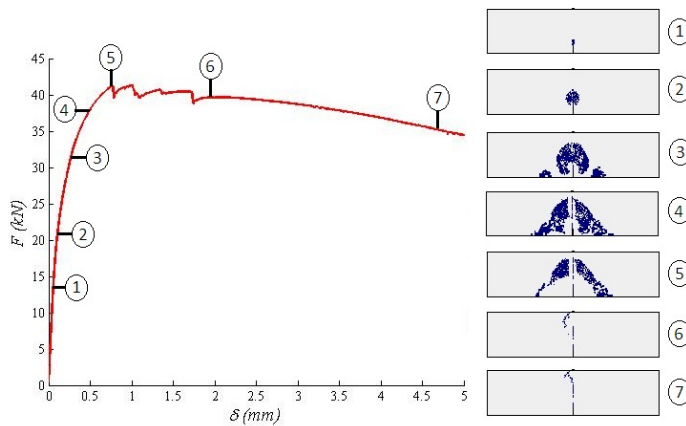
Figure 5.24. Numerical and experimental load versus deflection in three point notched beam test with the tagged points, where the analysis of the injection of the strain constant mode is applied. The elements that belong to the injection domain are indicated in the beam with darker blue.

Again, it is noticed that the region next to de notch and in the bottom of the beam are initially injected but any crack is formed out of the notch section and thereby in stage (6) and during the rest of the loading process any injection is performed these regions.

5.5.   Test 4: Dogbone specimen test

In general, tensile tests are performed indirectly via bending and split-tensile tests. These indirect tests give results that are not strictly comparable with those provided by direct tensile tests, because the existence of a compressive stress component that may be far greater in magnitude than the induced tensile stress, and whose influence at failure cannot be considered (Broch & Franklin 1972). The direct tensile test is seldom used, yet it is one of the best methods to characterize the tensile behavior. Although the uniaxial tensile test involves such difficulties, the objective of the Suwannakarn's work (Suwannakarn 2009) was to evaluate and model the postcracking behavior of HPFRC composite using it. An extensive experimental program was carried out using direct tensile tests and stress vs. crack opening displacement tests on notched tensile prisms. Initially, the cementitious matrix specimen was evaluated, in order to provide a basis of comparison and for control. Subsequently, the direct tensile test using fiber reinforced dog-bones is performed and then the crack opening displacement test using fiber reinforced notched prisms. Due to the scatter of the experimental results reported in Suwannakarn's work, a detailed discussion was dedicated about the observed variability in HPFRC composites response.

It should be kept in mind, judging the results of HPFRC composites, that the variability of their responses is strongly influenced by many factors. In the case of randomly oriented fiber composites, the orientation within the matrix bulk depends on the processing details such as the method of placing the fiber concrete mix, flow characteristics of the mortar, and type of compaction. Other factors that tend to increase the statistical variability include the variation of concentration of fibers inside the specimen, variability of the matrix-fiber interface or local concentration of air inside the matrix among others. Further discussion about this topic is beyond of the scope of this work and the reader is addressed to (Li & Wang 2006) and (Wang et al. 1989).

5.5.1.   Dogbone specimen test; Plain mortar material

Figure 5.25 illustrates a scheme for the tensile testing of a dogbone specimen. The direct tensile strength of mortar was tested using dogbone specimens as shown in Figure 5.25 (a). The dimensions of the dogbone are given in Figure 5.25 (b) and (c). The finite element mesh, shown in Figure 5.26-(a), consists of quadrilateral elements, using a 2D plane stress model.
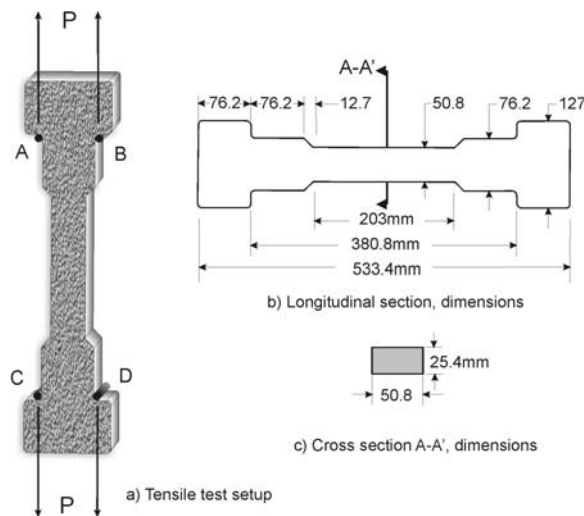
Figure 5.25. Scheme for the hooked end fiber reinforced dogbone specimen used in the
tensile test (Suwannakarn 2009).

Under monotonic tensile load, the specimen failed in a brittle manner and only a single crack was observed. Experimental results showed that the stress-strain behavior of mortal specimens did not exhibit perfect linear behavior. Moreover, the measured elastic modulus ranged between 7804 and 26717 MPa with an average of 13886 MPa. The used mortal appears to have significantly less stiffness than the regular concrete. The cracking strength presented a large variability and the average value was estimated to be 1.25MPa.

To perform the numerical simulation, vertical displacements were imposed in points A and B, as presented in Figure 5.25 (a), to stretch the specimen. The vertical reactions in points C and D were monitored continuously throughout the simulation. In the experimental campaign, the average elongation was obtained from points E and F spacing about 178mm. In order to trigger localization of deformation from a homogeneous state, a weak element was included in the middle of the specimen, slightly perturbed in terms of its strength (reduced 10%).

Figure 5.27 (a) shows the envelope of the experimental data and the average value. Likewise, Figure 5.27(a) compares the stress-strain curve computed using the numerical simulation with the one obtained from experiments. As it was expected, a single crack leads to the specimen failure (see Figure 5.27(b)).
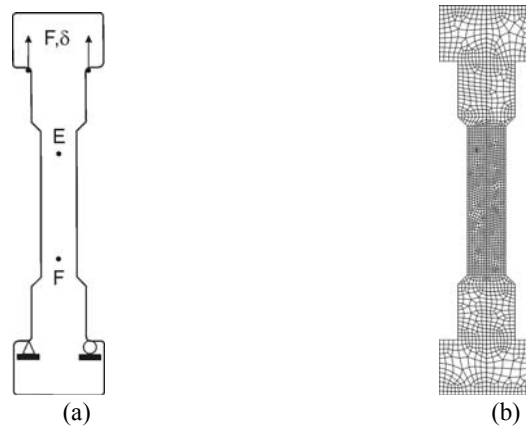
Figure 5.26. Dogbone specimen. (a) Numerical test layout. (b) Finite element mesh.
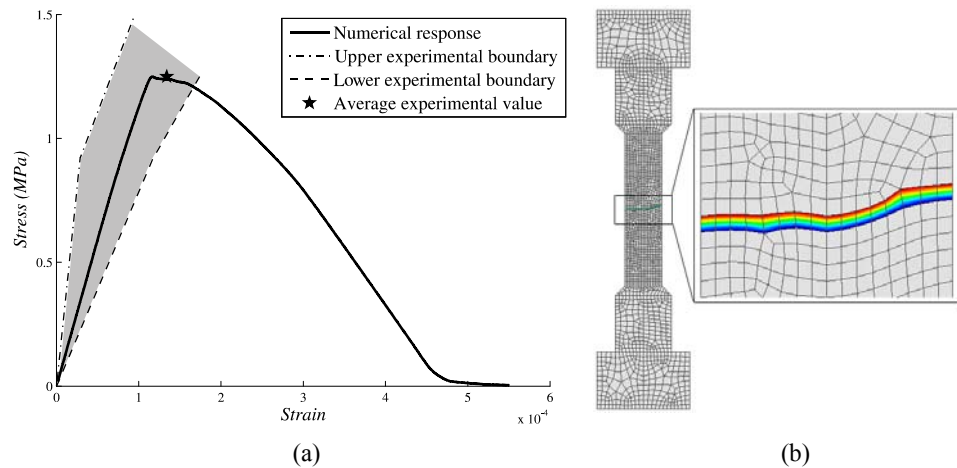
Figure 5.27. Stress versus strain of the unreinforced dogbone specimen: (a) numerical and experimental curves (Jiang et al. 2000), (b) crack pattern using the continuum with microstructure based model.

5.5.2. Dogbone specimen test: HPFRC composite material

During the specimen preparation, care was taken to prevent clumping of the fiber. Therefore, the random distribution of the fibers can be considered uniform. Although this fact suggests that the model should involve all the possible fiber orientations, for obtaining the response of this specimen, we assume that nine fiber bundles, which are regularly separated, and we believe that this is a reasonable approximation to the real distribution.

Number of nodes	Number of elements	Type of element	Type of formulation
2125	1967	quadrilateral	Standard and injection of a strain constant mode

Box 5.6. Description of the numerical test with details of the finite element mesh.

The matrix mechanical properties, provided by the tensile response of the dogbone without fibers, are used as input data for reinforced specimens. Hooked end fibers, commercially known under the trademark "Dramix®", were used in the experimental study. Fibers with two different tensile strengths were used, nonetheless, high strength steel fibers, with circular cross-section, were employed to simulate the composite material. Based on previous studies (Guerrero Z 1999), the authors reported typical values for the ultimate equivalent bond strength. Accordingly, bond strength for high strength steel fibers was estimated at 5.1 MPa. Box 5.6 summarizes the set of simulation parameters and in Box 5.7, the main mechanical properties used in the simulation of the HPFRC composite appear, where f_c', is the ultimate concrete tensile strength, E^m, is the matrix Young's modulus, υ^m, is the Poisson ratio, and G_f, is the fracture energy of the matrix. For the fiber σ_u^f is the yield stress, E^f is the Young's modulus, H^f, is the hardening parameter and V_f, is the fiber volume fraction. For the matrix-fiber interface (IZ), the parameters include τ_u^f, E^d and H^d, which stand for the ultimate bond strength, the Young's modulus and the hardening parameter, respectively. The preliminary simulation results achieved with the notched strip have suggested better performance of the quadrilateral element; therefore, the simulations for the current example are carried out using this element. With a view to comparing the effectiveness of the injection procedure, the example is also solved using the standard element and the injection of a strain constant mode.

Matrix	Fiber	Debonding
$f_c' = 1.25 MPa$	$\sigma_u^f = 2100 MPa$	$\tau_u^f = 5.1 MPa$
$E^m = 13.89 GPa$	$E^f = 210 GPa$	$E^d = 1e + 8 GPa$
$\upsilon^m = 0.2$	$H^f = 100 MPa$	$H^d = 100 MPa$
$G_f = 100\, N/m$	$\theta = \begin{bmatrix} 0°, 10°, 20°, 30°, \ldots \\ 45°, 60°, 70°, 80°, 90° \end{bmatrix}$ $\phi_f = 0.4 mm$	$V_f = 0.75\%$

Box 5.7. Dogbone tensile test: mechanical properties of the composite.

The tensile stress-strain curves for the test series are represented by the lower and upper envelopes, which are given in Figure 5.28. Comparing the numerical (with the injection procedure) and experimental results, they compare well and confirm that the model can approach the mechanical behavior of the HPFRC composite with fibers oriented in several directions.
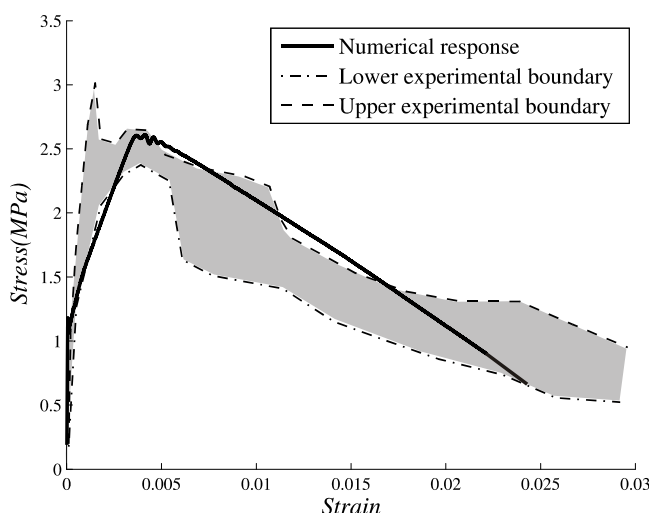
Figure 5.28. Comparison of the experimental results of the dogbone specimen and numerical curves using quadrilateral finite element and injection of constant strain mode.

In the numerical response curve, the first crack point, defined as the point at which starts the nonlinearity in stress strain curve, is clearly identified. Unlike the unreinforced specimen (Figure 5.15 (a)), the response shows hardening after first crack and the combined effect of the matrix and the fiber causes stiffness change. Strain hardening effect occurs up to a stress value of at least 2.6 MPa. According to the experimental data, the average maximum stress value was 2.71 MPa.

5.5.2.1. Fiber-matrix debonding and fiber pull out

The developed model allows observing details in the microstructure. During the stretching process, debonding and pullout of the hooked end fibers is expected. The simulation of the dogbone specimen leads to a vast amount of results. Let us consider three fiber bundles of the nine that originally has the specimen. For simplicity, we analyses the fiber bundles at 0º, 45º and 90º respect to the loading direction. In Figure 5.29, each row represents one bundle at different stages during the stretching process. The stages are marked according to Figure 5.30.

At stage 3, 4, 5 and 7, couples of pictures are displayed: on the left, the distribution of elements that reach the ultimate bond shear stress and, on the right, the distribution of the elements that reach the yield stress. The stages (3) and (4), for $\theta = 0º, 45º, 90º$, belong to the

hardening state, between the first crack stress point and the peak stress. During this stage, the fibers debond from the matrix and remain in elastic regime.
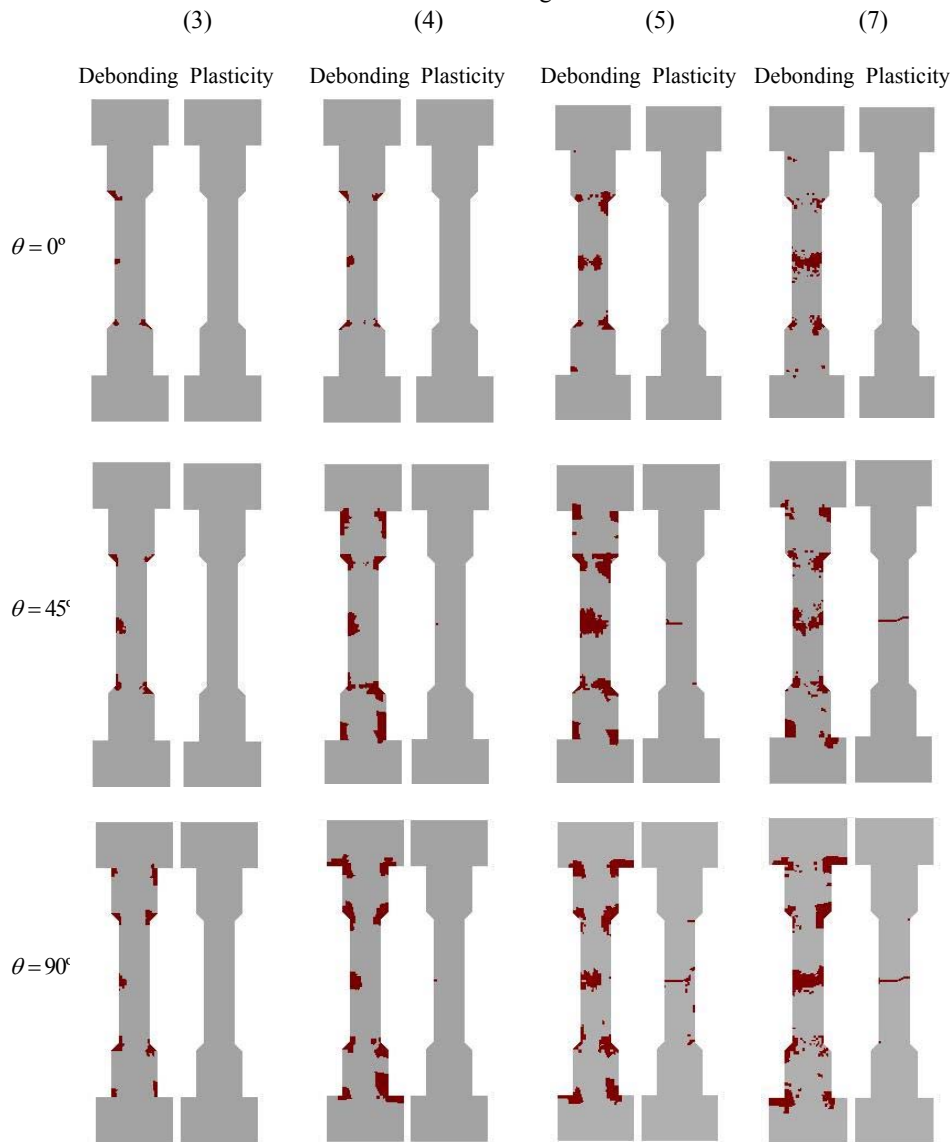
Figure 5.29. Main stages of the debonding and plastisity during the tensile test simulation for three representative bundles of fibers $\theta = 0°, 45°, 90°$. On the left, marked with red, the distributions of the element that reach the ultimate bond shear stress. On the right, the distribution of elements that reach the yield stress

Experimental works indicate that inclined fibers, with small angles respect to the load direction, and aligned fibers contribute more to the improvement in hardening performance. In stage (3), we can observe that for the aligned fibers ($\theta = 90º$), more elements reach the debonding condition if compared with the solution obtained using the horizontal ones ($\theta = 0º$). Debonding mechanism evolves significantly for aligned fibers in the stage (4), and not so much for horizontal ones.

Stages (5) and (7) represent points in the postcracking regime (with reference to curve in Figure 5.29). The horizontal fiber ($\theta = 0º$) remains elastic, while the inclined and aligned fibers ($\theta = 45º$, $\theta = 90º$, respectively), reach the yield condition in the elements on the crack path. The experimental evidence ((Robins et al. 2002), (Cunha et al. 2007), (Barros et al. 2005)) reported that the inclined hooked-end fibers present straightening and removal during the pullout. Therefore, in presence of a crack, plastic strain can be developed in various locations of the fiber near to the exit point. Although the hooked end are not explicitly considered in the model, the value of the ultimate bond strength reported by (Guerrero Z 1999) takes into account the straightening of the fiber during the pullout. This fact explains the plasticity is developed in the inclined fibers after occurring strain localization. Inspection of the debonding distributions in stage (5) and (7) suggest that all fibers around the macrocrack present debonding, with consequently loss of load-carrying capacity, and therefore a decrease of the composite resistance is observed in the stress-strain curve.

5.5.2.2. Strain localization and effect of the element formulation on the results

Figure 5.30 illustrates the stress-strain numerical curve, obtained by simulating the dogbone specimen presented in Figure 5.25. The mechanical properties are summarized in Box 5.7. The points tagged with the numbers 1 to 7 along the curve were selected to monitor the evolution of the injection domain of the constant strain mode as explained in section 3.3.2, when this approach is used in capturing the crack path. This result suggests that the injection initiates with the beginning of the hardening stage (Stage (1)). Then, in Stage (4), the injection domain spreads out to occupy the major part of the specimen and a large number of elements are injected. However, the number of elements injected reduces dramatically in the stage (5) and at the end of the simulation process, the elements on the failure path remain further injected.

Strain localization in experimental tests occurred without fiber failure, but multicracking is reported on the hardening branch. For the numerical simulation, strain localization occurs only after the peak stress, which is preceded by multicracking or "smeared damage". It is worth noting that multicracking cannot be captured by standard homogenized models and therefore the inclusion of the mesostructure allows the model to obtain multicracking before strain localization in a natural way.

It is remarkable that the use of the strain injection procedure can evaluate successfully the crack path, at least for this case, when multiple fiber bundles are considered in the analysis. The approach has proven in the simple example of the notched strip some improvement in terms of the localization pattern but in the mentioned case, only one fiber bundle was included in the simulation.
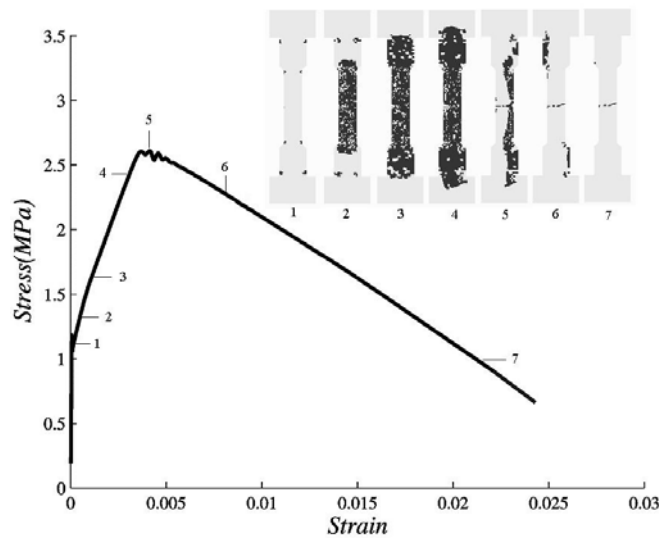
Figure 5.30.Stress – strain numerical curve of the dogbone specimen reinforced with hooked end fibers and injection evolution.

Unfortunately, direct comparison with experimental crack pattern is not possible in this example since no crack pattern is reported in the work of Suwannakarn. As for the numerical results, at the end of the tensile direct test, the solution of the localization pattern for the standard and the localization mode injection are depicted in Figure 5.31. Only one single macrocrack is observed in the specimen by using both alternatives. By restoring the results presented in Figure 5.29, it is possible to conclude that the failure process is controlled by the pulling out of the fibers.

(a)   (b)   (c)
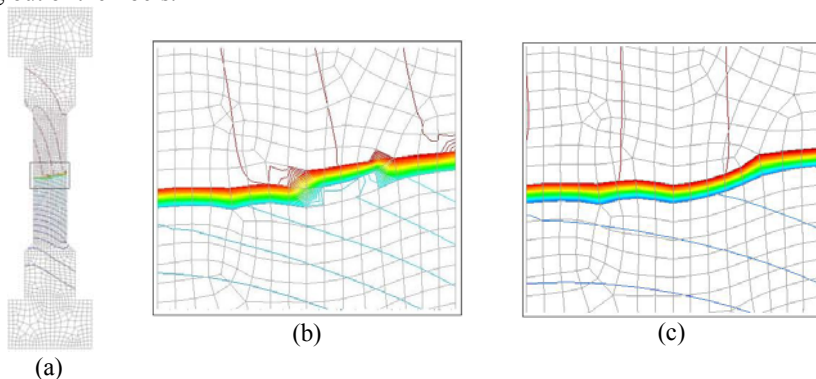
Figure 5.31. Iso displacement contours at the end of the analysis of the dogbone specimen reinforced with hooked end fibers. (a) Complete specimen showing the macrocrack in the middle section. (b) Crack pattern for the standard quadrilateral element formulation. (c) Crack pattern for the standard quadrilateral element formulation with strain injection procedure.

5.5.2.3. Bridging effect caused by fibers and matrix damage

Figure 5.32 illustrates different stages in the evolution of the damage pattern by means of contour fills, which correspond to the points marked in Figure 5.30. It is to be noted that no interpolation of the integration point data of damage is performed. Note that the limits used to represent this distribution range from 0.95 to 1.0. As expected, high values of damage in concrete matrix are presented in early stages, which are interpreted as microcracking (Stage 2). Before strain localization, stages 3 and 4, large areas of the specimen are severely degraded. This is evidence of bridging effect, which takes place in the specimen. Although the strain localization process is almost completed for stages 5 and 7, the damage distribution contour fills show a damage factor increase. In the localization band, the value of the damage parameter indicates that the matrix stiffness is completely exhausted; however the stress-strain curve at stage 7 shows a residual stress due to the remained fiber loading capacity.
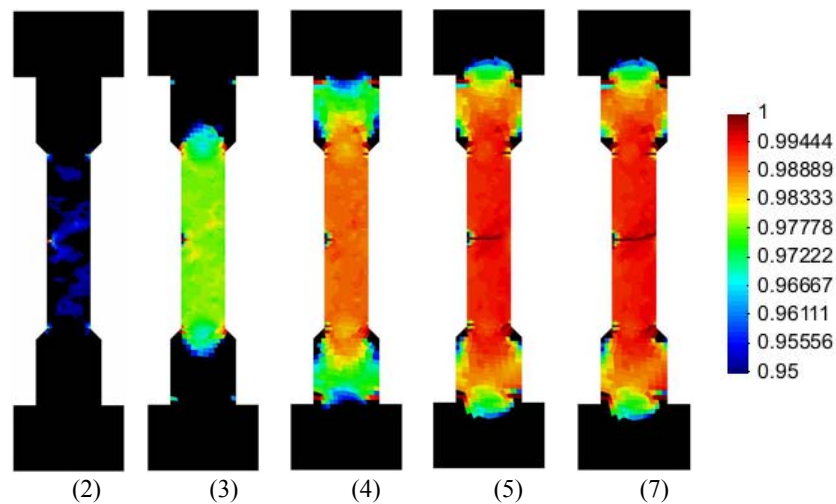
Figure 5.32. Numerical damage evolution during the direct tensile test simulation of the dogbone specimen.

5.5.2.4. On the effect of the fiber volume fraction

So far, the discussion was dedicated primarily to examine the results for $V_f = 0.75\%$, however, experimental results for other fiber contents by volume were tested by (Suwannakarn 2009). Simulation for $V_f = 1.0\%, 1.5\%$ are carried out, so as to obtain stress-strain curves. In Figure 5.33 are compared the numerical responses with the corresponding experimental ones.
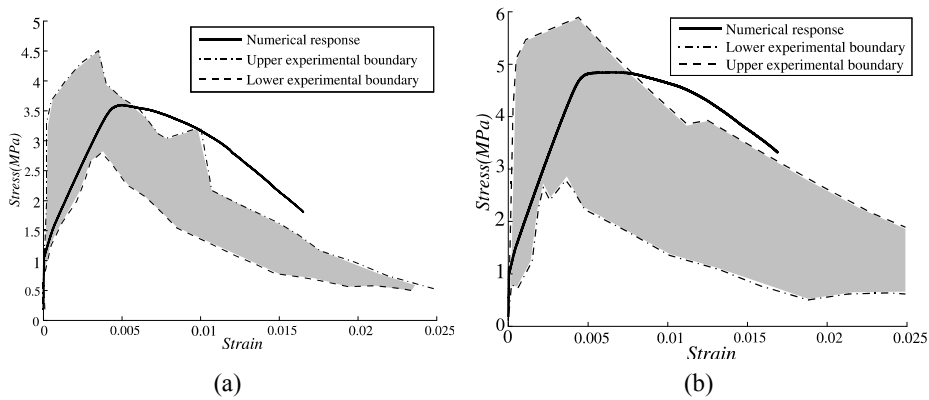
Figure 5.33. Stress – strain numerical curve of the dogbone specimen reinforced with hooked end fibers and injection evolution. (a) $V_f = 1.0\%$. (b) $V_f = 1.5\%$

5.6.   Test 6: Crack opening displacement test (COD, Notched prism test)

The dogbone-shaped notched specimen of fiber reinforced concrete is used to control the location of the crack position. To ensure adequate propagation path, the specimen has symmetrical notches at their middle section. This test setup is ideal to measure some fracture properties of this composite and to estimate the size of a pseudo plastic zone, which corresponds to the cracked area of the matrix (Suwannakarn 2009).
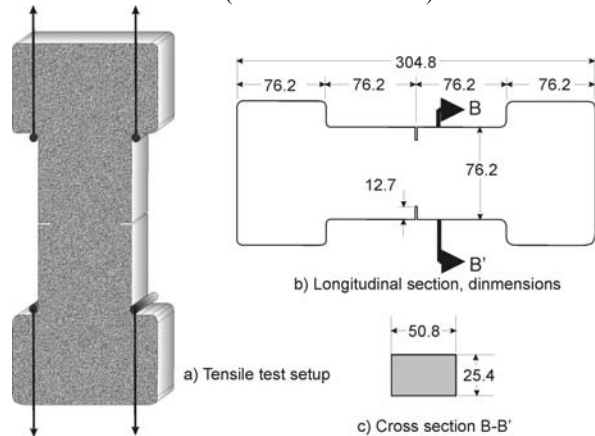
Figure 5.34. Scheme for the tensile testing of a double-notched dogbone specimen (Suwannakarn 2009).

The geometric details are shown in Figure 5.34. Dimensions are given in Figure 5.34 (b) and (c) for the longitudinal- and cross-section, respectively. In the experimental setup, two crack gauges were placed one on the left and the other on the right, spanning each notch to measure the displacement. On the simulated specimen, displacements were measured in the position indicated in Figure 5.35(a) with the letters a-d. During the tensile test, displacements were imposed at the top and restricted in the bottom as indicated in Figure 5.35 (a).

The finite element mesh, shown in Figure 5.35(b), consists of 1639 bilinear quadrilateral elements. Note that the mesh was refined locally in the neighboring area of the notches to prevent inadequate crack propagation and in order to simulate accurately the crack opening process.

(a)   (b)
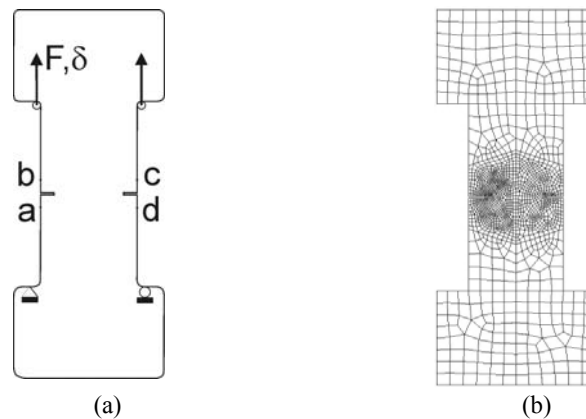
Figure 5.35. Double notched dogbone specimen. (a) Numerical test layout. (b) finite element mesh

Number of nodes	Number of elements	Type of element	Type of formulation
1723	1639	quadrilateral	Standard and injection of a strain constant mode

Box 5.8. Description of the double notched dogbone numerical test: details of the finite element mesh.

5.6.1.   Stress versus crack opening displacement curves

Figure 5.36 shows the stress versus crack opening displacement curves for the numerical simulation and the envelope of the experimental tests. Following the initial elastic response, the curve presents strain hardening due to the multiple cracking. As for the numerical result, it lies within the experimental envelopes. However, one can immediately see from this result

that the post cracking branch of the curve deviates significantly from the experimental data. Nevertheless, keeping in mind the large variability reported in experiments and the small number of specimens used for this case (only 3). The coefficient of variation (normalized measure of dispersion) for the toughness in specimens using hooked end fibers presented values over 60.
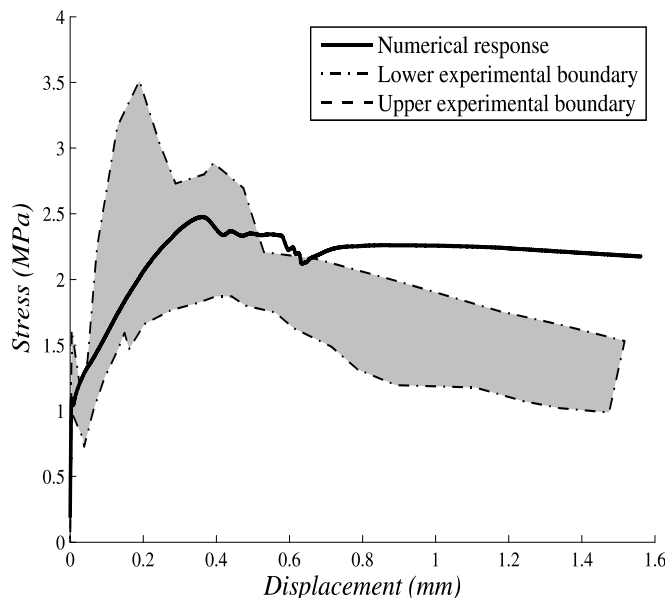
Figure 5.36. Numerical and experimental crack pattern in double notched test.
(a) Numerical curve. (b) Experimental envelopes (Suwannakarn 2009).

5.6.2. Crack propagation in the notched hooked end fiber specimen

In the problem of crack propagation, details of the crack tip damage mechanisms are complex due to the presence of the fiber bundles system. Under tension, crack propagation begins when the tensile stress in the fibers bundles close to the crack tip exceed their strengths. However, subsequent damage of the matrix or interfacial fiber matrix debonding in the fibers near to the crack tip can reduce these fiber stress concentrations, and thereby, the tendency towards crack propagation. Another consequence of the presence of the fiber is that the damage zone, which surrounds the notch, is larger than the theoretical damage zone developed at a crack tip in a typical unreinforced material, and then more possible crack propagation paths in the reinforced material can be expected.
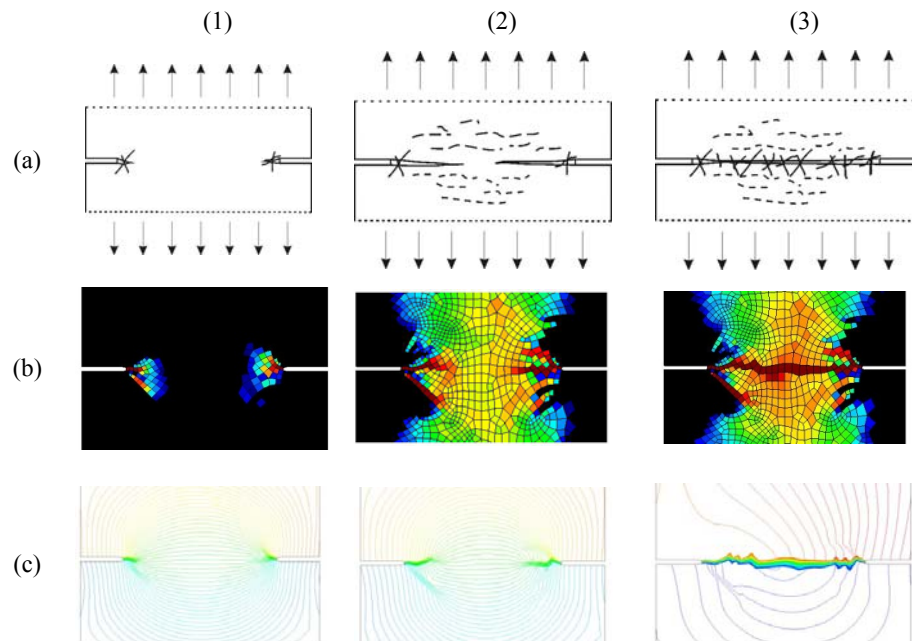
Figure 5.37. Tensile response in (σ-COD) double notched test. (a) Typical crack propagation and
localization in HPFRC composites (Suwannakarn 2009). (b) Numerical damage distribution
($d \geq 0.98$). (c) iso displacement curves displaying the crack evolution.

As the specimen is subjected to the tensile loading process, the concentration of damage
appears mostly at the notches neighborhood, as it is shown in the first stage of Figure
5.37(b). After initiation, the damage progresses in different directions and the area where
microcracking occurrs, grows rapidly between the two notches (stage 2 of Figure 5.37(b)).
During this stage, a larger damage zone is observed when the tensile load increases more, but
the first crack does not propagate and it is probably arrested by the fibers. According to
(Suwannakarn 2009), the first crack does not necessarily propagates through the complete
section, prior to the formation of other cracks. Finally, with further stretching of the speci-
men, it gives rise to damage concentration in zone the between the notches.

Figure 5.37 (c) shows the iso-displacement contour plots in the three stages considered.
As it can be clearly seen in the contour plots, the macrocrack propagates from the notches to
the middle part of the specimen. At the beginning of the fracture process, the stress state is
such that the crack can find more than one possible path to release the stress concentration at
the notch; therefore, branching at the notches is observed during the simulation, so that, more
than one crack competes to form the final macrocrack. This effect was also reflected in the
visual observations of the direct test. As the stretching process steps forward, a single macro-
crack begins to gradually dominate the failure of the composite. The strain hardening beha-
vior in the stress versus crack opening displacement is characterized by the slow propagation

of the main crack from one end of the section to the other end. The macrocrack follows the easiest fracture path and finally, it crosses all the transverse section.

(1)   (2)   (3)

(a) Typical crack propagation

(b) Debonding

$\theta = 0°$

(c) Plasticity

(d) Debonding

$\theta = 90°$
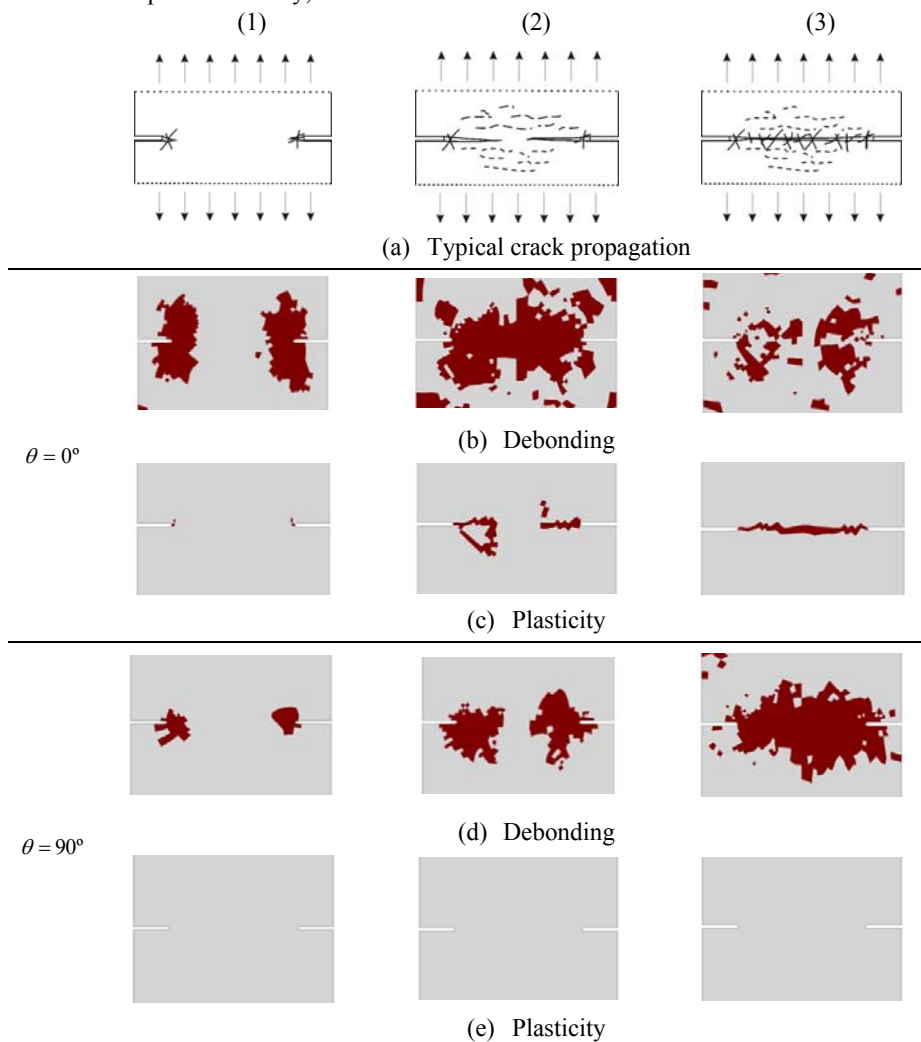
(e) Plasticity

Figure 5.38. Main stages of debonding and plasticity evolution of the loading process. (a) Typical crack propagation and localization in HPFRC composites (Suwannakarn 2009). (b) Debonding distribution $\theta = 0°$. (c) Plasticity distribution $\theta = 0°$.(d) Debonding distribution $\theta = 90°$. (e) Plasticity distribution $\theta = 90°$. The red areas represent the element in inelastic regime.

For further analysis, we turn back to the typical crack propagation scheme, which is repeated for convenience in Figure 5.38-(a). Figure 5.38-(b) and (c) compares, at the notched zone, the debonding and plasticity evolution in the fiber bundle oriented $\theta = 0°$ respect to the

loading direction. Careful inspection of Figure 5.38-(b) and (c) suggests that, as it may be surmised, the pull out process involves first, a debonding action, which provides alternative paths for the crack to follow and second, fiber plastic deformation, which contributes directly to the total deformation of the composite. The debonding action, accordingly, is preceded by the formation of a new surface at the fiber matrix interface; therefore, reduction of composite strength may be significantly related to the loss of interface resistance.

Figure 5.38-(e) reveals that plastic deformation is not observed in horizontally placed fiber bundle. However, debonding plots in Figure 5.38-(d) predict loss of adhesive and frictional capacity in the interfacial transition zone for this fiber bundle.

Iso-displacement contours for total displacements, in Figure 5.39(a), show a single macrocrack between the two symmetrical notches. This crack pattern compares well with the experimental cracks, which appear on the right hand side of the Figure 5.39. Despite the presence of the notches in the specimen was designed to induce stress concentration in the central region and, in turn, an easy predictability of the crack pattern, experimental findings show in one case (according to Suwannakarn 2009) a deviated crack path respect to the desired trajectory, as it is observed in the specimen on the right side of the Figure 5.39(b).

(a)   (b)
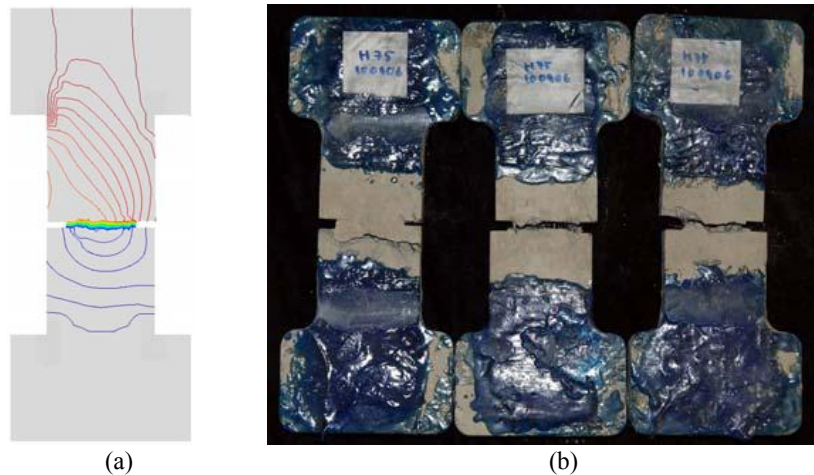
Figure 5.39. Numerical and experimental crack pattern in double notched test. (a) Numerical.
(b) Experimental (Suwannakarn 2009).

Chapter 6
Conclusions and recommendations for further work

6.1. Summary and general conclusions

Based on the multifield theory, a novel formulation to model the HPFRC composite behavior has been presented. The formulation provides a framework, in which the principal ingredient is the relative displacement (slip) between the concrete matrix and the steel fiber. From the point of view of the continuum with microstructure, this slip displacement can be interpreted as a micromorphic variable. Moreover, the formulation incorporates some additional mesostructural mechanisms or interactions such as: 1) the microstress associated with the uniaxial fiber stress σ_f and 2) microforce associated with the shear stress component acting on the interface surface between the fiber and the matrix τ_Γ. The balance equations related with these substructural actions stems from a basic axiom of invariance of the power with respect to classical changes of observers, as it was established by Mariano (Mariano & Stazi 2005). The final expression of the balance equation at the mesoscale is similar to the experimental relation between the axial stress and the shear stress acting in the fiber during the pullout process presented by (Naaman & Najm 1991).

The kinematical description of the fiber is based on the analysis of a single specimen containing a fiber and undergoing a tensile loading process. Taking into account the failure of the matrix fiber interface (IZ) failure allowed us to introduce the morphological descriptor as the relative displacement triggered by the external action. As a consequence of the presence of the new morphology introduced in the kinematical, the composite strain can be written in terms of the displacements $\overline{\mathbf{u}}$, undergone for the matrix, and the relative matrix-fiber displacement (slip) $\boldsymbol{\beta}$. Emphasis is placed here to the consistency and rigor of the approach.

The material multi-field representations must satisfy the laws of thermodynamics, in particular the second law. Therefore, the HPFRC composite constitutive model is based on a thermodynamical framework under the following consideration: the total free energy is partitioned in different terms. Each term is associated with a composite compound, namely, matrix, fiber, and fiber-matrix interface. Therefore, the free energy is expressed in terms of every compound's free energy and its own set of internal variables. The adopted rule of mixture combines the free energy of the compounds proportionally to its volumetric factor. From the obtained overall free energy expression and the constitutive constrains arise composite stresses, as also microstresses and the microsforces concepts. The use of this framework allows developing constitutive models for each of the compounds as well as the overall model for the composite to represent different responses of the material. Finally, appropriated models using damage and plasticity theory are selected to characterize the individual behaviors.

Initially, the proposed model is developed to consider a unique fiber bundle oriented in the $\mathbf{r}$ direction. However, aware of the random nature of the distribution of the fibers in the bulk material, the model is finally generalized to include multiple fiber bundles oriented in several directions, taking care that each of them participates in the overall behavior according to its own volume fraction. In this way, the total free energy is redefined to add as many new terms as the number of bundle fibers considered. The assumption of considering discrete directions regularly distributed with identical volume fraction is, in our opinion, a good representation of the statistical distribution of the fibers in the real case. However, this assumption, although useful in those cases where the fibers are located predominantly in the plane of analysis, does not work satisfactorily in those other cases where the fiber are oriented out of the plane. Therefore, we have restored to the *orientation number* calculated in the manner proposed by Dupont et al (Dupont & Vandewalle 2005), in order to account for the fiber out of the plane of analysis. We consider that this simplification does not alter the results of the fracture analysis because, in the cases subjected to evaluation, the crack pattern does not depend strongly on the thickness dimension.

The model thus obtained from the multifield approach enjoys remarkable features:
- Provides balance momentum equations that represent the pointwise equilibrium of substructural actions. In fact, the fiber pullout and its relation with the slip at the interface surface between the matrix and the fiber is a phenomenon that has been largely studied. However, the models developed for HPFRC composites have not included it explicitly. In our approach, a governing equation of the actions participating on pullout mechanism arises automatically from the multifield framework.
- Unlike the models using internal variables to describe the same phenomenon, by using a continuum microfield to account for the mesoscopic slip displacement, it is possible to write the power of external and internal actions in terms of this new variable. Moreover, the redefinition of the power according to the continuum with microstructure allows us to identify the microstresses and microforces.
- The continuum description of the mesoscopic slip displacement overcomes the problems presented in methods that treat fibers as discrete entities, which re-

quire explicit discretization of every fiber. This kind of approaches can be inefficient and cumbersome, while in our case a less computationally demanding scheme has been proposed.

- The majority of models based on a representative volume element (RVE) make the assumption of perfect local periodicity. Unlike these methodologies, the proposed model, stemming from the continuum with microstructure, does not require it.

The use of the rule of mixtures to calculate the total free energy has the advantage of leading to a simple expression for the composite stresses. Moreover, it is this simplicity that allows the model to include as many fiber bundles as possible to consider the distribution representative of the real statistical one. Additionally, from the implementation point of view, the computation of the total composite quantities, i.e. the total stress tensor and the total constitutive tensor, becomes structured in a modular way.

On the other hand, the use of softening continuum constitutive laws leads to loss of uniqueness of the solution and, thereby, many problems arise in numerical simulations. To overcome the pathologies related to the softening, such as mesh dependency, we have resorted to regularization techniques to prevent localization of deformation into a zero volume zone. The continuum softening modulus was rewritten as a function of the discrete softening parameter, which can be related to material properties as the fracture energy, Young's modulus and the uniaxial peak stress.

A very important mechanisms influencing dramatically the structural behavior of HPFRC composites is the cement fracture. For this reason, the model includes additional tools to characterize the onset and propagation of cracks. These tools are based on the bifurcation analysis and the injection of specific modes of deformation using mixed formulations to increase the ability of the finite element formulation capture solutions with strain localization modes. The failure modes of the composite material are not as simple as in plain concrete. During the onset of the crack evolution, several complicated micromechanisms, that involves all the compounds, interact. Again, the rule of mixtures is useful in the failure analysis because it provides the constitutive tensor of the composite allowing for the bifurcation analysis evaluation so as to find the injection domain. The injection, in the finite element mesh, of specific localization modes is applied to the elements that belong to injection domain. Following this methodology, mesh bias dependence is alleviated.

The couple system of equation, which describes the HPFRC composite and its mesoscale is characterized as a two-field approach. For the computational treatment, a mixed finite element formulation is selected to discretize the domain. It is used triangular and quadrangular elements with linear interpolation functions to represent the displacements $\mathbf{u}$ and the relative matrix-fiber displacement (slip) $\boldsymbol{\beta}$. As for the numerical resolution, two strategies for solving the boundary value problem (BVP) are proposed: a monolithic scheme and a staggered one. In the first strategy, the whole problem is treated as a monolithic entity and all fields are evaluated simultaneously in time. In the staggered strategy, the fields are computationally treated in a sequential form, as isolated entities.

The continuum with microstructure based model for HPFRC composites is finally applied to simulate the mechanical non linear behavior of a set of selected experimental tests.

The mechanical properties of the fiber-matrix interface, the fiber alignment and the fiber volume fraction are changed to show the capability of the model to perform simulations of HPFRC composites under different conditions. Numerical results are compared and discussed in every example to remark some characteristics of the model. Special attention is paid to the discussion of the microstructural results and their relation with the macrostructural behavior, because they have a strongly influence on the failure process.

6.2.   Concluding remarks on the numerical solution scheme

The remarkable aspects of the numerical implementation that deserve consideration include: 1) the regularization of the softening parameter, 2) the strain injection procedure to alleviate the mesh bias dependence of the finite element technique, and 3) the monolithic and staggered procedures to integrate the meso- and macrostructural coupled problem.

In the analysis of the HPFRC composite material, particular attention is given to the mesh size dependence. This is motivated by the presence of the continuum damage model used to characterize the brittle behavior of the concrete, which incorporates strain softening behavior to represent the degradation of the material. But, consequently, as it is well known, the numerical solution in the finite element analysis becomes dependent of the mesh refinement, resulting in physically unreasonable solutions. Therefore, in order to regularize the softening parameter the continuum damage model is based on the smeared crack approach using the consistent characteristic length proposed by (Oliver 1989).

Furthermore, to circumvent the drawback presented in the classical localization methods is the mesh bias dependence, we have introduce a technique develop by Dias et al (Dias et al. 2011b), in which constant strain localization modes are injected via mixed finite elements formulations. The technique proved to alleviate the problem and additionally, according with these authors, from the point of view of the implementation, the sophistication is reduced in comparison with other methods. The technique also shows also benefits when used in the solution of the HPFRC composite model.

The accuracy and stability of the monolithic scheme is given by the characteristic of the selected integration scheme. These two properties of the integration algorithm are essentially related to the way that the numerical integration error, generated at a given step of the analysis, propagates and amplifies in subsequent time steps. The accuracy of the IMPLEX algorithm has been studied and assessed by Oliver et al (Oliver et al. 2008). They also proved that the algorithm is robust enough even in problems where the materials are equipped with strain softening.

The decomposition of the BVP describing the HPFRC composite in many partitions is based on physical and computational considerations. Firstly, the microscopic balance equation and secondly the existence of $n_f + 1$ fields and the corresponding microscopic balance equations combined by means of the rule of mixture allows us to decouple the system of equations. Thus, for the computational treatment, every field can be descritized in space using different interpolation function and even non-matched meshes. However, for simplici-

ty, we have introduced the same discretization for every field. The aspects that should be taken with care in the implementation of the staggered (or partitioned) procedure are: the accuracy, the stability, the computational cost and the efficiency.

The accuracy of the integration scheme is degraded during the application of the staggered strategy, as it was shown in chapter 4. Therefore, the procedure proposed to increase of the solution accuracy is based on the prediction of $\boldsymbol{\beta}$ during the calculation of the field $\mathbf{u}$.

The partitioned approach facilitates the computational implementation issues. The BVP formed by $n_f + 1$ equation showed that following a four-step scheme (prediction of the field $\boldsymbol{\beta}$, advancing of the field $\mathbf{u}$, substitution, and advancing of $\boldsymbol{\beta}$), the solution maintains the accuracy in the same order as the one obtained by using the monolithic scheme.

6.3.   Concluding remarks about the numerical results

The model validation is performed by selecting a set of examples, which explore the capability of the model to represent the mechanical behavior of the HPFRC composite. They evaluate, not only the macromechanical behavior, but also some prominent substructural aspects. The attention, during the evaluation of the model is also focused on the ability of the finite element formulation to capture the fracture process and the manner in which it occurs.

6.3.1.   The notched strip uniaxial loading

In the following, we summarize briefly the obtained results for the notched strip under uniaxial loading:

- The numerical evaluation of a small notched strip was carried out to examine several features of the model, initially with aligned fibers respect to the loading direction and then with inclined fibers. First, in order to investigate the sensitivity of the proposed model to the bond shear strength properties, numerical simulations with identical mechanical and geometrical characteristics are carried out, but varying the bonding properties of the fiber-matrix interface. The analysis of the results gives rise to the classification of the mechanical response in three different behaviors, depending on the debonding failure mechanisms, as follows: (a) fully debonded, (b) partially debonded and (c) fully bonded.
- A weak fiber-matrix interface in the composite (or low values of the ultimate bond strength) produces a poor stress transfer between both components and, therefore, fibers are not fully utilized. The model shows a sudden debonding in the whole domain of the notched strip with consequent deactivation of the composite effect. Low ductility can be associated with low values of the ultimate bond strength.
- The results suggest that for high values of ultimate bond strength τ_u^f, the model predicts a fully bonded case being characterized, in the load displacement curve, by the existence of pseudo strain hardening after the end of the elastic stage.

- Intermediate values of ultimate bond strengths display, in the load-displacement curve, semi-ductile behavior being associated with partially debonded interfaces.
- The effect of the fiber orientation on the response of the notched specimen was investigated for identical ultimate bond strength values. The observed results show that the peak load decreases with the inclination of the fiber. The largest peak load is obtained when inclination equals 0º, i.e. when the fibers are aligned to the load.
- In order to analyze the role played by the element formulation during the localization process, three finite element formulations have been contemplated: i) the standard triangle, ii) the standard quadrilateral element and iii) the injection of an elemental constant strain mode in the quadrilateral element. From the so obtained load displacement curves, it is noted that the post peak response of the notched strip is affected by the finite element approach. The triangular element exhibits stress-locking (spurious stress transfer across a widely open crack), which is caused by a poor kinematical representation of the discontinuous displacement field around the macroscopic crack in the central part of the specimen. Alternatively, the quadrilateral element does not display a quite marked deficient response. Even more, the quadrilateral element with the injection of a constant mode exhibits a clear improvement respect to the triangular formulation.

6.3.2. Beam test with horizontally oriented fibers

Three types of four-point bending test specimens have been examined: i) plain cement, ii) CSS-steel-wire-reinforced cement, and iii) BSS-steel-wire-reinforced cement. In the absence of experimental estimations of the ultimate bond stress value τ_u^f, for the fiber-matrix interface, the purpose of the simulation has been to find a value that satisfactorily predict the structural mechanical response. This parameter has been tuned this parameter to achieve the best structural response fit. The model provides different solutions at different values of the fiber-matrix interface parameter, which are listed below,

- By comparing the experimental results with simulated ones, the BSS-wire reinforced specimen and the numerical response for $\tau_u^f = 7.5 MPa$ are in good agreement, as also, CSS-wire reinforced test result and the curve for $\tau_u^f = 2.5 MPa$.
- From the load displacement curves resulting in this example, it was evident that the fiber-local properties (e.g. interfacial bond strength) affect the postcracking response, so that, the higher is the interfacial bond strength value, the higher is the toughness. This result is due to the redistribution of stresses and proof of this assertion is the extended damage region determined for high values of the ultimate bond strength, in contrast to solutions displaying strain localization and concentration of damage for small values of τ_u^f.
- According to the micromechanics processes observed in the beam test when the matrix-fiber interface parameter has been varied, the structural response is classified into two different types: (a) Deflection softening, and (b) Deflection hardening. In the first case, the postcracking failure mechanisms involve plasticity along the crack path and the debonding domain affects the middle third of the beam distributed not

only to the neighbor points of the macrocrack but also to regions relatively remote from it. Therefore, we can conclude that low ultimate bond strength reduces the bridging effect (or the capacity to transfer stresses between matrix and fiber) and directly decreases the interface toughness (pullout energy). In the second case, i.e., deflection hardening, the results suggest that pullout of fibers trigger plasticity and debonding fracture processes, so the fibers provide much more ductility and toughness to the composite.

- As for the fracture process, an examination of the numerical results provides some insights on how the ultimate bond strength value affects the crack pattern. For low values of the matrix-fiber interface parameter, it is observed a single opening crack pattern at the central part of the beam, almost perpendicular to the longitudinal direction, which reproduces the experimental observation with CSS-wires. However, using high values of the matrix-fiber interface parameter, multiple cracks arise in the beam.

6.3.3.   Dogbone test of HPFRC composite under tensile loading

This example has been used to assess the HPFRC composite material response under tensile behavior undergoing cracking and fracturing. The random distribution of the fibers was assumed uniform and well represented by nine fiber bundles, which are regularly separated. One value for the ultimate bond shear strength was tested based on typical values for the ultimate equivalent bond strength (Guerrero Z 1999).

- During the stretching process, fiber bundles oriented in different direction showed very different debonding and plasticity responses. In the postcracking regime, the horizontal fiber ($\theta = 0º$) remains elastic, while the inclined and aligned fibers ($\theta = 45º$, $\theta = 90º$, respectively), reach the yield condition in the elements on the crack path. On the other hand, debonding distributions showed that all fibers debond around the macrocrack, with a consequent loss of load carrying capacity, and therefore decrease of the composite resistance is observed in the stress-strain curve.
- It is remarkable that the use of the injection procedure allows to evaluate successfully the crack path, when multiple fiber bundles are considered in the analysis. Also, it is important to note that this method reduces mesh-bias dependence.
- Very high values of damage in concrete matrix are presented in early stages of the loading process, which can be interpreted as microcracking. Besides, large areas of the dogbone are severely degraded at the end of loading as effect of the pullout process.

6.3.4.   Crack opening displacement test using a notched dogbone

A fiber reinforced dogbone-shaped notched specimen has been examined to control the location of the crack position. To ensure adequate propagation path, the specimen has symmetrical notches at their middle section. About this example, we can make the following remarks:

- The numerical result lies within the experimental envelopes. However, some discrepancies between the numerical results and the experimental ones were observed for the post cracking branch of the load displacement curve. It is possible that the large variability reported in experiments and the small number of specimens used for this case (only 3) has something to do with this difference. Moreover, from experimental results, the coefficient of variation (normalized measure of dispersion) for the toughness in specimens using hooked end fibers presented values over 60%.
- The analysis of the crack propagation in the notched specimen observed in the simulations approaches very well the experimental observations described by (Suwannakarn 2009). Typically, three stages characterize the failure process: (1) the onset of the first crack, (2) multiple cracks, associated with strain hardening, and (3) the localization, associated with strain softening, which were detected by the model.
- The application of the model on the specimen reveals that the presence of the fibers induces more than one possible path to release the stress concentration at the notch; and therefore, branching at the notches location is observed, so that, more than one crack competes to form the final macrocrack. Finally, one macrocrack follows the easiest fracture path during its propagation and crosses all the transverse section while the others close.

6.3.5. Beam with randomly distributed fibers

The model is applied to a notched beam designed according to the RILEM specification (162-TDF 2002). It contains randomly distributed fibers and a notch is situated in the middle span, which is sufficiently small to avoid undesirable effects. Results for unreinforced and reinforced beam were compared. The numerical results of this example give rise to the following conclusions:

- Experimental and numerical curves agree quite well up to the peak load, but after this point, the proposed model slightly overestimates the load. The crack pattern of the unreinforced and the reinforced specimens display a single crack when using the approach presented in this work, which agree with the real case. However, the reinforced specimen does not split abruptly in two parts and presents larger deformation in comparison with the unreinforced beam.
- The results proved that the coupled effect of the fiber-matrix interface debonding and the axial plastic strain in the fiber affect the composite behavior in such a manner that the brittleness of the unreinforced material is removed.
- According to the iso color map in the end of the loading process, severe degraded material is presented in the notch proximity and in the symmetrical region around it. However, no multiple cracks are shown in this case. It is remarkable that in this particular case a good part of the material remains elastic and it behaves as a composite during the complete loading process.

6.4.   Main contributions of this research

The present work has been devoted to investigate a new model, which describes the non-linear mechanical response of the HPFRC composite as a structured micromorphic material. The main idea in the presented model is to introduce an internal morphological descriptor to include the fiber-matrix relative displacement in the structural behavior of the material, all of this based on the multifield theory. The essential contributions of the new model are the following.

- The introduction of a new kinematical independent variable, the morphological descriptor, that accounts for the mentioned fiber-matrix sliding mechanism. Additionally, the kinematic that describes the deformation mechanism of the fiber and the matrix at the meso-level.
- The balance equation of the substructural actions derived for this model, connecting the micro stresses with the micro forces and which has a physical meaning related with the fiber-matrix bond slip mechanism.
- The application of the mixture theory in order to derive the expression of the composite free energy. Initially, it is applied to a unique fiber bundle oriented in the direction $\mathbf{r}$ and then, it is generalized to include multiple fiber bundles oriented in several directions.
- The extension of the localized strain injection procedure via mixed formulations to simulate the fracture problem of the HPFRC composite.
- The numerical implementation of the finite element formulation and the fracture model of the HPFRC composite.
- Two integration schemes for solving the couple system of equations that describes the behavior of ht HPFRC composite. Firstly, a monolithically scheme and secondly, a staggered scheme.
- The model assessment via a selected set of numerical example inspired by experimental cases. The numerical validation illustrates different aspects of the proposed methodology.

6.5.   Future research lines

The main goal of developing a consistent and rigorous approach to the multifield modeling of HPFRC composite has only partly achieved in this work. This is realized through the further development of the mesoscale model to include not only the fiber-interface but also other fields, which participates in the meso-mechanical failure process such as spalling, bending and straightening of the fiber, among others. In parallel, the identification and determination of the parameters that are related to these mechanisms. These developments should be based on framework of the multifield theory to maintain the consistency and rigorousness of the model. On the other hand, some weaknesses of the proposed model were observed and require special attention and further work:

- The HPFRC composite is a three dimensional problem. The simulation of the damage and failure of short fiber reinforced composites highly depend on the spatial distribution and orientation of the fibers. The assumption used in the model that the randomly distribution can be represented by a limited number fiber bundles is a conservative one.
- The partitioned procedure for the analysis of the HPFRC composite coupled problem was implemented in the present study using a sequential strategy. However, this methodology could be more efficient when considering a high number of fiber bundles if it is parallelized.
- The matrix-fiber interface characterization, i.e. the ultimate bond shear strength values and its fracture energy properties, is a critical point. The model requires this information to analyze adequately the material behavior. However, a unified method to extract the material parameters from experimental test is not yet available.
- The material modeling of each compound of the composite in this study use simple constitutive models to represent their nonlinear behavior. However, the rule of mixture that was considered to combine the individual mechanical behaviors might overestimate the composite response. Enhancements in the constitutive model are convenient to include other loading modes, which were not studied here in detail, such as compression or shear.

The summarized points above gives rise to two areas that deserve additional attention in the modeling of short fiber composites. They are presented in the following subsections

6.5.1.   Multifield modeling

- The multifield based model can be extended to other composites that present the same morphology as the HPFRC composite. Special object of study can be fiber reinforced metal composites or polymer composites, which contain high volume fractions of fibers and a detailed discretization is unsuitable. Usually, the analysis of these materials is done by means of phenomenological approaches that omit in many cases the mesostructural influence in the fracture analysis.
- Some others mesomechanical morphologies can be incorporated to the model to account for the spalling, straightening of the fibers during pullout, fiber-fiber interaction, or other possible mechanisms that affect the global failure process.
- The model should be extended to three dimensional cases in order to avoid the assumption about the orientation of the fibers, which implies a reduction of the volume fraction due to the fibers that are out the plane of analysis in the 2D case presented.
- The model was implemented using triangular and quadrilateral elements, and it was used the same discretization for the field $\mathbf{u}$ and $\boldsymbol{\beta}$. However, different discretizations can be applied. Thereby, future studies about this topic can be fruitful.

6.5.2. Implementation issues

- Although the staggered scheme for solving the non-linear equation system showed stability, it is an important concern to study rigorously this aspect as well as the accuracy of the procedure.
- In the context of the fracture model, many enhancements to capture better the microcracking and the macrocrack patterns. Recent studies provide guides in this regard and they can be applied to the model for the HPFRC composite to alleviate even more mesh bias dependence and other mesh related pathologies.

Appendix I

We show that the angular momentum balance equation arising in the HPFRC model as derived from the multifield theory ((Mariano & Stazi 2005)), results the classical angular momentum balance equation of the conventional continuum mechanics specifying the symmetry of the stress tensor $\boldsymbol{\sigma}$.

First, we derive the transformation law of $\dot{\boldsymbol{\beta}}$ under an observer change. Let us consider the expression (2.10), (2.17) and (2.18):

$$\boldsymbol{\beta} = \beta(r,s,t)\mathbf{r} \quad ; \quad \mathbf{S} = \sigma_{rr}(r,s,t)(\mathbf{r} \otimes \mathbf{r}); \quad \mathbf{z} = z_r \mathbf{r}; \tag{I.1}$$

where z_r is the r-component of $\mathbf{z}$. Also, consider that $\boldsymbol{\beta}$ is the micromorphic field described by the observer 1 and $\hat{\boldsymbol{\beta}}$ is the same entity described by the observer 2. Both observers differing by a time dependent rotation: $\mathbf{Q}(t)$, where $\mathbf{Q} \in SO(3)$ is a time dependent second order rotation tensor, plus a time dependent translation. Then, given the rate of the micromorphic field $\dot{\boldsymbol{\beta}}$ described by the observer 1, the same entity described by the observer 2, and denoted $\dot{\hat{\boldsymbol{\beta}}}$, is:

$$\dot{\hat{\boldsymbol{\beta}}}\Big|_{Q=1} = \overline{(\beta\mathbf{Qr})}\Big|_{Q=1} = \left[\dot{\beta}\mathbf{Qr} + \beta\dot{\mathbf{Q}}\mathbf{r} + \beta\mathbf{Q}\dot{\mathbf{r}}\right]\Big|_{Q=1} = \dot{\boldsymbol{\beta}} + \mathbf{Q}\dot{\mathbf{Q}}\Big|_{Q=1}\boldsymbol{\beta} \tag{I.2}$$

In this expression, the axial vector, spin, of the instantaneous rotation velocity, of one observer respect to other ($\mathbf{Q}\dot{\mathbf{Q}}\Big|_{Q=1}$), is denoted with $\mathbf{q}$ and the following identity follows: $\mathbf{Q}\dot{\mathbf{Q}}\Big|_{Q=1}\boldsymbol{\beta} = \mathbf{q} \wedge \boldsymbol{\beta}$. Introducing the third order permutation tensor $\mathbf{e}$ ($\mathbf{e}_{ijk} = 1$ if (i, j, k) is an even permutation of $(1,2,3)$, $\mathbf{e}_{ijk} = -1$ if it is an odd permutation, and 0 if any index is repeated), such that : $\mathbf{q} \wedge \boldsymbol{\beta} = \mathbf{e} : (\mathbf{q} \otimes \boldsymbol{\beta})$, in (I.2) we can write: $\mathbf{Q}\dot{\mathbf{Q}}\Big|_{Q=1}\boldsymbol{\beta} = (-\mathbf{e}\boldsymbol{\beta})\mathbf{q} = \mathcal{A}\mathbf{q}$, where the operator:

$$\mathcal{A} = \frac{d\dot{\boldsymbol{\beta}}}{d\mathbf{q}} = -\mathbf{e}\boldsymbol{\beta}. \tag{I.3}$$

Due to the co-linearity of $\boldsymbol{\beta}$ and $\mathbf{z}$, it results, for any arbitrary rotation $\mathbf{Q}$, that:

$$\mathcal{A}^T \mathbf{z} = 0; \tag{I.4}$$

and expressing $(\nabla \mathcal{A}^T)\mathbf{S}$ in indicial notation, it also result:

$$(\nabla \mathcal{A}^T)\mathbf{S} = -e_{ijk} \frac{\partial \beta_k}{\partial x_l} S_{jl}; = \mathbf{0} \tag{I.5}$$

because the indices (j,l and k) are identical. With (I.4) and (I.5), we conclude that the angular momentum balance equation (equation (17) in Mariano et al. (Mariano & Stazi 2005)):

$$skew(\boldsymbol{\sigma}) = \mathcal{A}^T \mathbf{z} + (\nabla \mathcal{A}^T)\mathbf{S} = \mathbf{0}; \tag{I.6}$$

turns out to be the classical angular momentum balance equation of the conventional continuum mechanics, form where the symmetry of the conventional stress tensor must be enforced.

References

162-TDF, R. T. (2002) Recommendations of RILEM TC 162-TDF: Test and design methods for steel fibre reinforced concrete: bending test. *Materials and Structures,* 35**,** 579 - 582.

Aboudi, J. (1989) Micromechanical Analysis of Composites by the Method of Cells. *Applied Mechanics Reviews,* 42**,** 193-221.

Armero, F. & Garikipati, K. (1996) An analysis of strong discontinuities in multiplicative finite strain plasticity and their relation with the numerical simulation of strain localization in solids. *International Journal of Solids and Structures,* 33**,** 2863-2885.

Aveston, J. & Kelly, A. (1973) Theory of Multiple Fracture of Fibrous Composites. *Journal of Materials Science,* 8**,** 352-362.

Banthia, N., Bentur, A. & Mufti, A. A. (1998) *Fiber reinforced concrete: present and future,* Canadian Society for Civil Engineering.

Banthia, N. & Trottier, J.-F. (1994) Concrete Reinforced with Deformed Steel Fibers, Part I: Bond-Slip Mechanisms. *ACI Materials Journal,* 91**,** 435-446.

Barros, J., Cunha, V., Ribeiro, A. & Antunes, J. (2005) Post-cracking behaviour of steel fibre reinforced concrete. *Materials and Structures,* 38**,** 47-56.

Bažant, Z. & Oh, B. (1983) Crack band theory for fracture of concrete. *Materials and Structures,* 16**,** 155-177.

Bažant, Z. & Planas, J. (1998) *Fracture and size effects in concrete and other quasibrittle materials* Boca Raton, CRC Press.

Beghini, A., Bazant, Z., Zhou, Y., Gouirand, O. & Caner, F. (2007) Microplane Model M5f for Multiaxial Behavior and Fracture of Fiber-Reinforced Concrete. *Journal of Engineering Mechanics,* 133**,** 66-75.

Bencardino, F., Rizzuti, L., Spadea, G. & Swamy, R. N. (2010) Experimental evaluation of fiber reinforced concrete fracture properties. *Composites Part B: Engineering,* 41**,** 17-24.

Bensoussan, A., Lions, J.-L. & Papanicolaou, G. (1978) *Asymptotic analysis for periodic structures*, Elsevier.

Benssousan, A., Lions. J.L & G., P. (1978) *Asymptotic Analysis for Periodic Structure,* Amsterdam North-Holland.

Benvenuti, E. (2008) A regularized XFEM framework for embedded cohesive interfaces. *Computer Methods in Applied Mechanics and Engineering,* 197**,** 4367-4378.

Beyerlein, I. J. & Phoenix, S. L. (1996) Stress concentrations around multiple fiber breaks in an elastic matrix with local yielding or debonding using quadratic influence superposition. *Journal of the Mechanics and Physics of Solids,* 44**,** 1997 - 2039.

Bilby, B. A., Cottrell, A. H. & Swinden, K. H. (1963) The Spread of Plastic Yield from a Notch. *Proceedings of the Royal Society of London. Series A, Mathematical and Physical Sciences,* 272**,** 304-314.

Bolander, J., Choi, S. & Duddukuri, S. (2008) Fracture of fiber-reinforced cement composites: effects of fiber dispersion. *International Journal of Fracture,* 154**,** 73-86.

Bolander, J. E. & Sukumar, N. (2005) Irregular lattice model for quasistatic crack propagation. *Physical Review B,* 71**,** 094106.

Bongué Boma, M. & Brocato, M. (2010) A continuum model of micro-cracks in concrete. *Continuum Mechanics and Thermodynamics,* 22**,** 137-161.

Borst, R. d., Remmers, J. J. C., Needleman, A. & Abellan, M.-A. (2004) Discrete vs smeared crack models for concrete fracture: bridging the gap. *International Journal for Numerical and Analytical Methods in Geomechanics,* 28**,** 583-607.

Boulfiza, M. (1998) Constitutive Modeling of Fiber Reinforced Cement Composites. *Departament of Civil Engineering.* Vancouver, The University of British Columbie.

Broch, E. & Franklin, J. A. (1972) The point-load strength test. *International Journal of Rock Mechanics and Mining Sciences & Geomechanics Abstracts,* 9**,** 669-676.

Capriz, G. (1989) *Continua with microstructure,* Berlin, Springer Verlag.

Capriz, G. & Mariano, P. M. (2001) Multifield theories: an introduction. *International Journal of Solids and Structures,* 38**,** 939 - 941.

Car, E., Zalamea, F., Oller, S., Miquel, J. & Oñate, E. (2002) Numerical simulation of fiber reinforced composite materials--two procedures. *International Journal of Solids and Structures,* 39**,** 1967 - 1986.

Carpinteri, A., Cornetti, P., Barpi, F. & Valente, S. (2003) Cohesive crack model description of ductile to brittle size-scale transition: dimensional analysis vs. renormalization group theory. *Engineering Fracture Mechanics,* 70**,** 1809-1839.

Colin, J. (2000) *Fiber-reinforced cements and concrete*, Gorgon and Breach Science publishers.

Coto Roquet, L. A. (2007) Ecuaciones constitutivas para el análisis de secciones de HRFA. Ingeniería de la Construcción, Universitat Politècnica de Catalunya.

Cox, H. L. (1952) The Elasticity and Strength of Paper and Other Fibrous Materials. *British Journal of Applied Physics* 3**,** 72-79.

Cunha, V. M. C. F., Barros, J. A. O. & Sena-Cruz, J. M. (2007) Pullout behaviour of hooked-end steel fibres in

self-compacting concrete. Guimarães.

De Souza Neto, E., Perić, D. & Owen, D. (2008) *Computational methods for plasticity. Theory and applications,* Chichester, John Willey & Sons Ltd.

de Souza Neto, E. A. & Feijóo, R. A. (2010) Variational Foundations of Large Strain Multiscale Solid Constitutive Models: Kinematical Formulation. *Advanced Computational Materials Modeling.* Wiley-VCH Verlag GmbH & Co. KGaA.

Dias, I. (2012) Strain injection techniques in numerical modeling of propagating material failure. *Departamento de resistencia de materiales y estructuras en la ingeniería.* Barcelona, Universidad Politécnica de Cataluña.

Dias, I. F., Oliver, J. & Huespe, A. E. (2011a) Strain injection, mixed formulation and strong discontinuities in fracture modeling of quasi-brittle materials. *Congress in numerical methods in engineering.* Coimbra.

Dias, I. F., Oliver, J. & Huespe, A. E. (2011b) Strain injection, mixed formulations and strong discontinuities in fracture modeling of quasi-brittle materiales. IN ANTÓNIO., T., ISABEL, N. F., FELIPE, M. L., ANTONIO, R.-F., IRENE, A. & JESUS, B. (Eds.) *Congress on numerical methods in engineering.* Coimbra

Dupont, D. & Vandewalle, L. (2005) Distribution of steel fibres in rectangular sections. *Cement and Concrete Composites,* 27**,** 391 - 398.

Ericksen, J. L. (1974) Liquid crystals and cosserat surfaces. *Mechanics and applied mathematics,* 27**,** 213-219.

Fantilli, A., Mihashi, H. & Vallini, P. (2007) Crack profile in RC, R/FRCC and R/HPFRCC members in tension.

Fantilli, A. P., Mihashi, H. & Vallini, P. (2009) Multiple cracking and strain hardening in fiber-reinforced concrete under uniaxial tension. *Cement and Concrete Research,* 39**,** 1217 - 1229.

Fantilli, A. P. & Vallini, P. (2007) A Cohesive Interface Model for the Pullout of Inclined Steel Fibers in Cementitious Matrixes. *Journal of Advanced Concrete Technology,* 5**,** 247-258.

Felippa, C., Park, K. C. & Farhat, C. (2001) Partitioned analysis of coupled mechanical systems. *Computer Methods in Applied Mechanics and Engineering,* 190**,** 3247-3270.

Ferrara Liberato, R. G. (2000) Non-local damage analysis of three-point on SFRC notched beams. *Fiber Reinforced concrete (FRC) BEFIB' 2000.*

Ferreira, L. (2007) Fracture analysis of a high-strength concrete and a high-strength steel-fiber-reinforced concrete. *Mechanics of Composite Materials,* 43**,** 479-486.

Fischer, J. Y. a. G. (2006) Investigation of the Fiber Bridging Stress-Crack Opening Relationship of Fiber Reinforced Cementitious Composites. IN LI, G. F. A. V. C. (Ed.) *International RILEM Workshop on High Performance Fiber Reinforced Cementitious Composites in Structural Applications.*

Fish, J., Shek, K., Pandheeradi, M. & Shephard, M. S. (1997) Computational plasticity for composite structures based on mathematical homogenization: Theory and practice. *Computer Methods in Applied Mechanics and Engineering,* 148**,** 53-73.

Ghosh, S., Lee, K. & Moorthy, S. (1995) Multiple scale analysis of heterogeneous elastic structures using homogenization theory and voronoi cell finite element method. *International Journal of Solids and Structures,* 32**,** 27-62.

Ghosh, S., Lee, K. & Raghavan, P. (2001) A multi-level computational model for multi-scale damage analysis in composite and porous materials. *International Journal of Solids and Structures,* 38**,** 2335-2385.

Grammenoudis, P. & Tsakmakis, C. (2009) Micromorphic continuum Part I: Strain and stress tensors and their associated rates. *International Journal of Non-Linear Mechanics,* 44**,** 943 - 956.

Guerrero, P. & Naaman, A. E. (2000) Effect of mortar fineness and adhesive agents on the pull-out response of steel fibers. *ACI Materials Journal,* 97**,** 12-20.

Guerrero Z, A. P. (1999) Bond stress-slip mechanisms in high performance fiber reinforced cement composites.

Hariri, K. (2001) Fracture Mechanics Behaviour of Concrete at Early Age. IN ELFGREN, L. (Ed.) *IMPROVED PRODUCTION OF ADVANCED CONCRETE STRUCTURES.* Technical University of Braunschweig.

Herakovich, C. (1998) *Mechanics of Fibrous Composites,* New York John Wiley and Sons Inc

Hernández, J. (2008) Numerical modeling of crack formation in powder compaction based manufacturing processes. Universitat Politècnica de Catalunya Escola Tècnica Superior D'enginyers de Camins, Canals I Ports.

Hill, R. (1964) Theory of Mechanical Properties of Fibre-strengthened Materials: I. Elastic Behaviour. *Journal of the Mechanics and Physics of Solids,* 12**,** 199-212.

Hillerborg, A., Modéer, M. & Petersson, P. E. (1976) Analysis of crack formation and crack growth in concrete by means of fracture mechanics and finite elements. *Cement and Concrete Research,* 6**,** 773-781.

Hofstetter, G. & Meschke, G. (2011) *Numerical Modeling of Concrete Cracking*, Springer.

Holzapfel, G. (2000) *Nonlinear solids mechanics, A continuum approach for engineering,* Chichester, Wiley.

Hu, X., Day, R. & Dux, P. (2003) Biaxial failure model for fiber reinforced concrete. *Journal of Materials in Civil Engineering,* 15**,** 609-615.

Jiang, H., Valdez, J. A., Zhu, Y. T., Beyerlein, I. J. & Lowe, T. C. (2000) The strength and toughness of cement reinforced with bone-shaped steel wires. *Composites Science and Technology,* 60**,** 1753 - 1761.

Kabele, P. (2007a) Multiscale framework for modeling of fracture in high performance fiber reinforced cementitious composites. *Engineering Fracture Mechanics,* 74**,** 194 - 209.

Kabele, P. (2007b) Multiscale framework for modeling of fracture in high performance fiber reinforced cementitious composites. *Engineering Fracture Mechanics,* 74**,** 194-209.

Kim, D., Naaman, A. E. & El-Tawil, S. (2008) Comparative flexural behavior of four fiber reinforced cementitious composites. *Cement and Concrete Composites,* 30**,** 917 - 928.

Kim, D. J., Naaman, A. E. & S, E.-T. (2009) High Performance Fiber Reinforced Cement Composites with Innovative Slip Hardening Twisted Steel Fibers. *International Journal of Concrete Structures and Materials,* 3**,** 119-126.

Kim, P., Li, V. & Kamada, T. (2002) Fracture Toughness of Microfiber Reinforced Cement Composites. *Journal of Materials in Civil Engineering,* 14**,** 384-391.

Kulla, J. (1998) Constitutive modeling of fiber reinforced brittle materials. Helsinki university of technology.

Lange-Kornbak, D. & Karihaloo, B. L. (1997) Tension softening of fibre-reinforced cementitious composites. *Cement and Concrete Composites,* 19**,** 315-328.

Laranjeira, F., Aguado, A. & Molins, C. (2010) Predicting the pullout response of inclined straight steel fibers. *Materials and Structures,* 43**,** 875-895.

Lee, Y., Kang, S.-T. & Kim, J.-K. (2010) Pullout behavior of inclined steel fiber in an ultra-high strength cementitious matrix. *Construction and Building Materials,* 24**,** 2030 - 2041.

Leung, C. K. Y. & Geng, Y. P. (1998) Micromechanical modeling of softening behavior in steel fiber reinforced cementitious composites. *International Journal of Solids and Structures,* 35**,** 4205 - 4222.

Leung, C. K. Y. & Li, V. C. (1990) Applications of a two-way debonding theory to short fiber composites. *Composites* 21**,** 305-317.

Li, F. & Li, Z. (2000) Continuum damage mechanics based modeling of fiber reinforced concrete in tension. *International Journal of Solids and Structures,* 38**,** 777-793.

Li, F. & Li, Z. (2001) Continuum damage mechanics based modeling of fiber reinforced concrete in tension. *International Journal of Solids and Structures,* 38**,** 777-793.

Li, Q. M. (2001) Strain energy density failure criterion. *International Journal of Solids and Structures,* 38**,** 6997-7013.

Li, V. C. (1992) A simplified micromechanical model of compressive strength of fiber-reinforced cementitious composites. *Cement and Concrete Composites,* 14**,** 131 - 141.

Li, V. C. (2003) On High Performance Fiber Reinforced Cementitious Composite. *JCI Symposium on DFRC***,** 13-23.

Li, V. C. & Stang, H. (1997) Interface property characterization and strengthening mechanisms in fiber reinforced cement based composites. *Advanced Cement Based Materials,* 6**,** 1-20.

Li, V. C. & Wang, S. (2006) Microstructure variability and macroscopic composite properties of high performance fiber reinforced cementitious composites. *Probabilistic Engineering Mechanics,* 21**,** 201 - 206.

Lin, Z. & Li, V. C. (1997) Crack bridging in fiber reinforced cementitious composites with slip-hardening interfaces. *Journal of the Mechanics and Physics of Solids,* 45**,** 763 - 787.

Linero, S. D. L. (2006) Un modelo del fallo material en el hormigón armado, mediante la metodología de discontinuidades fuertes de continuo y la teoría de mezclas. Universitat Politècnica De Catalunya Escola Tècnica Superior D'enginyers De Camins, Canals I Ports.

Mariano, P. (2007) Roubícek, T., Nonlinear partial differential equations with applications. *Meccanica,* 42**,** 615-616.

Mariano, P. (2008a) Cracks in Complex Bodies: Covariance of Tip Balances. *Journal of Nonlinear Science,* 18**,** 99-141.

Mariano, P. & Stazi, F. (2005) Computational aspects of the mechanics of complex materials. *Archives of Computational Methods in Engineering,* 12**,** 391-478.

Mariano, P. M. (2000) Configurational forces in continua with microstructure. *Zeitschrift für Angewandte Mathematik und Physik (ZAMP),* 51**,** 752-791.

Mariano, P. M. (2008b) Mechanics of complex bodies: Commentary on the unified modeling of material substructures. *Theoretical and Applied Mechanics,* 35**,** 235-254.

Martínez, X. (2008) Micromechanical simulation of composite materials using the serial/parallel mixing theory. *Departament de resistència de materials i estructures a l'enginyeria.* Barcelona, Universistat Politècnica de Catalunya.

Maugin, G. (1992) *The thermomechanics of plasticity and fracture*, Cambridge University Press.

Mindlin, R. D. (1964) Micro-structure in linear elasticity. *Archive for Rational Mechanics and Analysis,* 16**,** 51-78.

Möes, N., Dolbow, J. & Belytschko, T. (1999) A Finite Element Method for Crack Growth Remesching. *International Journal for Numerical Methods in Engineering,* 46**,** 131-150.

Mori, T. & Tanaka, K. (1973) Average stress in matrix and average elastic energy of materials with misfitting inclusions. *Acta Metallurgica,* 21**,** 571-574.

Mosconi, M. (2005) Multifield hyperelasticity: variational theorems for complex bodies. *Mechanics Research Communications,* 32**,** 525 - 535.

Muliana, A. H. (2008) Multi-scale framework for the thermo-viscoelastic analyses of polymer composites. *Mechanics Research Communications,* 35**,** 89-95.

Muliana, A. H. & Haj-Ali, R. (2008) A multi-scale framework for layered composites with thermo-rheologically complex behaviors. *International Journal of Solids and Structures,* 45**,** 2937 - 2963.

Naaman, A. & Reinhardt, H. (2006) Proposed classification of HPFRC composites based on their tensile response. *Materials and Structures,* 39**,** 547-555.

Naaman A. E & Alwan J.A (1993) Comment on "Characterization of Interfacial Properties in Fiber-Reinforced Cementitious Composites". *Journal of american ceramic society,* 76**,** 1645-1646.

Naaman A. E, R. H. W. (1995) High performance fiber reinforced cement composites 2 (HPFRCC 2): proceedings of the Second International RILEM Workshop 'High Performance Fiber Reinforced Cement Composites'. IN A E NAAMAN, R. H. W. (Ed.).

Naaman A. E, S. S. P. (1976) Pull-out Mechanisms in Steel Fiber Reinforced Concrete. *Journal of the structural division***,** 1537-1548.

Naaman, A. E. (2003) Engineered Steel Fibers with Optimal Properties for Reinforcement of Cement Composites. *Journal of Advanced Concrete Technology,* 1**,** 241-252.

Naaman, A. E. (2007a) High Performance Fiber Reinforced Cement Composites. IN CAIJUN & MO, Y. L. (Eds.) *High Performance Construction Materials – Science and Applications.* World Scientific Publishing Co. Pte. Ltd.

Naaman, A. E. (2007b) Tensile strain-hardening FRC composites: Historical evolution since the 1960. IN GROSSE, C. U. (Ed.) *Advances in Construction Materials 2007.* Springer Berlin Heidelberg.

Naaman, A. E. & Najm, H. (1991) Bond-slip Mechanisms of Steel Fibers in Concrete. *ACI Materials Journal,* 88**,** 135-145.

Naaman, A. E., Namur, G. J., Alwan, J. & Najm, H. (1991) Fiber Pull-Out and Bond Slip. Part I: Analytical Study. *ASCE Journal of Structural Engineering,* 117**,** 2769-2790.

Nammur, G. G. J., and Naaman, A.E. (1989) A Bond Stress Model for Fiber Reinforced Concrete Based on Bond Stress Slip Relationship. *ACI Materials Journal,* 86**,** 45-57.

Nguyen, B. N. & Khaleel, M. A. (2004) A mechanistic approach to damage in short-fiber composites based on micromechanical and continuum damage mechanics descriptions. *Composites Science and Technology,* 64**,** 607 - 617.

Oliver, J. (1989) A consistent characteristic length for smeared cracking models. *International Journal for Numerical Methods in Engineering,* 28**,** 461-474.

Oliver, J., Cervera, M., Oller, S. & Lubliner, J. (1990) Isotropic damage models and smeared crack analysis of concrete. IN Nenad Bicanic, H. M. (Ed.) *Computer aided analysis and design of concrete structures.* Zell am See, Austria.

Oliver, J., Dias, I. F. & Huespe, A. E. (2010a) Strong discontinuities, mixed finite element formulations and localized strain injection, in fracture modeling of quasi-brittle materials. *Computational Modelling of Concrete Structures: EURO-C 2010.* CRC Press.

Oliver, J. & Huespe, A. E. (2004a) Continuum approach to material failure in strong discontinuity settings. *Computer Methods in Applied Mechanics and Engineering,* 193**,** 3195-3220.

Oliver, J. & Huespe, A. E. (2004b) Theoretical and computational issues in modelling material failure in strong discontinuity scenarios. *Computer Methods in Applied Mechanics and Engineering,* 193**,** 2987 - 3014.

Oliver, J., Huespe, A. E., Blanco, S. & Linero, D. L. (2006a) Stability and robustness issues in numerical modeling of material failure with the strong discontinuity approach. *Computer Methods in Applied Mechanics and Engineering,* 195**,** 7093-7114.

Oliver, J., Huespe, A. E. & Cante, J. C. (2008) An implicit/explicit integration scheme to increase computability of non-linear material and contact/friction problems. *Computer Methods in Applied Mechanics and Engineering,* 197**,** 1865 - 1889.

Oliver, J., Huespe, A. E., Cante, J. C. & Díaz, G. (2010b) On the numerical resolution of the discontinuous material bifurcation problem. *International Journal for Numerical Methods in Engineering,* 83**,** 786-804.

Oliver, J., Huespe, A. E., Pulido, M. D. G. & Chaves, E. (2002) From continuum mechanics to fracture mechanics: the strong discontinuity approach. *Engineering Fracture Mechanics,* 69**,** 113-136.

Oliver, J., Huespe, A. E. & Sánchez, P. J. (2006b) A comparative study on finite elements for capturing strong discontinuities: E-FEM vs X-FEM. *Computer Methods in Applied Mechanics and Engineering,* 195**,** 4732-4752.

Oller, S. (2003) *Simulación Númerica del Comportamiento Mecánico de los Materiales Compuestos,* Barcelona, Centro Internacional de Metodos Numéricos en Ingeniría (CIMNE).

Oller, S., Oñate, E., Miquel, J. & Botello, S. (1996) A plastic damage constitutive model for composite materials. *International Journal of Solids and Structures,* 33**,** 2501-2518.

Ostoja-Starzewski, M. (2002) Microstructural randomness versus representative volome element in thermomechanics. *Journal of applied mechanics,* 69**,** 25-35.

P.J. Sánchez, A. E. H., J. Oliver G. Diaz & Sonzogni, V. E. A macroscopic damage-plastic constitutive model for concrete failure simulation.

Paley, M. & Aboudi, J. (1992) Micromechanical analysis of composites by the generalized cells model. *Mechanics of Materials,* 14**,** 127-139.

Patrick, G. W., Marsden, J. E. & Shadwick, W. F. (Eds.) (1993) *Integration Algorithms And Classical Mechanics,* Providence, R.I., American Mathematical Society.

Peng, X. & Meyer, C. (2000) A continuum damage mechanics model for concrete reinforced with randomly distributed short fibers. *Computers \& Structures,* 78**,** 505 - 515.

Pietruszczak, S. & Mróz, Z. (1981) Finite element analysis of deformation of strain-softening materials. *International Journal for Numerical Methods in Engineering,* 17**,** 327-334.

Planas, J., Elices, M., Guinea, G. V., Gómez, F. J., Cendón, D. A. & Arbilla, I. (2003) Generalizations and specializations of cohesive crack models. *Engineering Fracture Mechanics,* 70**,** 1759-1776.

Pros, A., Diez, P. & Molins, C. (2011) Modeling steel fiber reinforced concrete: numerical immersed boundary approach and a phenomenological mesomodel for concrete-fiber interaction. *International Journal for Numerical Methods in Engineering***,** n/a-n/a.

Radtke, F. K. F., Simone, A. & Sluys, L. J. (2010) A computational model for failure analysis of fibre reinforced concrete with discrete treatment of fibres. *Engineering Fracture Mechanics,* 77**,** 597-620.

Rajput, R. K. (2008) *A Textbook of Manufacturing Technology (Manufacturing Processes),* New Delhi, Laxmi Publications.

Rashid, Y. R. (1968) Ultimate strength analysis of prestressed concrete pressure vessels. *Nuclear Engineering and Design,* 7**,** 334-344.

Rastellini, F., Oller, S., Salomón, O. & Oñate, E. (2008) Composite materials non-linear modelling for long fibre-reinforced laminates: Continuum basis, computational aspects and validations. *Computers \& Structures,* 86**,** 879 - 896.

Rice, J. R. & Rudnicki, J. W. (1980) A note on some features of the theory of localization of deformation. *International Journal of Solids and Structures,* 16**,** 597-605.

Robins, P., Austin, S. & Jones, P. (2002) Pull-out behaviour of hooked steel fibres. *Materials and Structures,* 35**,** 434-442.

Rodriguez, F. P., D. (1984) Hormigón con la Incorporación de Fibras. *Revista de Obras Públicas,* 779-796.

Sanchez-Palencia, E. (1987) General introduction to asymptotic methods. IN Sanchez-Palencia, E. & Zaoui, A. (Eds.) *Homogenization Techniques for Composite Media.* Springer Berlin / Heidelberg.

Sánchez-Palencia, E. (1986) Homogenization in Mechanics A Survey of Solved and Open Problems. *Rend. Sem. Mat. Univers. Politecn. Torino,* 44**,** 1-45.

Sanz-Herrera, J. A., García-Aznar, J. M. & Doblaré, M. (2008) Micro-macro numerical modelling of bone regeneration in tissue engineering. *Computer Methods in Applied Mechanics and Engineering,* 197**,** 3092-3107.

Shannag, M., Hnasen, W. & Tjiptobroto, P. (1999) Interface debonding in fiber reinforced cement-matrix composites. *Journal of composites materials,* 33**,** 158-176.

Si-Larbi, A., Ferrier, E. & Hamelin, P. (2006) Flexural behaviour of MRBC beams (multi-reinforcing bars concrete beams), promoting the use of FRHPC. *Composite Structures,* 74**,** 163-174.

Simo, J. C. & Hughes, T. J. R. (1998) *Computational inelasticity,* New York Springer-Verlag.

Simo, J. C. & Ju, J. W. (1987) Strain- and stress-based continuum damage models--I. Formulation. *International Journal of Solids and Structures,* 23**,** 821-840.

Simo, J. C. & Oliver, J. (1994) A new approach to the analysis and simulation of strong discontinuities. IN BAZANT, Z., BITTNAR, B., JIRÁSEK, M. & MAZARS, J. (Eds.) *Fracture and Damage in Quasibrittle Materials, Experiments, Modeling and Computer Analysis.* E&FN Spon.

Simo, J. C., Oliver, J. & Armero, F. (1993) An analysis of strong discontinuities induced by strain-softening in rate-independent inelastic solids. *Computational Mechanics,* 12**,** 277-296.

Sirijaroonchai, K. (2009) A Macro-scale Plasticity Model for High Performance Fiber Reinforced Cement Composites. Civil \& Environmental Engineering, University of Michigan.

Sirijaroonchai, K., El-Tawil, S. & Parra-Montesinos, G. (2010) Behavior of high performance fiber reinforced cement composites under multi-axial compressive loading. *Cement and Concrete Composites,* 32**,** 62 - 72.

Sujivorakul, C., Waas, A. M. & Naaman, A. E. (1999) Pullout Response of a Smooth Fiber with an End Anchorage *Journal of engineering mechanics,* 126**,** 986-993.

Suquet, P. (1987) Elements of Homogenization for Inelastic solids Mechanics. IN SANCHEZ-PALENCIA, E. & ZAOUI, A. (Eds.) *Homogenization Techniques for Composite Media.* Springer Berlin / Heidelberg.

Suwaka, H. & Fukuyama, H. (2006) Nonlinear finite element analysis on shear failure of structural elements using high performance fiber cement composite. *Journal of Advanced Concrete Technology,* 4**,** 45-57.

Suwannakarn, S. W. (2009) Post-cracking characteristics of high performance fiber reinforced cementitious composites. University of Michigan.

Svendsen, B. (2001) Formulation of balance relations and configurational fields for continua with microstructure and moving point defects via invariance. *International Journal of Solids and Structures,* 38**,** 1183-1200.

Tripp, D. E. H., J. H. Gyekenyesi, J. P. (1989) A Review of Failure Models for Unidirectional Ceramic Matrix Composites Under Monotonic Loads. *34th International Gas Turbine and Aeroengine Congress and Exposition.* Toronto, NASA.

Trovalusci, P. & Masiani, R. (2005) A multifield model for blocky materials based on multiscale description. *International Journal of Solids and Structures,* 42**,** 5778 - 5794.

Trusdell, C. & Toupin, R. (1960a) *The clasical field theories,* Berlin, Springer-Verlag.

Trusdell, C. & Toupin, R. (1960b) *The clasical field theories.,* Berlin, springer-verlag.

Trusdell, C. & Toupin, R. (1960c) *Principiples of classical mechanics and field theory,* Berlin, Springer-Verlag.

Tucker Iii, C. L. & Liang, E. (1999) Stiffness predictions for unidirectional short-fiber composites: Review and evaluation. *Composites Science and Technology,* 59**,** 655-671.

Wang, Y., Backer, S. & Li, V. (1989) A statistical tensile model of fiber reinforced cementitious composites. *Journal of composites* 20**,** 265-274.

Welschinger, F. & Miehe, C. (2008) Variational Formulations and FE Active-Set Strategies for Rate-Independent Nonlocal Material Response. *PAMM,* 8**,** 10475-10476.

Willis, J. R. (1967) A comparison of the fracture criteria of griffith and barenblatt. *Journal of the Mechanics and Physics of Solids,* 15**,** 151-162.

Wittel, F. K., Kun, F. & Herrmann, H. J. Damage Simulation of High Performance Fiber Reinforced Concrete.

Wu, H.-C. & Li, V. C. (1994) Trade-off between strength and ductility of random discontinuous fiber reinforced cementitious composites. *Cement and Concrete Composites,* 16**,** 23-29.

Wu, M. S. (2011) Strategies and challenges for the mechanical modeling of biological and bio-inspired materials. *Materials Science and Engineering: C,* 31**,** 1209-1220.

Xu, B., Ju, J. W. & Shi, H. (2010) Progressive Micromechanical Modeling for Pullout Energy of Hooked-end Steel Fiber in Cement-based Composites. *International Journal of Damage Mechanics*.

Zhang, J. & Li, V. C. (2004) Simulation of crack propagation in fiber-reinforced concrete by fracture mechanics. *Cement and Concrete Research,* 34**,** 333-339.

Zhang, J., Li, V. C., Nowak, A. S. & Wang, S. (2002) Introducing Ductile Strip for Durability Enhancement of Concrete Slabs. *Journal of Materials in Civil Engineering,* 14**,** 253-261.

Zhao, P. & Ji, S. (1997) Refinements of shear-lag model and its applications. *Tectonophysics,* 279**,** 37-53.

Zhou, X. F. & Wagner, H. D. (1999) Stress concentrations caused by fiber failure in two-dimensional composites. *Composites Science and Technology,* 59**,** 1063 - 1071.

Scientific work emerging from this research

Journal articles:

Related to chapter 2 and 5:

J. Oliver, D.F. Mora, A. E. Huespe and R. Weyler. A micromorphic model for steel fiber reinforced concrete. International Journal of Solids and Structures. Volume 49, Issue 21, 15 October 2012, Pages 2990–3007

Related to chapter 3, 4 and 5, (submitted):

A.E. Huespe, J. Oliver, D.F. Mora. Computational modeling of high-performance steel fiber reinforced concrete using a micromorphic approach, Computational Mechanics.

Communications to international conferences:

Full papers:

Oliver, F.; Huespe, A.E.; Mora, D. F. Computational modeling of fiber reinforced concrete as a composite complex material. A: International conference on recent advances in nonlinear models. Structural Concrete Applications. "International conference on recent advances in nonlinear models: Structural Concrete Applications (CoRAN 2011)". 2011, p. 41-60.

Abstracts:

D.F. Mora, A. Huespe, X. Oliver: Macro – micro structures modeling of material failure in high performance fiber reinforced cementitious composites, *CD-ROM Proceedings of the 6th European Congress on Computational Methods in Applied Sciences and Engineering (ECCOMAS 2012)*, September 10-14, 2012, Vienna, Austria, Eds.: Eberhardsteiner, J.; Böhm, H.J.; Rammerstorfer, F.G., Publisher: Vienna University of Technology, Austria, ISBN: 978-3-9502481-9-7

Oliver, F.; Huespe, A.E.; Mora, D. F. Multiscale modeling of fiber reinforced cement composites with microstructure. A: II International Conference on Computational Modeling of Fracture and Failure of Materials and Structures. "Computational modeling of fracture and failure of materials and structures: proceedings of the II International Conference on Computational Modeling of Fracture and Failure of Materials and Structures (CFRAC 2011) held in Barcelona, Spain, 6-8 june 2011". Centre Internacional de Mètodes Numèrics en Enginyeria (CIMNE), 2011, p. 269.

Oliver, F.; Huespe, A.E.; Mora, D. F. Computational modelling of fiber reinforced cement composites as a complex material. A: XI International Conference on Computational Plasticity Fundamentals and Applications. "Computational plasticity XI: fundamentals and applications: proceedings of the XI International Conference on Computational Plasticity held in Barcelona, Spain, 07-09 September 2011". Barcelona: Centre Internacional de Mètodes Numèrics en Enginyeria (CIMNE), 2011, p. 1.